



AN ABSTRACT OF THE DISSERTATION OF

Chris Patton for the degree of Doctor of Philosophy in Mechanical Engineering presented on  
February 7, 2013.

Title: Development of Vehicle Dynamics Tools for Motorsports.

Abstract approved:

---

Robert K. Paasch

In this dissertation, a group of vehicle dynamics simulation tools is developed with two primary goals: to accurately represent vehicle behavior and to provide insight that improves the understanding of vehicle performance. Three tools are developed that focus on tire modeling, vehicle modeling and lap time simulation.

Tire modeling is based on Nondimensional Tire Theory, which is extended to provide a flexible model structure that allows arbitrary inputs to be included. For example, rim width is incorporated as a continuous variable in addition to vertical load, inclination angle and inflation pressure. Model order is determined statistically and only significant effects are included. The fitting process is shown to provide satisfactory fits while fit parameters clearly demonstrate characteristic behavior of the tire.

To represent the behavior of a complete vehicle, a Nondimensional Tire Model is used, along with a three degree of freedom vehicle model, to create Milliken Moment Diagrams (MMD) at different speeds, longitudinal accelerations, and under various yaw rate conditions. In addition to the normal utility of MMDs for understanding vehicle performance, they are used to develop Limit Acceleration Surfaces that represent the longitudinal, lateral and yaw acceleration limits of the vehicle.

Quasi-transient lap time simulation is developed that simulates the performance of a vehicle on a predetermined path based on the Limit Acceleration Surfaces described above. The method

improves on the quasi-static simulation method by representing yaw dynamics and indicating the vehicle's stability and controllability over the lap. These improvements are accomplished while maintaining the simplicity and computational efficiency of the two degree of freedom method.

©Copyright by Chris Patton  
February 7, 2013  
All Rights Reserved

Development of Vehicle Dynamics Tools for Motorsports

by  
Chris Patton

A DISSERTATION

submitted to

Oregon State University

in partial fulfillment of  
the requirements for the  
degree of

Doctor of Philosophy

Presented February 7, 2013  
Commencement June 2013

Doctor of Philosophy dissertation of Chris Patton presented on February 7, 2013.

APPROVED:

---

Major Professor, representing Mechanical Engineering

---

Head of the School of Mechanical, Industrial and Manufacturing Engineering

---

Dean of the Graduate School

I understand that my dissertation will become part of the permanent collection of Oregon State University libraries. My signature below authorizes release of my dissertation to any reader upon request.

---

Chris Patton, Author

## ACKNOWLEDGEMENTS

This dissertation represents the final stage of my formal education and in the nearly quarter century that I have been a student, there have been countless teachers, instructors, and professors that have guided me to this point. This is in addition to my friends and family that have supported, encouraged, and often worked alongside me. To you all, I offer my thanks. The following are several acknowledgements directly related to my dissertation.

I would like to thank my adviser Dr. Robert Paasch for providing personal guidance as well as inspiration and guidance for the Global Formula Racing Team (GFR). This team has provided an amazing environment of collaborative education, which would not have come to be without Dr. Paasch's guidance and support.

Thank you to all the members of GFR that have developed the team to its current state, including members of the Beaver Racing Team at Oregon State University and the BA Racing Team at the Duale Hochschule Baden-Württemberg in Ravensburg Germany, that laid the groundwork that would become GFR. Through the development of our vehicles, countless team members have contributed to my understanding of vehicle dynamics. Without this extraordinary group of people that I have been privileged to work with, creating this dissertation would not have been possible.

I am grateful to the many people and institutions that have made Formula SAE and Formula Student possible, including the volunteers and organizers that work tirelessly to provide students with the venues to practice and demonstrate the fruits of our education. In particular, I would like to thank the design judges who shared their knowledge and experience, and consistently challenged me to expand my own. These events would not be possible without the support of SAE, VDI and IMechE. I would like to acknowledge the Formula SAE Tire Testing Consortium and Calspan for providing access to the tire data used in this dissertation.

Finally, I would like to thank my family. While I attribute much of my educational achievement to the happy, loving and encouraging environment provided by my family, I would like thank them in particular for managing to bring up an engineer that is only mildly socially awkward.

## TABLE OF CONTENTS

	<u>Page</u>
1. Dissertation Introduction.....	2
2. Tire Modeling: A Fitting Process for a Non-Dimensional Tire Model with Arbitrary Inputs....	4
2.1. Introduction .....	5
2.2. Background .....	5
2.2.1. Pacejka – Delft Tire .....	5
2.2.2. Nondimensional Tire Theory.....	6
2.3. Pure Slip Model Structure .....	8
2.3.1. Nondimensional Transform .....	8
2.3.2. Simplified Magic Formula .....	10
2.3.3. Model Parameter Response Surfaces.....	11
2.4. Fitting Pure Slip Model Parameters .....	12
2.4.1. Description of Test Data.....	12
2.4.2. Identifying Normalization and Shift Parameters .....	12
2.4.3. Identifying Magic Formula Parameters.....	15
2.4.4. Fitting Response Surfaces .....	16
2.4.5. Determining Model Order .....	18
2.5. Combined Slip Model.....	20
2.5.1. Interaction Response Surface Definition .....	20
2.5.2. Fitting Interaction Response Surfaces .....	22
2.6. Error Evaluation .....	26
2.6.1. Pure Slip .....	27
2.6.2. Combined Slip .....	29
2.6.3. Rim Width .....	29
2.7. Future Work.....	31

## TABLE OF CONTENTS (Continued)

	<u>Page</u>
2.8. Conclusion.....	31
3. Vehicle Modeling: Creating Milliken Moment Diagrams under general Yaw and Longitudinal Acceleration Conditions.....	32
3.1. Introduction .....	33
3.2. Background .....	34
3.2.1. <b>CN-AY</b> Diagrams .....	34
3.2.2. <b>CN-CY</b> Diagrams.....	38
3.2.3. Applications.....	40
3.3. Creating Acceleration Moment Diagrams .....	41
3.3.1. Reference Frames .....	41
3.3.2. Tire Slip Angles .....	41
3.3.3. Vehicle-Slip and Steer Angles.....	42
3.3.4. Vehicle Model Definition .....	44
3.3.5. Free Rolling <b>CN-CY</b> Diagram (Infinite Radius).....	46
3.3.6. Constant Yaw Rate <b>CN-CY</b> Diagram (Finite Radius).....	48
3.3.7. Free Rolling <b>CN-AY</b> Diagram .....	49
3.3.8. Level Surface Moment Diagrams .....	50
3.4. Interpretation .....	57
3.5. Future work.....	60
3.6. Conclusion.....	60
4. Lap Time Simulation: Quasi-Transient Lap Time Simulation via Acceleration-Moment Limit Surfaces.....	61
4.1. Introduction .....	62
4.2. Background .....	62

## TABLE OF CONTENTS (Continued)

	<u>Page</u>
4.3. Necessary Concepts .....	65
4.3.1. Finite Difference Equations.....	65
4.3.2. Derivative Notation.....	66
4.3.3. Curvilinear Motion .....	66
4.4. General Implementation.....	67
4.4.1. Path Representation .....	68
4.4.2. Vehicle Model .....	70
4.4.3. Boundary Speed Profile .....	73
4.4.4. Critical Points .....	75
4.4.5. Limit Speed Profile .....	78
4.4.6. Yaw Velocity and Slip Angle .....	81
4.4.7. Drive-Brake Continuity.....	84
4.4.8. Steering Angle .....	85
4.4.9. Controllability and Stability.....	86
4.4.10. Power Limitation.....	88
4.5. Results.....	88
4.5.1. Quasi-Static vs. Quasi-Transient .....	89
4.5.2. Design Study.....	90
4.6. Future Work.....	91
4.7. Conclusion.....	91
5. Dissertation Conclusion .....	93
6. Bibliography .....	94

## LIST OF FIGURES

<u>Figure</u>	<u>Page</u>
Figure 1: Quadratic fit of longitudinal coefficient of friction .....	11
Figure 2: Longitudinal sweep group - force plotted vs. time .....	13
Figure 3: Longitudinal sweep group - force plotted vs. slip ratio .....	13
Figure 4: Lateral sweep group - force plotted vs. time.....	13
Figure 5: Lateral sweep group - force plotted vs. slip ratio .....	13
Figure 6: Normalized longitudinal force fit with the Magic Formula.....	16
Figure 7: Normalized longitudinal force fit with the Magic Formula – zero crossing.....	16
Figure 8: Normalized lateral force fit with the Magic Formula .....	16
Figure 9: Normalized lateral force fit with the Magic Formula – zero crossing.....	16
Figure 10: Zero order fit of normalized longitudinal stiffness .....	17
Figure 11: Zero order fit of normalized cornering stiffness.....	17
Figure 12: Linear fit of normalized longitudinal.....	17
Figure 13: Linear fit of normalized cornering stiffness .....	17
Figure 14: Quadratic fit of normalized longitudinal stiffness .....	18
Figure 15: Quadratic fit of normalized cornering stiffness .....	18
Figure 16: High order response surface fit to low order data .....	19
Figure 17: High order response curve fit to low order data .....	19
Figure 18: Flow chart for pure slip response fit order selection.....	20
Figure 19: Longitudinal combined slip weight .....	21
Figure 20: Lateral combined slip weight .....	21
Figure 21: Flow chart for interaction response fit order selection.....	24
Figure 22: Longitudinal combined slip weighting surface with superimposed data .....	25
Figure 23: Lateral combined slip weighting surface with superimposed data .....	25
Figure 24: Lateral and longitudinal force for slip ratio sweeps at 3° slip angle.....	25
Figure 25: Lateral and longitudinal force for slip ratio sweeps at 6° slip angle.....	25
Figure 26: Lateral force vs. Slip angle colored by error region .....	27
Figure 27: Longitudinal force vs. slip ratio colored by error region.....	27
Figure 28: Pure longitudinal slip MAE error colored by error region .....	28

## LIST OF FIGURES (Continued)

<u>Figure</u>	<u>Page</u>
Figure 29: Pure lateral slip MAE error colored by error region .....	28
Figure 30: Combined MAE error colored by error region.....	29
Figure 31: Pure longitudinal slip MAE error colored by error region .....	30
Figure 32: Pure lateral slip MAE error colored by error region .....	30
Figure 33: Combined MAE error colored by error region.....	30
Figure 34: Milliken Moment Diagram – <i>CN-AY</i> – 30 m/s .....	33
Figure 35: <i>CN-AY</i> – 30 m/s – cornering sequence .....	35
Figure 36: Lateral and yaw acceleration - on track testing.....	36
Figure 37: Asymmetric oval test track .....	37
Figure 38: <i>CN-CY</i> – infinite radius.....	39
Figure 39: Steer vs. vehicle-slip: normal and construction grids .....	43
Figure 40: Front vs. rear slip angle: normal and construction grids .....	43
Figure 41: Steer vs. vehicle-slip: un-shifted and shifted grids .....	44
Figure 42: Front vs. rear slip angle: un-shifted and shifted grids .....	44
Figure 43: Flow chart for load transfer convergence.....	48
Figure 44: <i>CN-CY</i> – infinite radius – detailed.....	49
Figure 45: <i>CN-CY</i> – 10 meter radius – detailed .....	49
Figure 46: <i>CN-AY</i> – 30 m/s – detailed.....	50
Figure 47: <i>CN-AY</i> – 20 m/s – detailed.....	50
Figure 48: <i>CN-AY</i> – 30 m/s – side view .....	51
Figure 49: <i>CN-AY</i> – 30 m/s – 3d view .....	51
Figure 50: <i>CN-AY</i> – 30 m/s – multiple level surfaces.....	52
Figure 51: Quadratic Taylor approximation of tire force .....	55
Figure 52: Flow chart for level surface convergence .....	56
Figure 53: <i>CN-AY</i> – 30 m/s – driving limit.....	57
Figure 54: <i>CN-AY</i> – 30 m/s – driving limit – g-g view .....	57
Figure 55: <i>CN-AY</i> – 30 m/s – braking limit.....	57
Figure 56: <i>CN-AY</i> – 30 m/s – braking limit – g-g view .....	57

## LIST OF FIGURES (Continued)

<u>Figure</u>	<u>Page</u>
Figure 57: Stability index – 20 m/s – driving.....	58
Figure 58: Stability index – 20 m/s – braking.....	58
Figure 59: Steering sensitivity – 20 m/s – driving .....	59
Figure 60: Steering sensitivity – 20 m/s – braking .....	59
Figure 61: g-g diagram – 20 m/s .....	59
Figure 62: Asymmetric oval test track .....	69
Figure 63: Track map from GPS .....	70
Figure 64: Curvature profile from GPS.....	70
Figure 65: Octahedral LAS (3d) .....	71
Figure 66: General LAS ( $an - \omega$ ) .....	71
Figure 67: Octahedral LAS ( $an - at$ ) .....	71
Figure 68: Octahedral LAS ( $\omega - at$ ).....	71
Figure 69: General LAS (3d) .....	73
Figure 70: General LAS ( $an - \omega$ ) .....	73
Figure 71: General LAS ( $an - at$ ) .....	73
Figure 72: General LAS ( $\omega - at$ ).....	73
Figure 73: Boundary speed profile.....	75
Figure 74: Critical points – Octahedral LAS.....	76
Figure 75: Critical points – General LAS.....	76
Figure 76: Octahedral LAS (3d) w/profile .....	80
Figure 77: Octahedral LAS ( $an - \omega$ ) w/profile .....	80
Figure 78: Octahedral LAS ( $an - at$ ) w/profile .....	81
Figure 79: Octahedral LAS ( $\omega - at$ ) w/profile .....	81
Figure 80: LSP and BSP – Octahedral LAS .....	81
Figure 81: Velocity profile – Iteration comparison .....	82
Figure 82: Acceleration profiles – Iteration comparison .....	82
Figure 83: Yaw rate profile – Iteration comparison .....	83
Figure 84: Vehicle slip profile – Iteration comparison .....	83

## LIST OF FIGURES (Continued)

<u>Figure</u>	<u>Page</u>
Figure 85: Velocity profile – Iteration comparison segment .....	83
Figure 86: Acceleration profiles – Iteration comparison segment .....	83
Figure 87: Yaw rate profile – Iteration comparison segment.....	84
Figure 88: Vehicle slip profile – Iteration comparison segment .....	84
Figure 89: Lap time convergence.....	84
Figure 90: Vehicle slip discontinuities.....	85
Figure 91: Vehicle slip filtering.....	85
Figure 92: Steered angle profile.....	86
Figure 93: Derivative of lateral acceleration w.r.t. steered angle .....	87
Figure 94: Derivative of lateral acceleration w.r.t. Vehicle slip angle .....	87
Figure 95: Derivative of yaw acceleration w.r.t. steered angle .....	87
Figure 96: Derivative of yaw acceleration w.r.t. vehicle slip angle.....	87
Figure 97: Power limitation .....	88
Figure 98: QSS-QTS vehicle slip comparison.....	89
Figure 99: QSS-QTS steered angle comparison.....	89
Figure 100: QSS-QTS yaw control comparison .....	90
Figure 101: QSS-QTS yaw stability comparison .....	90

## **Development of Vehicle Dynamics Tools for Motorsports**

## 1. Dissertation Introduction

A group of vehicle dynamics simulation tools is developed with two goals in mind. The first goal is that the tools should be sufficiently accurate, and describe the performance of a vehicle well enough that they can be used to make decisions when designing or developing a vehicle. The second goal is to provide tools that allow users to improve their understanding of how fundamental vehicle parameters affect vehicle performance. Many common tools used in motorsports lend themselves to either one of these goals but fall short of reaching both. For example, simple linear models can be very enlightening, but their often-simplistic assumptions limit their usefulness. Transient multibody simulations, on the other hand, can be made to replicate reality to a high degree, but the insight provided that comes along with simplicity is lost. The methods presented here represent a step between these two extremes.

The modeling process has been broken up into three sections, Tire Modeling, Vehicle Modeling, and Lap Time Simulation, each of which represent one of the primary chapters of this dissertation. Each section relies on the results of the previous, but useful information and insight into vehicle behavior can be gained at each level.

Tire modeling is based on Nondimensional Tire Theory, which is extended to create a flexible model structure that allows arbitrary inputs to be included. As an example, rim width is incorporated as a continuous variable in addition to vertical load, inclination angle and inflation pressure. Model order is determined statistically and only significant parameters are included. The fitting process is shown to provide satisfactory fits while fit parameters clearly demonstrate characteristic behavior of the tire.

The Nondimensional Tire Model is used along with a simple three degree of freedom vehicle model to create Milliken Moment Diagrams (MMD). A method is demonstrated for creating MMDs at different speeds, longitudinal accelerations, and under various yaw conditions. In addition to the well-established utility of MMDs, they are used to create a Limit Acceleration Surface, analogous to a g-g diagram, that represents the longitudinal, lateral and yaw acceleration limits of the vehicle.

Finally, quasi-transient Lap Time Simulation is developed that simulates the performance of a vehicle on a predetermined path based on the Limit Acceleration Surfaces described above. The method is an improvement on the quasi-static Simulation method as it dynamically simulates the yaw degree of freedom and provides the ability to evaluate vehicle stability and controllability over the lap, while maintaining the simplicity and computational efficiency of the two degree of freedom method.

## **2. Tire Modeling: A Fitting Process for a Non-Dimensional Tire Model with Arbitrary Inputs**

**Abstract:** A general tire model structure is created for predicting lateral and longitudinal tire forces that is based on Nondimensional Tire Theory with several extensions, including an alternative method for combined lateral and longitudinal force interactions. The model structure allows for additional arbitrary inputs beyond the required inputs of slip angle, slip ratio and vertical force. The fitting process determines the internal model structure through statistical error analysis. This process is demonstrated by fitting a model with additional inputs of inclination, inflation pressure and wheel rim width.

## 2.1. Introduction

Typical tire models have a pre-determined structure for predicting forces and moments based on a set group of inputs (e.g., slip angle, slip ratio, vertical force and inclination), and the effect of other inputs cannot be studied without creating a new model structure. In the following paper, a flexible model structure will be introduced for predicting lateral and longitudinal forces under combined slip conditions. The model structure will allow for an arbitrary number of additional inputs beyond longitudinal slip, lateral slip, and vertical force to be included in the tire model in a general manner.

The following sections begin with a brief background of the Magic Formula and the associated Pacejka/DelftTire models followed an introduction to Nondimensional Tire Theory. The structure of the proposed model will then be introduced, as well as a statistical process for fitting pure slip conditions. This methodology is then extended and applied to combined lateral and longitudinal slip conditions. The fitting process will be applied to data provided by the Formula SAE Tire Testing Consortium (TTC) [1] and collected on the flat track testing machine at Calspan's Tire Research Facility.

## 2.2. Background

The following sections are brief introductions to Magic Formula tire models and Nondimensional Tire Theory.

### 2.2.1. Pacejka - Delft Tire

The Magic Formula, shown in its most basic form in (1), is the basis of a semi-empirical model, which was developed in the '80s by Bakker, Nyborg and Pacejka [2]. Since its original formulation, updated versions have extended the model to enhance its capabilities. Models developed in this series (e.g., Pacejka '89, MF-TYRE 6.1) will be referred to in general as "MF" models. The ability of MF tire models to represent accurately a wide range of tire behavior, as well as extensive documentation and public availability has led to their widespread use including integration with many commercial vehicle dynamics software packages. A more complete background of MF models can be found in [3].

$$R = D \sin\{C \arctan[B(1 - E)\kappa + E \arctan(B\kappa)]\} \quad (1)$$

One of the most significant advantages of the MF models has been the consistent structure of the model which has allowed it to become very widely used, but this standardization is also one of its disadvantages, as there is no provision for extending the model to include additional inputs. For example, MF-TYRE 5.2 and earlier all include vertical force, slip angle, slip ratio and inclination as the standard inputs, but do not include the effect of inflation pressure. In [4] and [5] modifications to version MF-TYRE 5.2 are proposed to incorporate the effect of tire pressure. This new structure allows inflation pressure to be included in the fit, but the fit is still limited to parameters that are “built in” to the model and there is not a simple way of adding additional parameters. In order to study the effect of an additional parameter, the structure needs to be revised. This shortfall is the primary motivation for the development a model structure capable of accommodating arbitrary inputs.

### 2.2.2. Nondimensional Tire Theory

An alternative semi-empirical modeling method that also relies on the Magic Formula is Nondimensional Tire Theory. The primary goal of Nondimensional Tire Theory is the compression of tire data (e.g., slip angle sweeps at various vertical loads and inclinations) to a single curve using normalizing parameters such as the coefficient of friction and cornering stiffness. The resulting normalized curve has a peak of one as well as a slope through the origin of one. The process of data compression is performed on both cornering data, as well as drive/brake data.

Early implementations of Nondimensional Tire Theory [6,7] were based heavily on the physically derived Fiala tire model [8]. It was not until [9] that the Magic Formula was integrated into Nondimensional Tire Theory. A single instance of the Magic Formula (a single set of the parameters  $B$ ,  $C$ ,  $D$  and  $E$ ) and the relevant nondimensional parameters was used to represent normalized force data. At this point, the “friction cake model” from was also introduced which described combined lateral and longitudinal slip behavior. A concise overview of this implementation of Nondimensional Tire Theory can be found in either [10] or [11].

Some normalizing parameters vary with respect to operating conditions (vertical load, inclination, etc.) and in [12], polynomials are used to represent nondimensional parameters such as cornering stiffness and coefficient of friction. This was the first use of the response surface methodology in Nondimensional Tire Theory. This methodology is formalized and expanded in [13,14,15] to include additional inputs of inclination (previously combined with slip angle via inclination stiffness) and inflation pressure, as well as higher order polynomial terms. In [15] the response surface methodology is also applied to the Magic Formula parameters themselves. Specifically,  $E$  is allowed to vary with vertical load as a means for allowing different characteristic Magic Formula shapes (or peak locations). Although the response surface methodology was not specifically generalized, the concept was established that could easily lead to any model parameter varying with respect to any inputs.

In addition to pure longitudinal and lateral slip conditions, [15] also extends the response surface methodology to combined slip conditions by using the slip parameters themselves (slip ratio and slip angle) as inputs to various response surfaces (e.g., cornering stiffness as a function of slip ratio and longitudinal stiffness as a function of slip angle). The concept has promise, but it is not fully developed and the results are not compelling enough to justify use of this method. Instead, the cosine Magic Formula method, originally developed in [16], was used to develop the models presented in this paper. This is the same type of method used in the MF models since Pacejka '97. The method used in this work is similar to the method used in [3] with some changes to incorporate the response surface methodology.

Despite the differences in the representations between the MF and nondimensional methodologies, the resulting models are quite similar. The primary difference is that the MF tire models assume a specific structure (that may be less general but potentially more physically relevant) than non-dimensional tire models, which are fit with polynomial response surfaces of arbitrary order. A significant challenge that comes with the response surface methodology is the selection of which polynomial terms to include. In the following work, this challenge is overcome by selecting terms based on their statistical significance. This process will be demonstrated by creating a model with inclination, inflation pressure, and rim width as inputs in addition to the required slip ratio, slip angle and vertical force.

## 2.3. Pure Slip Model Structure

This section defines the normalizing transforms, introduces a simplified Magic Formula model, and presents polynomial response surfaces. The structure is shown using the pure longitudinal slip model as an example. The structure of the pure lateral slip model is similar, with  $x$  subscripts replaced with  $y$  and slip ratio  $\kappa$  replaced with slip angle  $\alpha$ . Other differences are noted as necessary.

### 2.3.1. Nondimensional Transform

The first step in the transform is to perform horizontal and vertical shifts such that the linear portion of the force curve is centered at the origin. This is accomplished by identifying the maximum slope of the force vs. slip curve (maximum longitudinal stiffness) and shifting the coordinates of this point to the origin. Longitudinal stiffness  $C_x$ , as well as normalized horizontal and vertical shifts  $\bar{S}_{Hx}$  and  $\bar{S}_{Vx}$ , are defined in (2-4). Quantities with an over bar (̄) have been normalized by vertical load  $F_z$ .

$$C_x = \frac{\partial F_x}{\partial \kappa} \Big|_{peak \ C_x} \quad (2)$$

$$\bar{S}_{Vx} = \frac{F_x}{F_z} \Big|_{peak \ C_x} \quad (3)$$

$$\bar{S}_{Hx} = \frac{C_x \kappa}{F_z} \Big|_{peak \ C_x} = \bar{C}_x \kappa \Big|_{peak \ C_x} \quad (4)$$

Normalized longitudinal stiffness, shown in (5), can be used to simplify the transforms and enforce positive values of longitudinal stiffness that decrease to zero at zero vertical force. This is an important characteristic for stable model performance. Normalized longitudinal and cornering stiffness will be used in this development.

$$\bar{C}_x = \frac{C_x}{F_z} \quad (5)$$

After horizontal and vertical shifts are applied, the resulting curve is an intermediate shifted transform that will be designated using a hat ( ^ ) notation. Shifted transformations are defined in (6, 7).

$$\hat{F}_x = F_x - F_z \bar{S}_{Vx} \quad (6)$$

$$\hat{\kappa} = \kappa - \frac{\bar{C}_{Hx}}{\bar{C}_x} \quad (7)$$

The transformation is completed by scaling the shifted force and slip ratio such that the normalized force curve has peak magnitudes and a slope through zero equal to one. This is accomplished using (8-10). In the pure lateral slip model, normalization of slip angle differs from that of slip ratio as noted in (11).

$$\hat{\mu}_x = \left| \frac{\hat{F}_x}{F_z} \right| \Big|_{peak \hat{\mu}_x} \quad (8)$$

$$\bar{F}_x = \frac{\hat{F}_x}{\hat{\mu}_x F_z} \quad (9)$$

$$\bar{\kappa} = \frac{\bar{C}_x \hat{\kappa}}{\hat{\mu}_x} \quad (10)$$

$$\bar{\alpha} = \frac{\bar{C}_y \tan(\hat{\alpha})}{\hat{\mu}_y} \quad (11)$$

Because  $\hat{\mu}_x$  may not be equal for driving and braking conditions,  $\hat{\mu}_x^+$  and  $\hat{\mu}_x^-$  are defined for  $\hat{\kappa}$  greater than and less than zero respectively but for the remainder of this development the + and - superscripts will be dropped and it is assumed that the appropriate  $\hat{\mu}_x$  is used based on the sign of  $\hat{\kappa}$ . It should also be noted that although  $\hat{\mu}_x$  may be referred to as a coefficient of friction, it is not strictly a coefficient of friction due to the vertical shift  $S_{Vx}$ . Coefficients of friction can be recovered using (12, 13).

$$\mu_x^+ = \hat{\mu}_x^+ + \bar{S}_{Vx} \quad (12)$$

$$\mu_x^- = \hat{\mu}_x^- - \bar{S}_{Vx} \quad (13)$$

The complete force and slip transforms can be condensed into (14-17).

$$\bar{F}_x = \frac{1}{\hat{\mu}_x} \left( \frac{F_x}{F_z} - \bar{S}_{Vx} \right) \quad (14)$$

$$\bar{\kappa} = \frac{1}{\hat{\mu}_x} (\bar{C}_x \kappa - \bar{S}_{Hx}) \quad (15)$$

$$\bar{F}_y = \frac{1}{\hat{\mu}_y} \left( \frac{F_y}{F_z} - \bar{S}_{Vy} \right) \quad (16)$$

$$\bar{\alpha} = \frac{\bar{C}_y}{\hat{\mu}_y} \tan \left( \alpha - \frac{\bar{S}_{Hx}}{\bar{C}_y} \right) \quad (17)$$

If the force curve is nearly linear at zero force, then the transforms can be simplified by removing the vertical shift. The resulting transformations are shown in (18-21).

$$\bar{F}_x = \frac{F_x}{\mu_x F_z} \quad (18)$$

$$\bar{\kappa} = \frac{1}{\mu_x} (\bar{C}_x \kappa - \bar{S}_{Hx}) \quad (19)$$

$$\bar{F}_y = \frac{F_y}{\mu_y F_z} \quad (20)$$

$$\bar{\alpha} = \frac{\bar{C}_y}{\mu_y} \tan \left( \alpha - \frac{\bar{S}_{Hy}}{\bar{C}_y} \right) \quad (21)$$

### 2.3.2. Simplified Magic Formula

The Magic Formula used here is modified slightly from its typical form based on constraints of Nondimensional Tire Theory. These constraints are the normalization of the peak magnitude, as well as the normalization of the slope through the origin, expressed in (22, 23).

$$D = 1 \quad (22)$$

$$BCD = 1 \quad (23)$$

After substituting these constraints into the Magic Formula and eliminating the parameters  $C$  and  $D$ , we are left with the resulting simplified Magic Formula shown in (24).

$$\bar{F}_x = \sin \left\{ \frac{1}{B_x} \arctan[B_x(1 - E_x)\bar{\kappa} + E \arctan(B_x\bar{\kappa})] \right\} \quad (24)$$

By enforcing these constraints and removing the extra parameters from the initial model structure, the constraints will always be respected, and the number of model parameters that need to be stored and calculated is reduced.

Like  $\hat{\mu}_x$ , the Magic Formula parameters  $B_x$  and  $E_x$  may not be equal for driving and braking and are also defined separately depending on the sign of  $\hat{\kappa}$ . Similarly, + and – superscripts will not be shown unless additional clarity is required.

### 2.3.3. Model Parameter Response Surfaces

The normalizing parameters  $\mu$  and  $\bar{C}$ , shift parameters  $\bar{S}_V$  and  $\bar{S}_H$ , and Magic Formula parameters  $B$  and  $E$ , are all represented using polynomial response surfaces such as the response surfaces shown in figure 1. The general form used to create this surface is shown in (25), with vertical force  $F_z$  and inclination angle  $\gamma$  as inputs. Constants  $p_n$  are polynomial parameters determined from a least squares fit of the data. Black dots represent the data points that were used to fit the surface.

$$\mu_x = p_0 + p_1 F_z + p_2 \gamma + p_3 F_z^2 + p_4 \gamma^2 + p_5 F_z \gamma \quad (25)$$

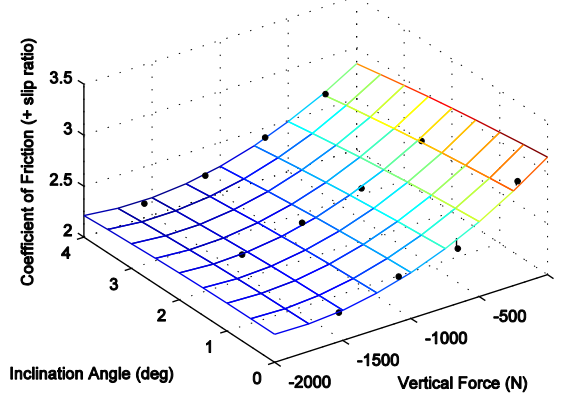


Figure 1: Quadratic fit of longitudinal coefficient of friction

## 2.4. Fitting Pure Slip Model Parameters

This section details how model parameters are collected from raw tire data, and how polynomial surfaces are fit to these parameters. The terms included in the polynomial are chosen using statistical significance as a selection criterion. The following development also uses the longitudinal pure slip case as an example but can be applied to the lateral slip case as well.

### 2.4.1. Description of Test Data

The TTC is a group formed by students and industry professionals with the goal of providing high quality tire data for student engineers [1]. Data collected by the TTC will be used to demonstrate the fitting process in the following sections. The data is primarily used by Formula SAE and Formula Students teams that compete in collegiate engineering design events around the world. The data provided is very structured, and this structure is relied on during the fitting process demonstrated below. The data used here is from a Hoosier bias ply racing tire.

Data was collected in two types of tests; free rolling tests that focus on lateral slip behavior by performing slip angle sweeps, and drive/brake tests that focus on longitudinal slip by performing slip ratio sweeps. Combined slip behavior is also evaluated during the drive/brake test by performing slip ratio sweeps at non-zero slip angles. In both test types, slip sweeps are performed at multiple vertical loads, inclinations and inflation pressures to fill out a test matrix. The tests are repeated for three different rim widths.

### 2.4.2. Identifying Normalization and Shift Parameters

In order to identify the effects of hysteresis, slip sweeps are performed in groups that include both positive and negative slip rates. Slip ratio sweeps are performed in pairs as shown in figures 2 and 3, with one negative slip-rate sweep followed by one positive slip-rate sweep. Slip angle sweeps are performed in groups of three as shown in figures 4 and 5, with two positive slip-rate sweeps and one negative slip-rate sweep. The first and last slip angle sweeps are partial sweeps that start and end at an intermediate slip angles respectively.

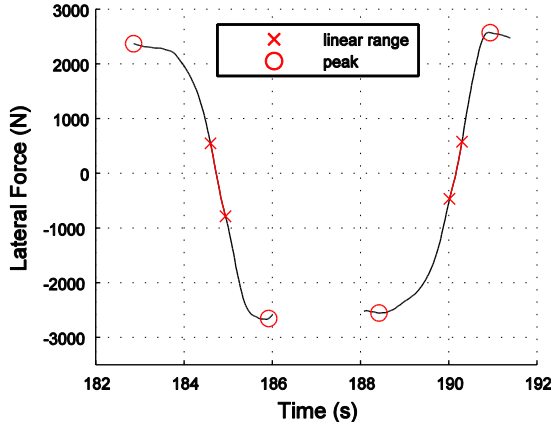


Figure 2: Longitudinal sweep group - force plotted vs. time

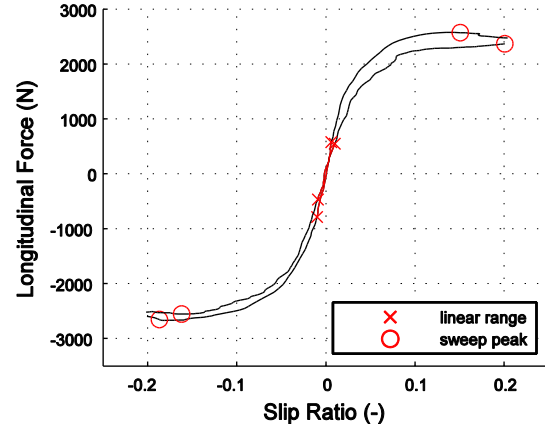


Figure 3: Longitudinal sweep group - force plotted vs. slip ratio

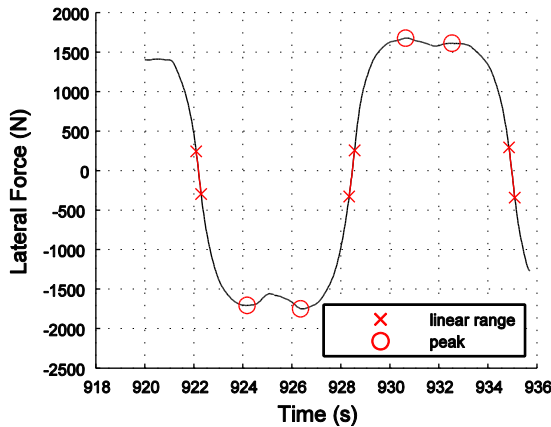


Figure 4: Lateral sweep group - force plotted vs. time

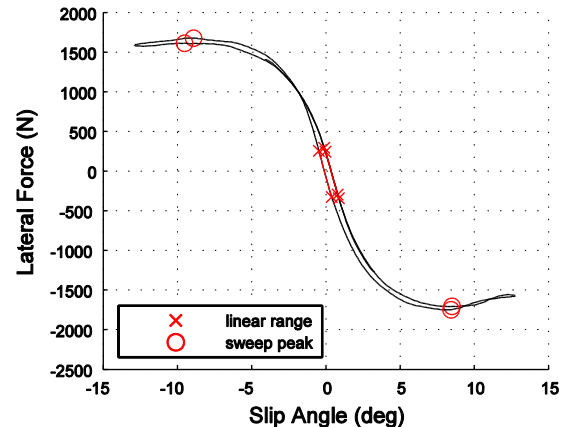


Figure 5: Lateral sweep group - force plotted vs. slip ratio

To identify the longitudinal stiffness  $C_x$  as well as the shift parameters  $S_V$  and  $S_H$ , for each slip sweep, a third order polynomial is fit to a region centered on zero force that covers a range up to 30% of the slip ratio at peak force. This polynomial is twice differentiated and set equal to zero to locate the maximum slope, which identifies the center of the linear region. Shift parameters and cornering stiffness are calculated from the polynomial coefficients as shown in (26-29).

$$F_x = a\kappa^3 + b\kappa^2 + c\kappa + d \quad (26)$$

$$S_H = -\frac{b}{3a} \quad (27)$$

$$S_V = aS_H^3 + bS_H^2 + cS_H + d = \frac{-b^3}{27a^2} + \frac{b^3}{9a^2} - \frac{cb}{3a} + d \quad (28)$$

$$C_x = 3aS_H^2 + 2bS_H + c = \frac{b^2}{3a} - \frac{2b^2}{3a} + c \quad (29)$$

If the vertical shift is neglected, a first order polynomial can be fit to a region centered on zero force, which covers a range up to 5% of the slip ratio at peak force. The fit parameters are used to define the slope and offsets as shown in (30-33).

$$F_x = c\kappa + d \quad (30)$$

$$S_H = -\frac{d}{c} \quad (31)$$

$$S_V = 0 \quad (32)$$

$$C_x = c \quad (33)$$

Once the normalization and shift parameters are collected for all sweeps within a group, they are averaged to determine the nominal values for the particular input case. In the lateral slip case, some care must be taken with this averaging, as a simple average can lead to a bias in  $S_{VY}$ ,  $S_{HY}$  and  $C_y$  because there are two positive slip rate sweeps and only a single negative slip rate sweep. In order to center the hysteresis loop, positive and negative slip rate sweeps must be equally weighted when averaged. A simple solution to this is to average the values from the two positive slip rate sweeps, then average that result with the value from the single negative rate slip sweep.

For each sweep, maximum and minimum normalized forces are recorded, but only some of these values will be representative of the true force peaks. As discussed above, cornering tests are made up of three sweeps, the first and last of which are only partial sweeps. When a partial sweep starts or ends with an intermediate slip angle, the normalized force associated with this slip angle is usually a maximum or minimum, but is not representative of a coefficient of friction.

When this is the case, these intermediate slip maxima or minima are disregarded. This is not an issue for drive brake test because there are no partial slip sweeps.

In both cornering and drive/brake test, four coefficients of friction will be measured. Two will be at positive slip angles, and two at negative slip angles. For both of these pairs, one is collected during a slip sweep with a positive slip rate and the other is collected during a slip sweep with a negative slip rate. The coefficients of matching slip sign are averaged to determine the nominal value for that sign.

### 2.4.3. Identifying Magic Formula Parameters

Once the normalization and shift parameters are collected, they are used to transform their respective sweep groups to the nondimensional space. This normalization results in a curve with a zero crossing centered on the origin with a slope of one and peak magnitudes in each direction of one. This normalized data is used to fit two instances of the simplified Magic Formula to each slip group, one for positive slip and another for negative slip. The Magic Formula parameters are fit using the MATLAB function “fminsearch” which uses a simplex search method to minimize the value of the function shown in (34). Figures 6 through 9 show examples of longitudinal and lateral sweep groups that have been normalized and fit with the Magic Formula in this manner.

$$\bar{E}_y = \sum_{i=1}^n (R_i - \bar{F}_i)^2 \quad (34)$$

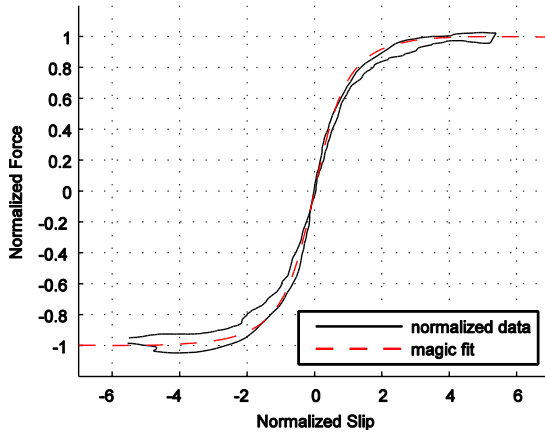


Figure 6: Normalized longitudinal force fit with the Magic Formula

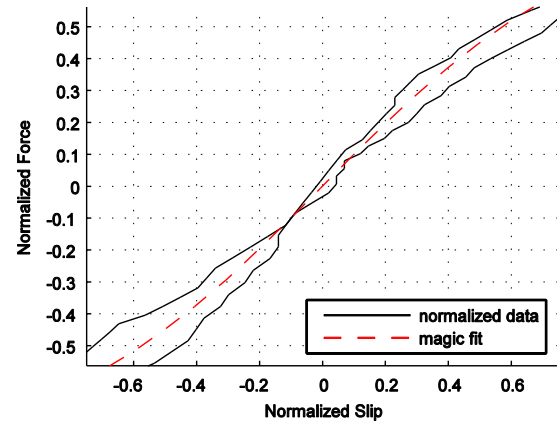


Figure 7: Normalized longitudinal force fit with the Magic Formula – zero crossing

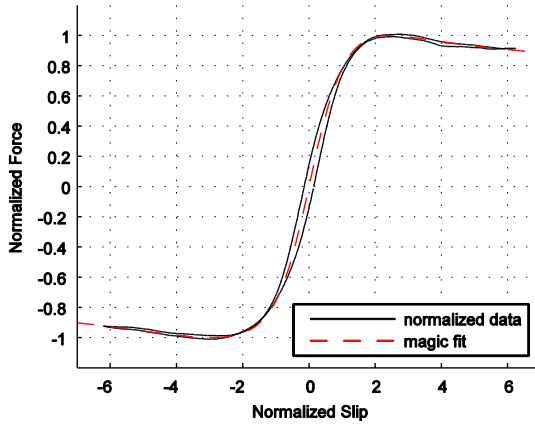


Figure 8: Normalized lateral force fit with the Magic Formula

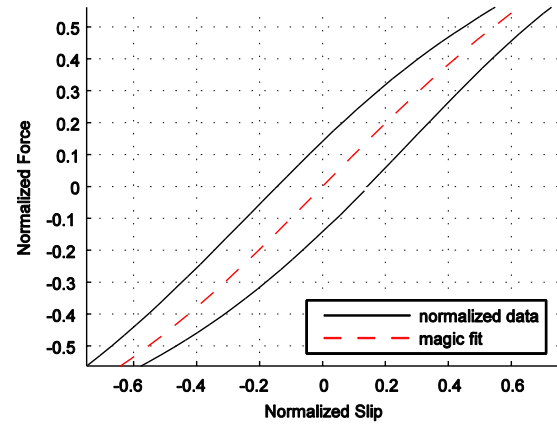


Figure 9: Normalized lateral force fit with the Magic Formula – zero crossing

#### 2.4.4. Fitting Response Surfaces

Once model parameters have been collected for all slip groups, polynomial response surfaces are fit so that parameters can be estimated continuously. This is accomplished by solving the system of equations for the weighted least squares solution. A typical choice of weighting is to use vertical force, which more heavily weights data points collected at higher loads in order to minimize absolute error. If equal weighting is used for all points then the total relative error across all loads will be minimized. Figures 10 through 15 show zero order (constant), first order

(linear) and second order (quadratic) fits to longitudinal and cornering stiffness values with vertical force weighting. Lines extending from data points represent their vertical distance from the response surface. Mesh surfaces are colored based on their vertical axis values.

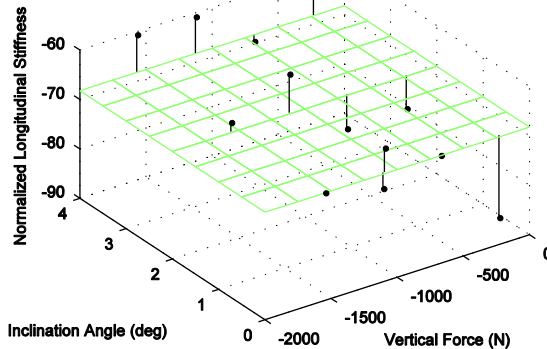


Figure 10: Zero order fit of normalized longitudinal stiffness

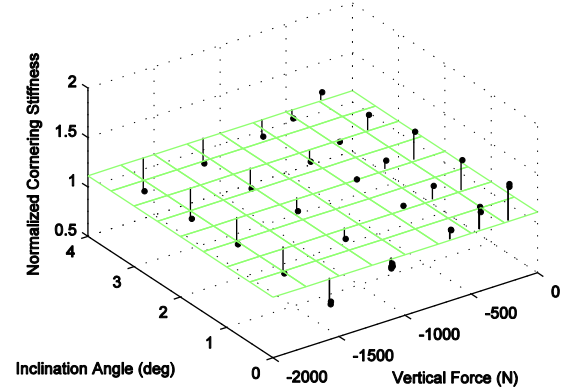


Figure 11: Zero order fit of normalized cornering stiffness

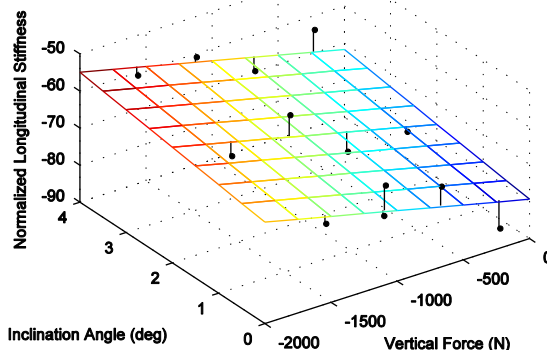


Figure 12: Linear fit of normalized longitudinal stiffness

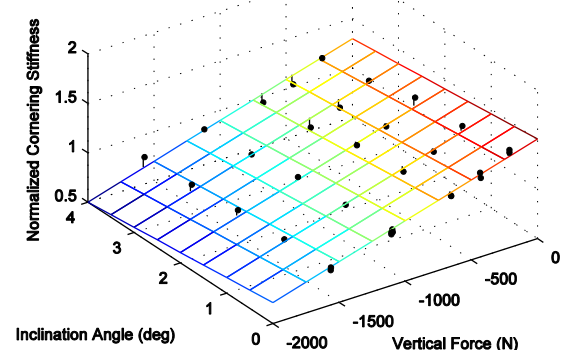


Figure 13: Linear fit of normalized cornering stiffness

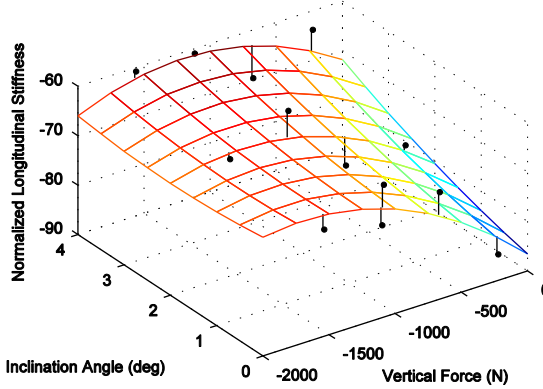


Figure 14: Quadratic fit of normalized longitudinal stiffness

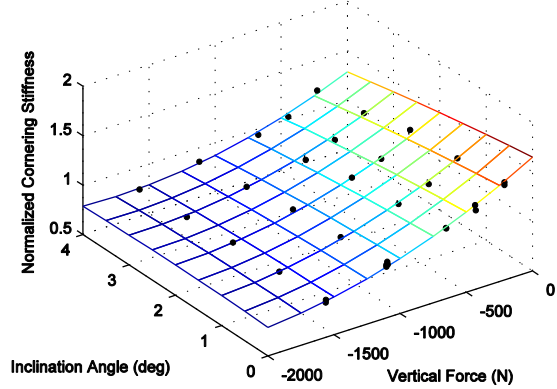


Figure 15: Quadratic fit of normalized cornering stiffness

The general forms of the three response surfaces are shown in (35-37).

$$\bar{C} = p_0 \quad (35)$$

$$\bar{C} = p_0 + p_1 F_z + p_2 \gamma \quad (36)$$

$$\bar{C} = p_0 + p_1 F_z + p_2 \gamma + p_3 F_z^2 + p_4 \gamma^2 + p_5 F_z \gamma \quad (37)$$

#### 2.4.5. Determining Model Order

To determine what terms should be included in the response surface, a fully populated polynomial of sufficiently high order is used as a starting point for fitting. Parameters may be removed for two reasons. First, higher order terms of some model inputs should not be included because data has not been collected at enough levels for a fully determined solution. For example, when a set of data for a given tire only includes two inflation pressures, terms above linear with respect to that input should not be included because fitting will be unstable and could result in trends that are not representative of the collected data. Figure 16 shows a quadratic response surface fit to coefficient of friction data measured at three vertical loads and two pressures. Figure 17 is a 2-dimensional representation of this same curve at a single vertical load. In this case, there is a strong quadratic character to the response. On this response surface, the coefficient of friction varies between negative four, which does not make physical sense, and nine, which is well outside realistic values of coefficient of friction. In order to avoid these errors, any terms of higher order that are inappropriate are removed.

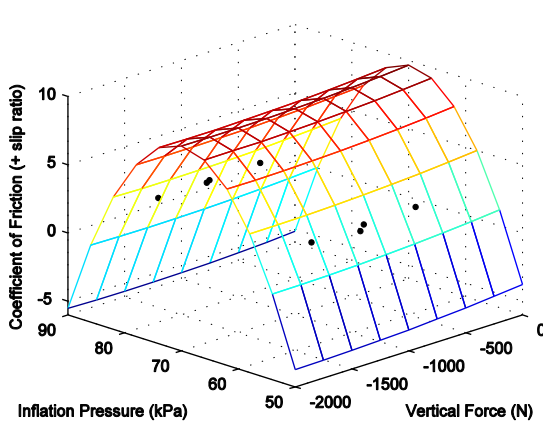


Figure 16: High order response surface fit to low order data

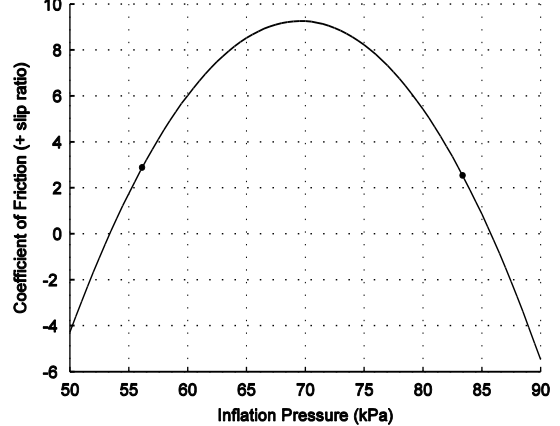


Figure 17: High order response curve fit to low order data

The second reason that some terms should be removed is that they do not contribute significantly to the quality of the response fit. One method for determining which parameters are important is to manually remove parameters and observe the effect on the value of the error (e.g., mean squared error), and on the visual fit of response surface. This can lead to acceptable fits, but it is preferable to have a process that is more objective and automated.

A process for determining important model parameters based on statistical significance is outlined in figure 18. The process begins with the fully populated response as a candidate fit, and a reduced fit is formed by removing the least significant term. The least significant term is the term that, when removed, causes the smallest increase in the weighted residual sum of squares error (RSS). Using the candidate model and the reduced model, an F-statistic is calculated using (38). The F-statistic is compared to  $F_{crit}$ , the F-statistic for  $(n_C - n_R, d - n_C)$  degrees of freedom for a given false rejection probability  $p$  (e.g., 5%).  $RSS_C$  and  $RSS_R$  are the respective weighted errors for the candidate and reduced fits,  $n_C$  and  $n_R$  are the number of parameters in each of the fits and  $d$  is the total number of data points being fit. If the calculated F-statistic is greater than  $F_{crit}$  then the reduced response becomes the new candidate response and the process is repeated. This continues until either the fit reduces to zero order (constant), or the effect of removing an additional term no longer improves the significance of the model. The choice of the false rejection probability  $p$  can be used to control the error of the response fits as well as the number of fit parameters used.

$$F = \frac{\left( \frac{RSS_R - RSS_C}{n_C - n_R} \right)}{\left( \frac{RSS_C}{d - n_C} \right)} \quad (38)$$

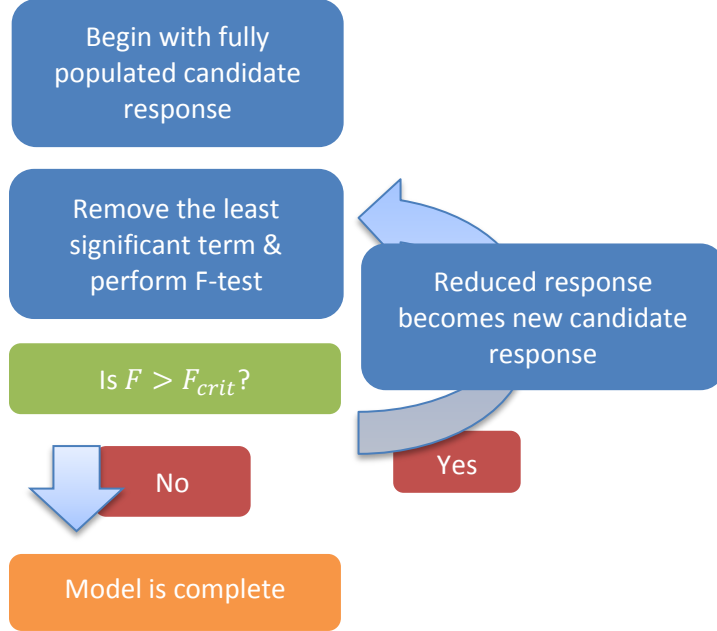


Figure 18: Flow chart for pure slip response fit order selection

## 2.5. Combined Slip Model

The combined slip method used here is similar to the method used in [3], which contains a development of greater depth than will be presented here. Several simplifications are made and the response surface methodology that was applied in the pure slip cases will be applied here as well.

### 2.5.1. Interaction Response Surface Definition

The cosine version of the Magic Formula (39, 40) is used as a weighting function for the effect of slip angle on longitudinal force. Like the sine version, the parameters  $B$ ,  $C$ ,  $D$  and  $E$  are used to control the shape of the resulting curves.

$$G_{x\alpha} = D \cos\{C \arctan[B(1 - E)\alpha + E \arctan(B\alpha)]\} \quad (39)$$

$$B = B_1 \cos\{\arctan(B_2 \kappa)\} \quad (40)$$

- $D$  scales the magnitude of the entire curve
- $C$  determines values at the extreme ends of the curve
- $B$  sets the curvature at the peak
- $E$  is used to broaden or narrow the outer part of the curve.

The weight function has the property that at zero slip angle, it will be equal to one, leaving the pure longitudinal slip condition unchanged. For slip angle values other than zero, the weight  $G_{x\alpha}$  will be less than one, reducing the predicted force. The level of interaction between the two slip parameters depends on their relative magnitudes. At large values of slip ratio, changes in slip angle will not significantly affect longitudinal force compared to the same slip angle change at smaller slip ratios. This is accomplished by varying the parameter  $B$  as a function of longitudinal slip as shown in (40). Representative response surfaces for longitudinal and lateral combined slip are shown in figures 19 and 20.

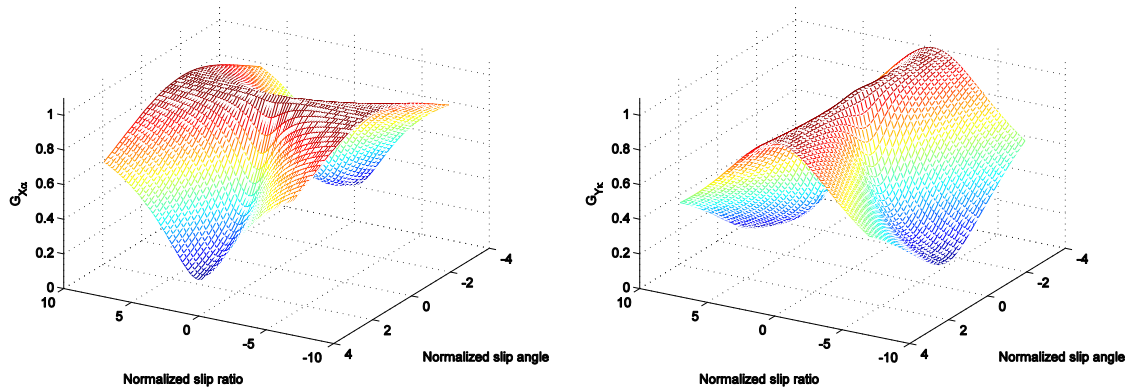


Figure 19: Longitudinal combined slip weight

Figure 20: Lateral combined slip weight

Once again, several simplifications can be made. First, the peak magnitude of  $G_{x\alpha}$  should be one, so the parameter  $D$  is not needed. In addition,  $G_{x\alpha}$  can be forced to go to zero for very large values of  $\alpha$ . This is accomplished by setting  $C$  equal to one. The result of these changes is the simplified version of (39) shown in (41).

$$G_{x\alpha} = \cos\{\arctan[B_{x\alpha}(1 - E_{x\alpha})\alpha + E_{x\alpha} \arctan(B_{x\alpha}\alpha)]\} \quad (41)$$

$$B_{x\alpha} = B_{x\alpha 1} \cos\{\arctan(B_{x\alpha 2}\kappa)\} \quad (42)$$

One additional change is advisable for the lateral force interaction weight  $G_{y\kappa}$ . According to [3] the interactions between lateral and longitudinal forces often result in peak lateral force occurring at some value other than zero slip ratio, with a magnitude slightly larger than measured in the pure lateral slip condition. To account for this, the shift parameter  $S_{Hy\kappa}$  is introduced, as well as the modified version of the cosine Magic Formula, shown in (43-45). The magnitude of the weighting function  $G_{y\kappa}$  remains equal to one at zero slip ratio, but now peaks at a slip ratio of  $-S_{Hy\kappa}$ .

$$G_{y\kappa} = \cos\{\arctan[B_{y\kappa}(1 - E_{y\kappa})(\kappa + S_{Hy\kappa}) + E_{y\kappa} \arctan(B_{y\kappa}(\kappa + S_{Hy\kappa}))]\} / G_{Hy\kappa} \quad (43)$$

$$G_{Hy\kappa} = \cos\{\arctan[B_{y\kappa}(1 - E_{y\kappa})S_{Hy\kappa} + E_{y\kappa} \arctan(B_{y\kappa}S_{Hy\kappa})]\} \quad (44)$$

$$B_{y\kappa} = B_{y\kappa 1} \cos\{\arctan(B_{y\kappa 2}\alpha)\} \quad (45)$$

### 2.5.2. Fitting Interaction Response Surfaces

The interaction parameters  $B_{x\alpha 1}$ ,  $B_{x\alpha 2}$ , and  $E_{x\alpha}$ , are all represented with polynomials in the same way as the pure slip parameters, but the way they are determined is different. This is due to several challenges that have to be overcome in order to fit the interaction response surfaces. The first is that the pure longitudinal sweeps and combined slip sweeps are performed in a single test, but the pure lateral slip sweeps are performed in a separate test. When the lateral forces from the pure lateral slip test are compared to similar conditions (e.g., same slip angle, slip ratio, vertical force, etc.) in the combined slip test, the resulting lateral forces are very different. One possible explanation for the discrepancy is that much more energy is put into the tire during the pure longitudinal slip and combined slip sweeps as compared to the pure lateral slip test, resulting in higher temperatures. This is supported by the significantly higher surface temperatures measured during the longitudinal and combined slip test. The increased temperatures could cause significant changes in tire behavior (e.g., change the coefficient of friction and/or cornering stiffness). In order to make use of the lateral force data from

combined slip tests, it is normalized so that the lateral force is equal to one at zero slip ratio. This normalized data represents the shape of the interaction weighting,  $G_{y\kappa}$ , and is used to fit the response surface. The pure longitudinal slip sweeps are conducted under the same conditions as the combined slip test, so the longitudinal forces are normalized by the longitudinal force expected for the pure slip conditions, which results in the in the interaction weighting  $G_{x\alpha}$ .

A second challenge is that, unlike the pure slip test, the interaction Magic Formula is a function of both slip parameters, making it unstable to fit all the parameters of a single instance of the cosine Magic Formula to a single sweep group. Instead, all of the combined slip data is collected into a single dataset that is used to fit a single instance of the interaction response surface. This is done to fit both lateral and longitudinal interaction response surfaces.

Since the interaction curves cannot be fit to each slip group independently, the polynomial response surfaces for each Magic Formula parameter cannot be fit using the simple linear least squares process used in the pure slip case. Instead, all of the response surfaces are determined simultaneously. This means, instead of determining two parameters ( $B$  and  $E$ ) for a single pure slip Magic Formula, four polynomial response surfaces with an arbitrary number of terms have to be determined at once. If terms up to second order are included and three inputs are used, 40 terms will be included in the interaction response. This increase in complexity significantly increases computation time to the point where starting with a fully populated model is not practical. To speed the fitting process an alternative process is illustrated in figure 21. Unlike the pure slip case, a zero order model is used as the starting point and the most significant term is added until new terms no longer significantly reduce the error of the model. In this case, the most significant term is the one that, when added, most reduces the weighted residual sum of squares. Similar to the pure slip response surface fitting, significance is tested using the F-statistic in (46). In this case,  $RSS_C$  and  $RSS_I$  are the respective weighted errors for the candidate and increased order fits,  $n_C$  and  $n_I$  are the number of parameters in each of the fits and  $d$  is the total number of data points being fit.

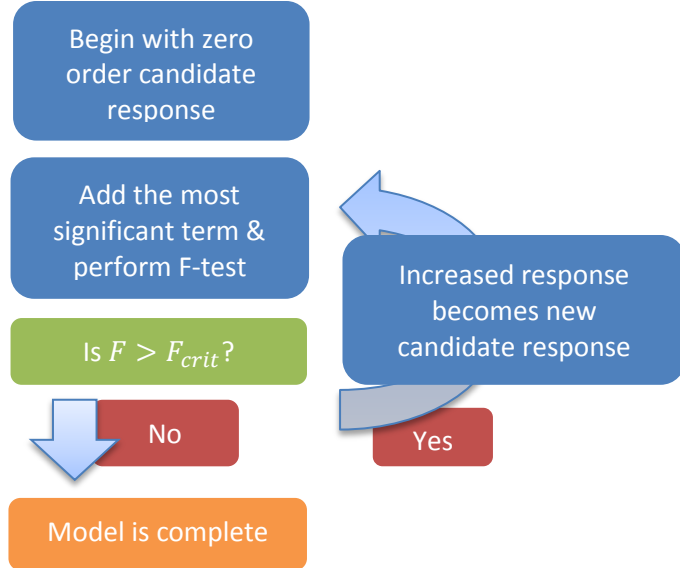


Figure 21: Flow chart for interaction response fit order selection

$$F = \frac{\left( \frac{RSS_C - RSS_I}{n_I - n_C} \right)}{\left( \frac{RSS_R}{d - n_I} \right)} \quad (46)$$

There is some loss of generality with this method because when the model order is increased, the previous model is used as a starting point for the next model, which could result in the solution search settling in a local minimum. Despite the reduced generality, this method provides acceptable results that will be discussed further in the following section. Figures 22 and 23 show data at a vertical force of 1090 N fit to their respective interaction response surfaces.

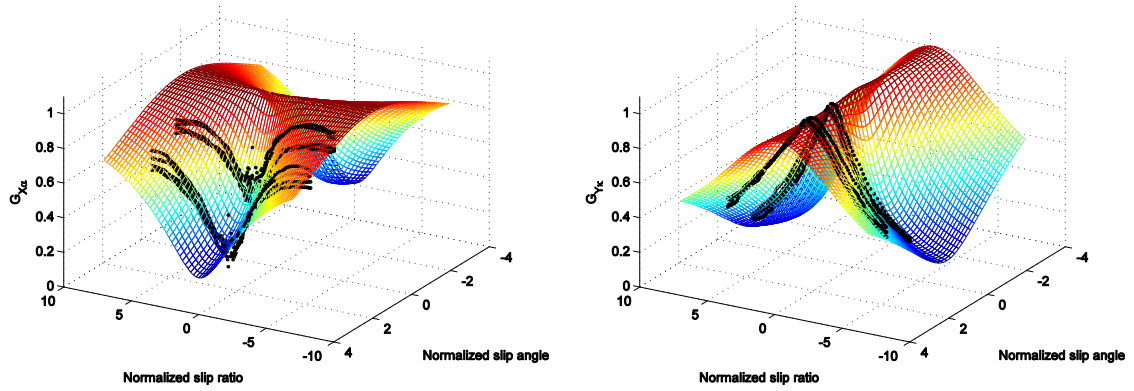


Figure 22: Longitudinal combined slip weighting surface with superimposed data

Figure 23: Lateral combined slip weighting surface with superimposed data

Figures 24 and 25 show results from slip ratio sweeps performed at slip angles of  $3^\circ$  and  $6^\circ$  respectively, as well as an example fit of the data. Sweeps were performed at various vertical loads, as indicated in the figures. Because of the discrepancy between lateral forces measured in pure lateral slip tests, the model values have been scaled by a factor of 0.85. This scaling factor was identified by minimizing the root mean squared error over the entire combined slip test.

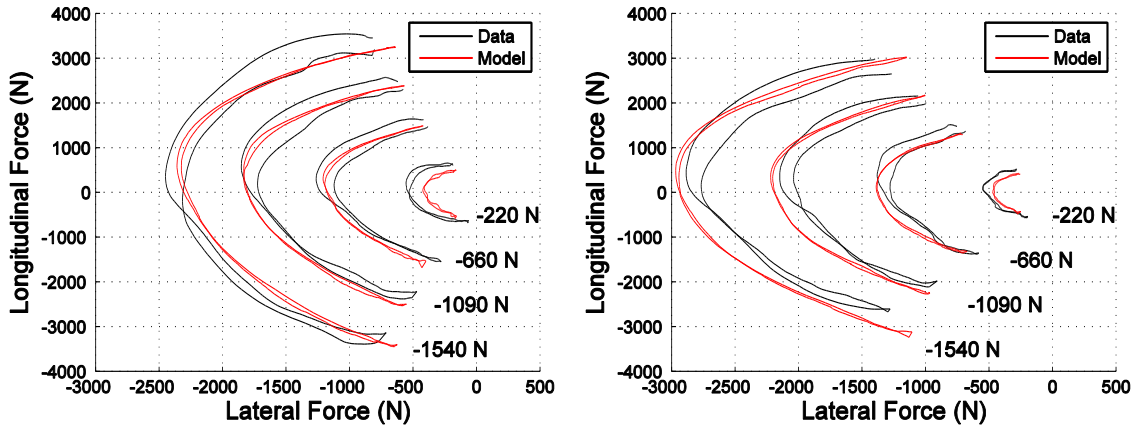


Figure 24: Lateral and longitudinal force for slip ratio sweeps at  $3^\circ$  slip angle

Figure 25: Lateral and longitudinal force for slip ratio sweeps at  $6^\circ$  slip angle

## 2.6. Error Evaluation

Six model types will be used to evaluate the quality of the model structure and fitting process. Three will have pre-determined model structures, with all parameter response surfaces modeled as: zero order (constant), first order (linear), or second order (quadratic). Three will be generated based on the significance criteria described in the previous sections, with significance levels ( $p$ ) of: 0.001, 0.01, and 0.1. Response surface terms up to second order will be evaluated and potentially included. For response surfaces, terms of higher order than appropriate for the data will not be considered (e.g., quadratic fit of two data points).

For each of the six model types, individual models are fit for three different rim widths, with inputs of inclination and inflation pressure in addition to slip ratio, slip angle and vertical load. A fourth model of each type is fit using data from all three rim widths, and includes rim width as an additional input parameter.

To aid in the understanding of fit quality, slip sweeps are broken into separate regions:

- Linear – forces up to 40% of peak force
- Peak – forces within 5% of their respective peak force
- Transition – forces between linear and peak forces
- Saturation – forces beyond peak region (some curves do not saturate)

The region a particular point falls into is determined by the tested values so that the points included in each region are independent of the model used. Figures 26 and 27 show pure slip curves for longitudinal and lateral force colored by region.

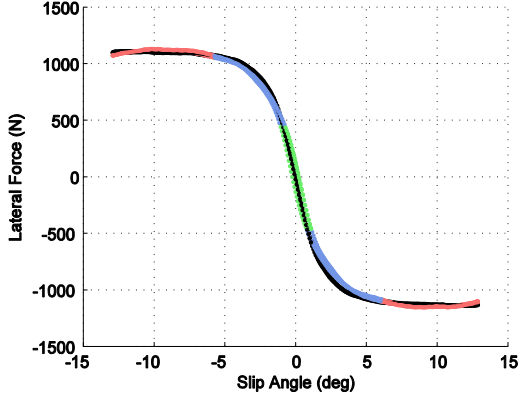


Figure 26: Lateral force vs. Slip angle colored by error region

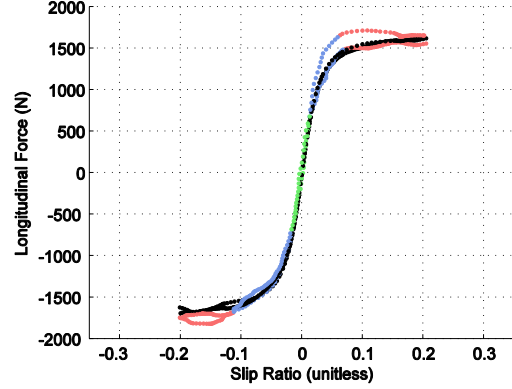


Figure 27: Longitudinal force vs. slip ratio colored by error region

### 2.6.1. Pure Slip

Figures 28 and 29 show the mean absolute error (MAE) for six types of pure longitudinal and lateral slip models which do not include rim width as an input. The error presented for each type is the average of the three constant rim width models. Combined slip weighting is not applied. Each error box is subdivided and colored to show the relative error magnitude of the corresponding regions (upper regions are positive slip and lower regions are negative slip). As expected, the zero order models have the highest error while the fully populated quadratic models have the least error, with the significance models varying between the two. In [15], MAE of approximately 100 N is reported for pure slip models fit to similar data (not including pressure variation or rim width in the test or model structure) which indicates that the error rates presented here are representative of established non-dimensional tire models.

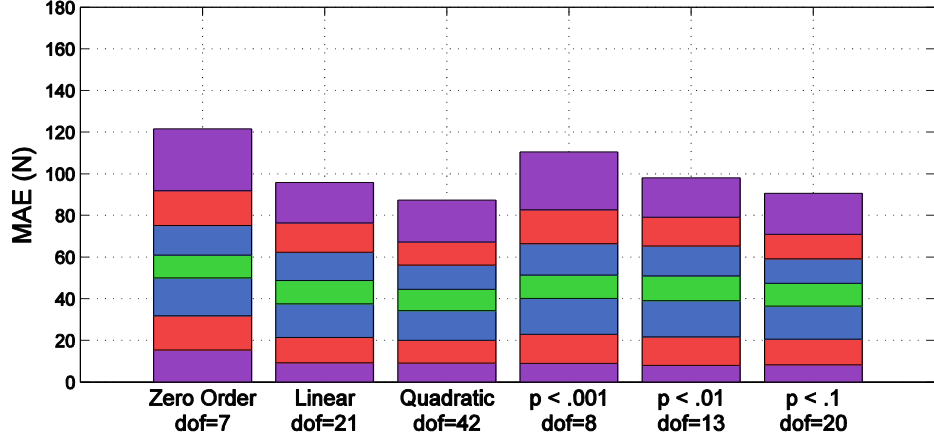


Figure 28: Pure longitudinal slip MAE error colored by error region

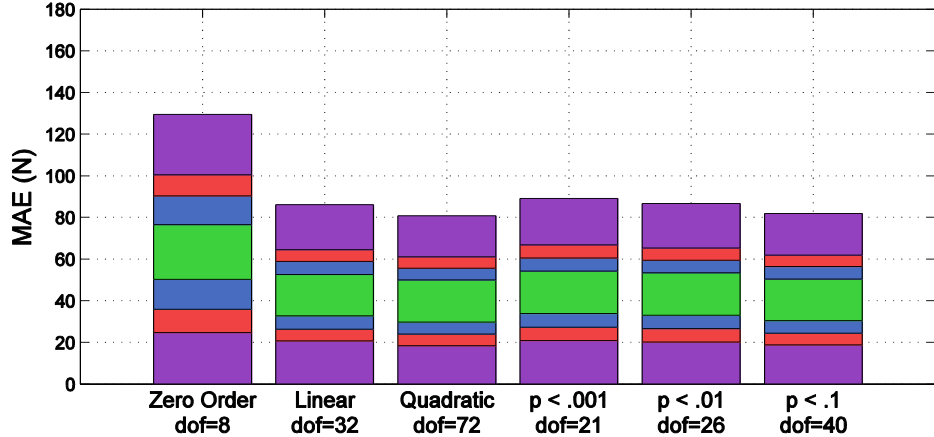


Figure 29: Pure lateral slip MAE error colored by error region

While the error rates are comparable between longitudinal and lateral slip, there tend to be more model parameters included in lateral models for the same significance. This is likely because more lateral slip sweeps are performed, and there is less random variation in the behavior of lateral parameters as can be seen when comparing normalized longitudinal and cornering stiffness in figures 14 and 15. It is also possible that lateral slip behavior requires more parameters to describe accurately.

An example of how the error regions can be used is illustrated by comparing the distribution of error in the models. The total error is similar for lateral and longitudinal slip, but the linear region is a much larger portion of the error in lateral slip test compared to longitudinal. This is

consistent through all model types and is likely due to the hysteresis loop near the origin that is typical of the lateral slip sweeps.

### 2.6.2. Combined Slip

For combined slip, error for each test point is defined as the Euclidian norm of the lateral and longitudinal errors. Figure 30 shows the combined slip MAE computed using data from pure longitudinal and combined slip sweeps, which are collected together during drive/brake test sequences. Due to the discrepancy between lateral forces in pure slip and combined slip tests discussed previously, a single scaling factor is applied to the lateral force data that minimizes the lateral mean squared error for each model.

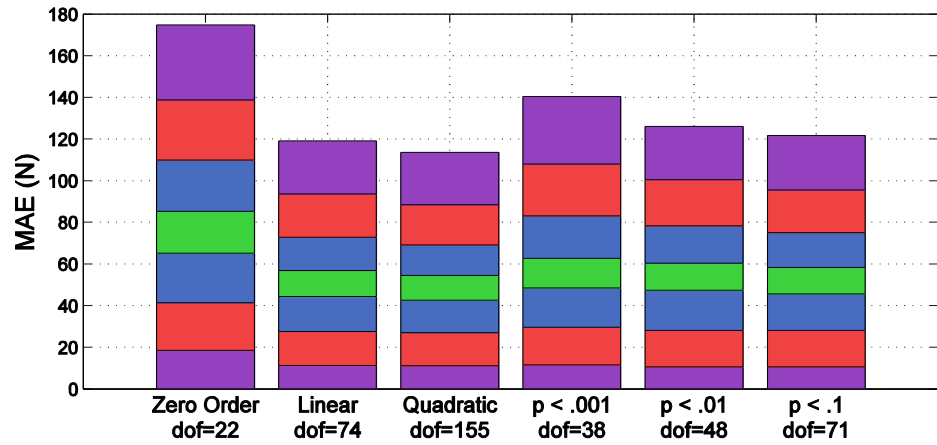


Figure 30: Combined MAE error colored by error region

### 2.6.3. Rim Width

Figures 31 through 33 show the results of pure lateral, pure longitudinal and combined fits that include rim width as an input. With the addition of rim width as an input, the error of the three fixed model structures remains similar to the models without rim width as a parameter. In every case the number of model parameters increases significantly for all model types except the zero order model.

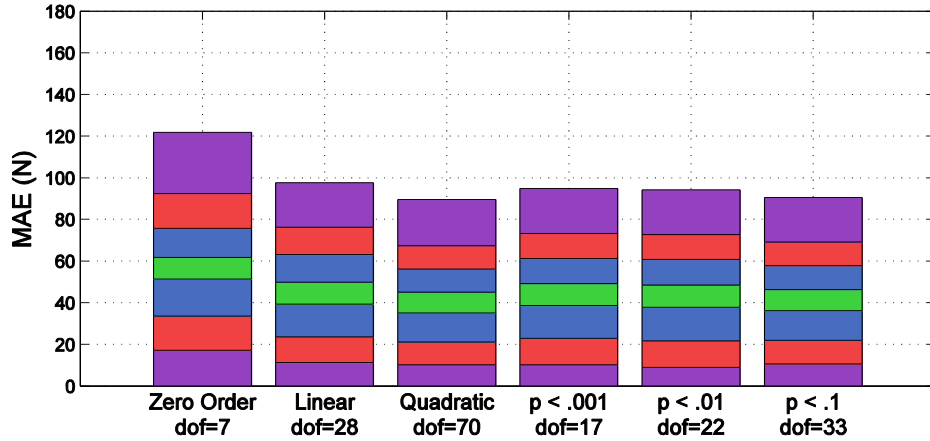


Figure 31: Pure longitudinal slip MAE error colored by error region

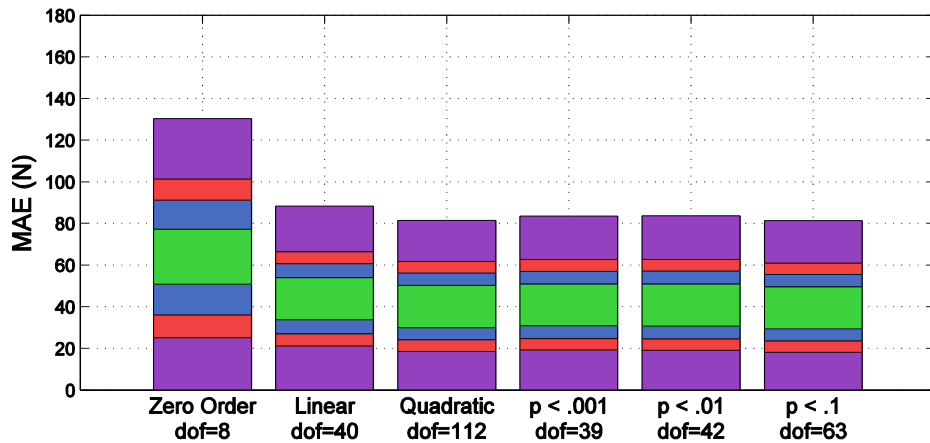


Figure 32: Pure lateral slip MAE error colored by error region

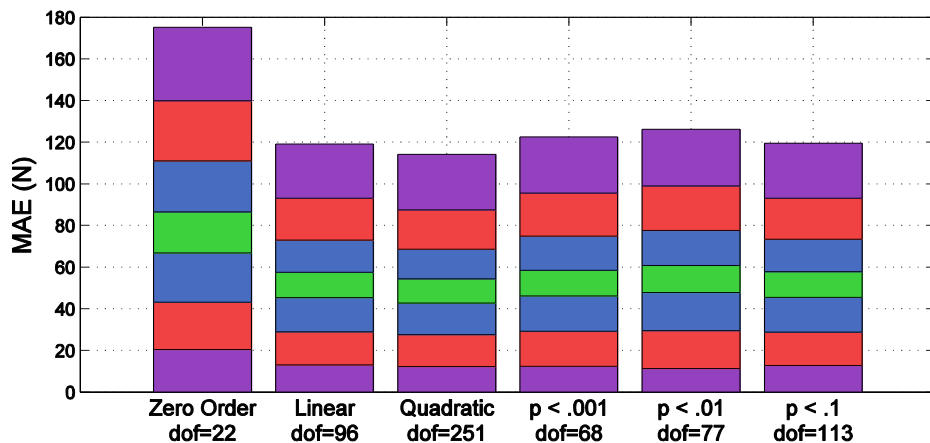


Figure 33: Combined MAE error colored by error region

## 2.7. Future Work

As illustrated by the large mismatch between lateral forces observed in pure slip and combined slip test, tire temperature appears to significantly affect the performance of the tire. Model accuracy could be improved by including thermal effects. Preliminary attempts to include surface tire temperature as an input showed that it is a significant parameter, but unlike the other parameters used, it can vary significantly over a single slip sweep, which complicates the fitting process. In addition, tire surface temperature and vertical load are highly correlated, which can lead to unstable fitting of response surfaces. If tire temperature is to be included as a model input, test sequences designed to vary temperature and load independently should be developed. It is also likely that internal tire temperature, which is not directly measured, is significant. Despite internal tire temperature not being directly measured, the tire's internal temperature could be estimated using a Kalman filter, or similar method, enabling its use as an input parameter.

Hysteresis also appears to be a significant source of error, particularly in the pure lateral slip case. There has not been any published work on dealing with the transient effects directly related to non-dimensional tire theory. Due to their similarity, methods applied to MF models in [3,17] could be adapted to Nondimensional Tire Theory, which could improve the accuracy of the nondimensional models and expand their applicability.

## 2.8. Conclusion

An adaptable model structure for estimating lateral and longitudinal force under combined slip conditions was defined, and a process for selecting its internal parameters based on statistical significance was developed. The quality of the model was evaluated using mean absolute error and is comparable with errors demonstrated by established non-dimensional models, while including additional inputs of inflation pressure and rim width.

### **3. Vehicle Modeling: Creating Milliken Moment Diagrams under general Yaw and Longitudinal Acceleration Conditions**

Abstract: Milliken Moment Diagrams (MMDs) are a useful tool for understanding a wide range of vehicle performance characteristics, and while the theory behind them is well developed, there are several aspects of their creation that present significant challenges. In particular, methods for including longitudinal dynamics are not well covered. This issue is addressed, and a process for generating MMDs over a range of yaw conditions, and longitudinal accelerations is presented.

### 3.1. Introduction

Milliken Moment Diagrams (MMDs) are constructed by identifying the lateral acceleration and yaw moment created by a range of vehicle slip and steer angle combinations. The resulting lines of constant vehicle slip and constant steer are plotted as shown in figure 34. These diagrams are useful tools for identifying the limits of vehicle performance and understanding many aspects of vehicle behavior including stability and control.

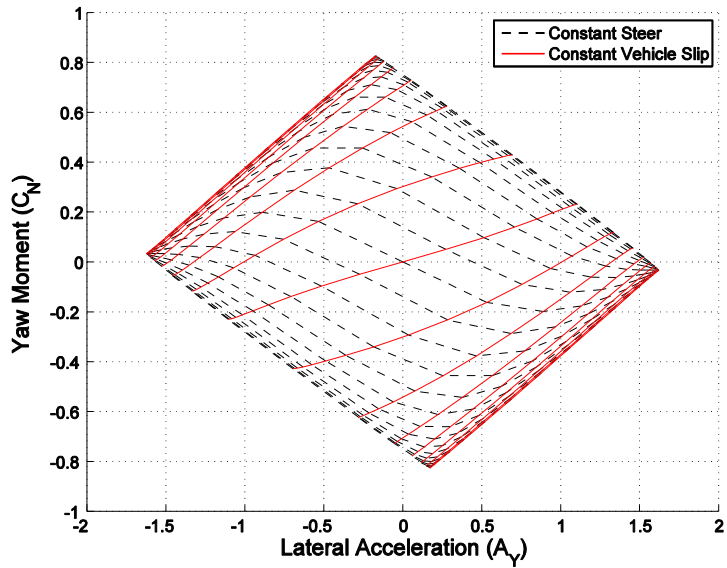


Figure 34: Milliken Moment Diagram –  $C_N$ - $A_Y$  – 30 m/s

The background and general framework for creating and using MMDs has been presented in various publications. However, several aspects of the method have not been adequately covered in the literature, which makes implementation difficult. The two most significant gaps in the creation and use of MMDs are the incorporation of longitudinal dynamics, and the implementation of various methods for incorporating yaw velocity. Presenting a process for creating MMDs that clarifies these two areas is the focus of this paper.

In the following background section, MMDs are introduced, including a brief review of the current literature. Next, processes will be demonstrated for creating MMDs beginning with a free-rolling vehicle. MMDs will then be created for driving and braking at constant longitudinal

acceleration. Finally, stability and steering sensitivity plots that are derived from MMDs are demonstrated as a tool for further understanding vehicle behavior.

### 3.2. Background

While MMDs can be created for arbitrarily complex vehicle models, they have their roots in linear force and moment vehicle analysis developed in [18]. This linear analysis was extended and MMDs were introduced in [19]. The use of MMDs was further developed in [20,21,22]. The background that follows will briefly cover the topics needed for a general understanding of linear force/moment analysis and moment diagrams. For a deeper review of both topics, [11] should be consulted.

#### 3.2.1. $C_N$ - $A_Y$ Diagrams

There are two types of MMDs presented in [11]. The first is constructed at a constant speed, and all lateral force created by the tires is used to hold the vehicle in steady state equilibrium without any outside disturbances. The yaw rate varies across the diagram with lateral acceleration and satisfies the steady state condition of (47). This type of diagram is referred to as a  $C_N$ - $A_Y$  diagram, as it is a plot of the yaw moment coefficient  $C_N$  vs. lateral acceleration  $A_Y$  as defined in (48, 49). Figure 34 is an example of a  $C_N$ - $A_Y$  diagram.

$$\omega = \frac{A_y}{V} \quad (47)$$

$$C_N = \frac{M_Z}{mgl} \quad (48)$$

$$A_Y = \frac{F_y}{mg} \quad (49)$$

The center of a  $C_N$ - $A_Y$  diagram, where lateral acceleration and yaw moment are both equal to zero, represents driving in a straight line. The upper part of the diagram represents positive yaw moments, which in an SAE coordinate system [23], indicates a moment turning a car into a right hand turn. Similarly, the right side of the diagram represents lateral acceleration in a right hand corner. Points along the  $A_y$  axis ( $C_N = 0$ ) represents pure steady state cornering, as all of the forces and moments are balanced. The area of the diagrams above and below the  $A_y$  axis can

be thought of as excess available moment that can be used to either stabilize or control the vehicle.

A useful attribute of this type of diagram is that it can be used to conceptualize constant velocity maneuvers on the lines of constant vehicle steer and vehicle slip. For example, figure 35 illustrates the sequence of a constant speed corner. The maneuver begins at point 1 with the vehicle driving in a straight line with no steer or vehicle slip angle. To enter the corner, a steering input is made, moving the vehicle up the line of constant vehicle slip to point 2. At point 2, excess yaw moment created by the steered front wheels causes a change in the vehicle slip angle and the vehicle follows the constant steer line to point 3. At point 3, the vehicle has reached steady state. To exit the corner, the steer angle is removed which moves the vehicle down the constant vehicle slip line to point 4. The unbalanced moment at point 4 causes the vehicle to follow the constant steer line back to point 1 at the center of the diagram, completing the cornering maneuver. While informative, it is important to note that this cornering representation is only an approximation because in a true cornering maneuver the steady state constraint from (47) will be violated during the transient corner entry and corner exit phases, and the behavior will depend significantly on how fast the steering input is applied.

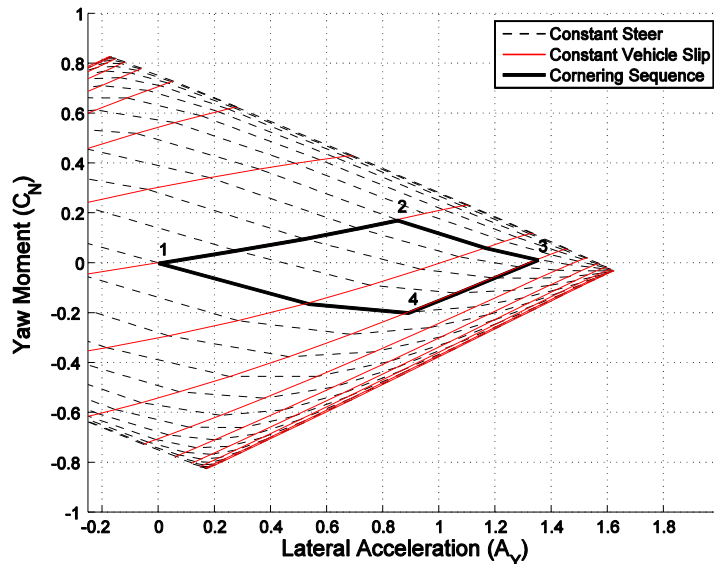


Figure 35:  $C_N$ - $A_y$  – 30 m/s – cornering sequence

In reality, when yaw acceleration is plotted against lateral acceleration, cornering maneuvers appear as smooth clockwise loops on the diagram. Right-handed corners create loops on the right side of the diagram (similar to the figure above), and left-handed corners create loops on the left side of the diagram. Slaloms result in loops that extend from the far right to the far left. Figure 36 illustrates this behavior with data from the 2011 Global Formula Racing Formula SAE vehicle. The data was collected while driving the “asymmetric oval” [24] test track, shown in figure 37, in a clockwise direction.

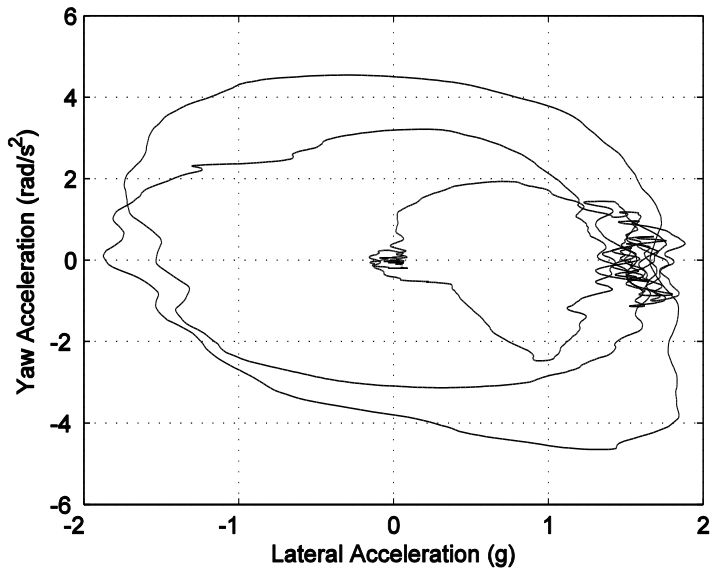


Figure 36: Lateral and yaw acceleration - on track testing

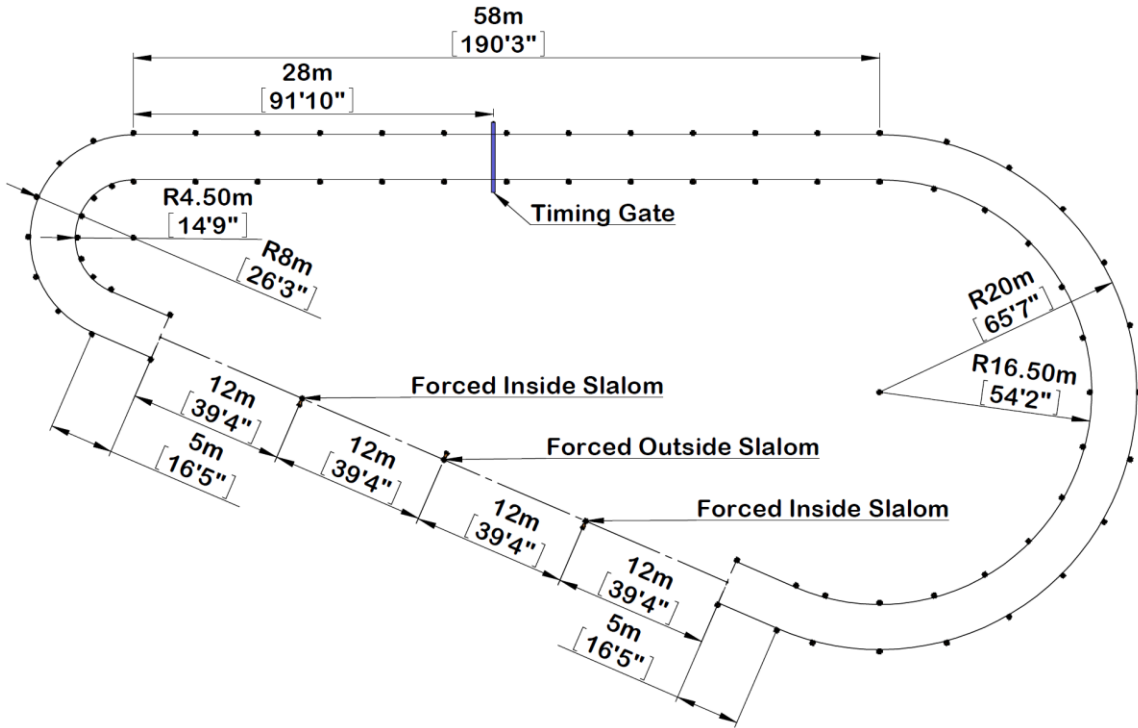


Figure 37: Asymmetric oval test track

Several linear vehicle characteristics are immediately apparent from the slopes of the constant steer and vehicle slip lines through the origin, as well as the outer shape of the diagram. For example, a MMD can be created at a speed such that the slope of the line of constant vehicle slip will be zero at the origin, meaning that for small increases in steering angle, there will be no change in vehicle slip angle. This is referred to as the tangent speed, as the vehicle is oriented tangent to its path. Above the tangent speed, the slope through the origin will be positive as shown in figure 35.

The line of constant steer angle that passes through the origin indicates the straight-line stability of the vehicle, and its slope is defined as the stability index. If the stability index is negative, any change in vehicle slip angle will be accompanied by a restoring moment that will return the vehicle to zero slip angle. In the opposite case, where the stability index becomes positive, positive vehicle slip angles will be accompanied by positive yaw moments, which will further increase the slip angle of the car. This will continue in an unstable manner and cause the car to spin unless a steering correction is made by the driver.

At the extreme edges of the diagram, cornering at or near the limit of the tires can be studied. The upper right edge represents saturation of the front tires. The lower right edge represents saturation of the rear tires (and the reverse on the left side). The maximum steady state lateral acceleration of the vehicle occurs where the outer edge of the diagram crosses the x-axis. If the upper right edge crosses the steady state axis, then the vehicle will be stable at the steady state limit and the vehicle will terminally “plow.” If the lower edge crosses the steady state axis then the vehicle will be unstable at the steady state limit and the vehicle will terminally “spin.”

Other interesting handling attributes related to the stability and controllability of the vehicle can be derived from  $C_N$ - $A_Y$  diagrams, such as trimmed sideslip, understeer gradient, and steering sensitivity. All of which are covered in [11].

### 3.2.2. $C_N$ - $C_Y$ Diagrams

The second type of diagram presented in [11] is the  $C_N$ - $C_Y$  diagram, which is a more general diagram and can take on multiple interpretations. The most significant difference between  $C_N$ - $C_Y$  diagrams and  $C_N$ - $A_Y$  diagrams discussed above is that the total lateral force generated is no longer assumed to resist the acceleration of the vehicle mass. Instead, some portion could be used to resist an outside disturbance, such as a side load due to wind or a component of gravitational force due to a cambered road. This distinction is made by replacing lateral acceleration  $A_Y$  with the lateral force coefficient  $C_Y$ . These diagrams are specified with a corner radius, which is used to determine the slip angles at the four corners of the vehicle. A  $C_N$ - $C_Y$  diagram created for an infinite radius is shown in 38.

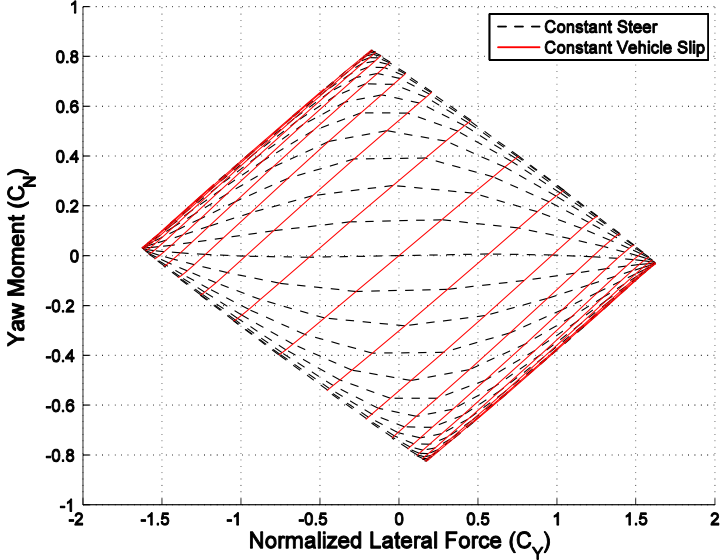


Figure 38:  $C_N$ - $C_Y$  – infinite radius

The standard interpretation of these diagrams is that they represent a constant radius test carried out over a range of speeds. With this interpretation in mind, the lateral force axis of the diagram, where yaw moment equals zero, represents steady state cornering on a constant radius. Neglecting any outside disturbances, the velocity can be identified using (50), the steady state constraint. If some lateral force disturbance is applied, more or less lateral force will be available to accelerate the vehicle and the speed of the vehicle on the radius will change.

$$V = \sqrt{A_y r} \quad (50)$$

An alternative interpretation of  $C_N$ - $C_Y$  diagrams is that they are created at constant speed and yaw rate. Geometrically, the slip angles created by a vehicle traveling at a speed  $V$  with yaw rate  $\omega$  will be identical to those traveling on a radius  $r = V/\omega$ , although the path radius is  $r = V^2/A_y$ . If other effects of speed are neglected, such as aerodynamic forces, the diagrams are equivalent. These two interpretations are not mutually exclusive, they simply offer different perspectives for looking at the same data. If aerodynamic forces or other secondary speed effects are included, the two  $C_N$ - $C_Y$  interpretations will no longer lead to the same results.

Regardless of which interpretation is used, large portions of the  $C_N-C_Y$  diagram will be of little value under normal circumstances. If the constant radius interpretation is applied, then negative accelerations on a positive radius corner lead to imaginary speeds, which do not have any physical meaning. Only when subjected to large disturbances will the entire diagram represent physically realizable states. If the constant speed and yaw-rate interpretation is used, when yaw rate and speed are both positive, negative accelerations represent a vehicle on a left handed path radius that is rotating to the right. While physically possible, this does not represent usual vehicle behavior and is not likely to be of much use. While much of the diagram will be uninteresting, because the usual steady state constraints no longer apply,  $C_N-C_Y$  can be used to represent more complicated transient dynamics.

While the interpretation of  $C_N-C_Y$  diagrams is less intuitive than  $C_N-A_Y$  diagrams they are simple and efficient to create. They have the added advantage that they are a direct graphical representation of the lateral acceleration and yaw acceleration derivative terms ( $N_\delta, N_\beta, Y_\delta, Y_\beta$ ) from [18], and how they vary over the performance range of the vehicle.

### 3.2.3. Applications

In [22], a specific implementation of MMDs is used along with acquired data and driver feedback, to make development changes to a Formula 1 car. The authors show that this type of model representation is useful for understanding and tuning a vehicle. Additional measures of stability and controllability are established in [25] based on how close a dynamic maneuver comes to the limits of a MMD. The use of MMDs for stability and control measurements is expanded further in [26], which uses CARSIM, a fully transient vehicle simulation package, to generate Milliken Moment Diagrams for use in stability studies. The analysis provides interesting insight into vehicle performance and quantifiable measurements of limit stability and controllability. The above examples all use  $C_N-A_Y$  diagrams. No examples of practical application of  $C_N-C_Y$  diagrams could be identified in the literature.

### 3.3. Creating Acceleration Moment Diagrams

The following sections cover the creation of Acceleration Moment Diagrams.

#### 3.3.1. Reference Frames

Three reference frames will be referred to throughout this paper. In every case, the reference frames are right handed with x-forward and z-down with respect to the vehicle. The reference frames are all treated as inertial frames that are instantaneously aligned with their respective references. The first reference frame is located at the vehicle center of mass and oriented along the body of the vehicle. This frame will be referred to as the “body frame” and denoted with a superscript “ $b$ ”. The second frame is also located at the vehicle center of mass, but its x-axis is oriented along the direction of travel of the vehicle. It will be referred to as the “velocity frame” and is denoted with a superscript “ $v$ ”. The velocity frame is related to the body frame by a rotation about their common z-axis with a magnitude of the vehicle slip angle  $\beta$ . Transforms from the body frame to the vehicle frame are given in (51, 52). A “tire frame” will be referred to which is located at the tire contact patch and oriented along the center plane of given tire. The tire frame for a particular tire is rotated relative to the body frame by a steering angle  $\delta$ . Quantities represented in the tire frame will be denoted with a superscript “ $t$ ”. Parameters specific to an individual tire will be denoted with a subscript “ $i$ ”. All MMDs in this paper are created with respect to the velocity frame, which requires a rotation of the accelerations calculated in the body frame to the velocity frame.

$$x^v = x^b \cos \beta + y^b \sin \beta \quad (51)$$

$$y^v = y^b \cos \beta - x^b \sin \beta \quad (52)$$

#### 3.3.2. Tire Slip Angles

Slip angles for a given tire can be broken down into two parts;  $\beta_i$  the component due to the vehicle’s geometry, yaw rate and speed; and  $\delta_i$ , the slip angle caused due to steering (including toe angle). Individual wheel slip angles  $\beta_i$  are found using (53), or equivalently using (54). The x and y positions of the four tire contact patch centers in the body frame are denoted by  $X_i$  and  $Y_i$

respectively. Total tire slip angle, including steered angle, is shown in (55). In the case where yaw rate is zero, tire slip angle is only determined by body slip angle and steered angle and the tire slip angles simplify to (54).

$$\beta_i = \tan^{-1} \frac{V \sin \beta + \omega X_i}{V \cos \beta - \omega Y_i} \quad (53)$$

$$\beta_i = \tan^{-1} \frac{r \sin \hat{\alpha} + X_i}{r \cos \beta - Y_i} \quad (54)$$

$$\alpha_i = \beta_i - \delta_i \quad (55)$$

$$\alpha_i = \beta - \delta_i \quad (56)$$

### 3.3.3. Vehicle-Slip and Steer Angles

To create an MMD, a grid of vehicle-slip and steer angles is needed that covers the range of interest. The simplest and most intuitive way to generate a grid is to vary the vehicle-slip angle across one dimension, and steer angle across the other. This method is simple, but because the front slip angles are affected by both the steered angle and the vehicle-slip angle, the resulting grid is not evenly distributed across the desired range of slip angles, and a larger grid is needed to cover the desired range. While this is not a computationally efficient grid of points, it is simple and conceptually matches the structure of MMDs (grid of constant steer and vehicle-slip) and is therefore recommended for initial implementation of MMDs.

If many diagrams are to be made quickly, a more efficient grid can be defined along front and rear construction-lines [11] that closely represent the slip angle at each end of the vehicle when not considering yaw rate. Along the rear construction-line, the vehicle-slip angle is varied and a corresponding counter steer of equal magnitude is introduced at the front. Along this construction line, the force and moment behavior is dominated by the rear of the vehicle. Along the front construction line, only the steering angle of the front is varied and the vehicle's behavior is dominated by the front of the vehicle. Figures 39 and 40 show representations of the vehicle-slip and steer angles for the two grid methods, and the resulting slip angles created when yaw rate is neglected. When the construction line method is used, the resulting MMDs

generated will still be plotted as lines of constant vehicle-slip and steer. The only difference between these two methods is the range of vehicle-slip and steer that is covered.

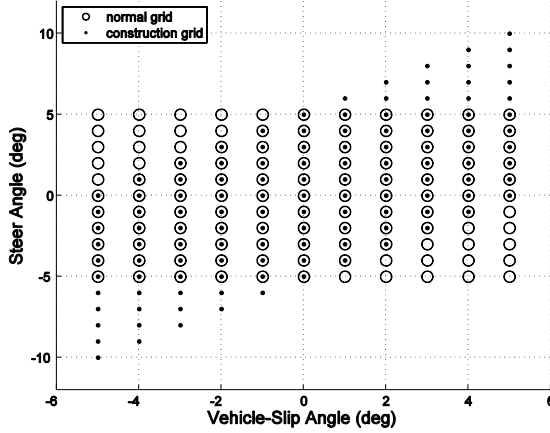


Figure 39: Steer vs. vehicle-slip: normal and construction grids

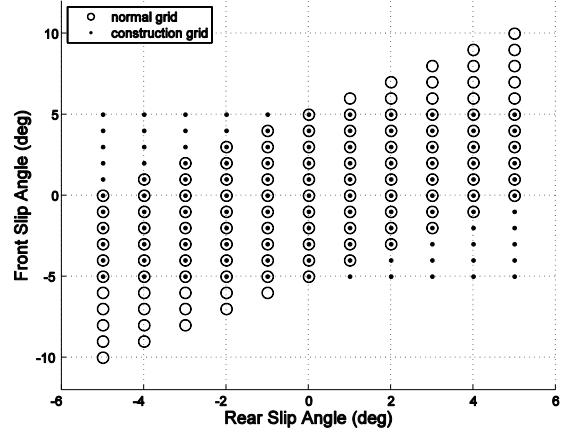


Figure 40: Front vs. rear slip angle: normal and construction grids

If the vehicle and MMD method are both symmetric, further efficiency can be gained by calculating only half of the diagram. This is done by varying either the vehicle slip angle or the vehicle steer angle over only half the usual range. When plotting the diagram, the opposite side can be represented by reversing the sign of both lateral acceleration and yaw moment.

If the diagram to be created is not symmetric, the entire range must be calculated, but when creating  $C_N$ - $C_Y$  diagrams, the center can be shifted to allow a smaller range of vehicle slip and steer angles to cover the entire performance range. In this case, (53) or (54) is used to calculate the slip angles at the centerline of the front and rear axles without considering any additional vehicle slip angle or steer angle. The vehicle-slip and steer range is offset such that the resulting front and rear slip angle ranges are centered on zero. Figures 41 and 42 show un-shifted and shifted grids for a constant yaw rate MMD created at 15 m/s and 1.5 rad/sec (10 meter radius). Although not necessary, the shift magnitude can be rounded to the nearest grid spacing in order to improve the aesthetics of labeled plots.

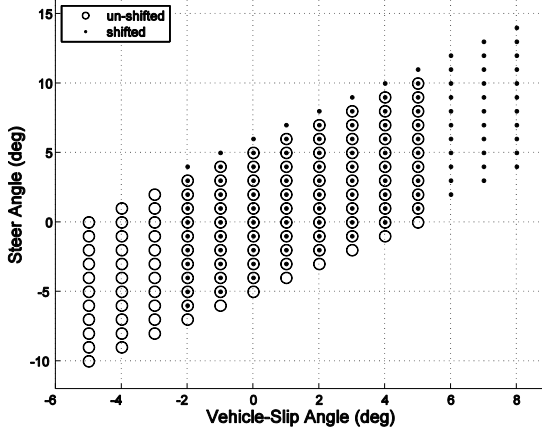


Figure 41: Steer vs. vehicle-slip: un-shifted and shifted grids

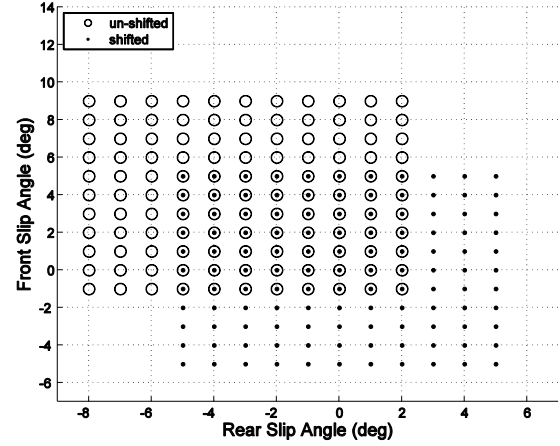


Figure 42: Front vs. rear slip angle: un-shifted and shifted grids

When creating  $C_N$ - $A_Y$  diagrams or  $C_N$ - $C_Y$  diagrams, either yaw rate or velocity varies across the diagram and the range of slip angles and steers required will depend significantly on either the specified speed of the  $C_N$ - $A_Y$  diagram, or the specified radius of the  $C_N$ - $C_Y$  diagram. In either case, some prior knowledge or some trial and error may be needed to determine the appropriate vehicle slip and steer ranges. All diagrams in this paper are created using a  $\pm 10^\circ$  grid with  $0.5^\circ$  increments. The construction line method is used and the grids will be shifted to center the slip angle range on zero when appropriate.

### 3.3.4. Vehicle Model Definition

The vehicle model used is as simple as possible while still maintaining the interesting factors that make creating MMDs a challenge. Additional complexity can be added to the model in order to gain more insight without significantly changing the procedures presented. The vehicle model has four wheels and dynamically simulates lateral, longitudinal and yaw degrees of freedom of the vehicle (3-DOF model). Parallel steering is used and the vehicle is left-right symmetric. Effects of aerodynamic forces and moments are not included.

A “Magic Formula” based tire model is used to predict longitudinal and lateral forces at each corner of the vehicle. The model represents the coupling between longitudinal and lateral forces, which is important when significant driving or braking performance is represented. A full description of the tire model used can be found in chapter 2 (tire model paper).

Equations (57-59) show how the steer angles  $\delta_i$  are used to rotate the longitudinal and lateral tire forces  $F_{xi}^t$  and  $F_{yi}^t$  into the body frame where they are summed to calculate the total forces and moments.

$$F_x^b = \sum_{i=1}^4 (F_{xi}^t \cos \delta_i - F_{yi}^t \sin \delta_i) \quad (57)$$

$$F_y^b = \sum_{i=1}^4 (F_{xi}^t \sin \delta_i + F_{yi}^t \cos \delta_i) \quad (58)$$

$$M_z = \sum_{i=1}^4 (X_i F_{xi}^t \sin \delta_i - Y_i F_{xi}^t \cos \delta_i + Y_i F_{yi}^t \sin \delta_i + X_i F_{yi}^t \cos \delta_i) \quad (59)$$

In order to calculate the vertical load on the four wheels, auxiliary equations are used to represent the suspension stiffness. Static front and rear weights are calculated in (60, 61), where  $w$  is the weight ( $mg$ ) of the vehicle and  $B_{rw}$  is the fraction of the total static load on the rear axle.

$$F_{zsf} = \frac{w(1 - B_{rw})}{2} \quad (60)$$

$$F_{zsr} = \frac{wB_{rw}}{2} \quad (61)$$

Equations (62-64) are used to calculate the force gains due to lateral and longitudinal accelerations on each axle.  $CG_z$  is the z height of the center of gravity above the ground,  $l$  is the wheel base of the vehicle,  $t$  is the track width of the car at the noted end and  $B_{rs}$  is the fraction of roll stiffness at the rear axle. In the case of longitudinal acceleration, front and rear weight transfers are equal in magnitude and opposite in sign.

$$\frac{\Delta F_{zf}}{\Delta A_x^b} = \frac{CG_z m}{2l} \quad (62)$$

$$\frac{\Delta F_{zf}}{\Delta A_y^b} = \frac{CG_z w(1 - B_{rs})}{t_{front}} \quad (63)$$

$$\frac{\Delta F_{zr}}{\Delta A_y^b} = \frac{CG_z w B_{rs}}{t_{rear}} \quad (64)$$

The static wheel loads and the gains due to accelerations are used in (65-68) to calculate the vertical loads on the four wheels. These equations must be modified if the load transferred from a tire is greater than its static load (limiting a tire to push on the road surface, not pull). In this paper, all load transfers are smaller than the static loads so this condition is not considered. While the MMDs represent accelerations in the velocity frame, the load equations use body accelerations.

$$F_{zfl} = F_{zsf} + \frac{\Delta F_{zf}}{\Delta A_x^b} A_x^b + \frac{\Delta F_{zf}}{\Delta A_y^b} A_y^b \quad (65)$$

$$F_{zfr} = F_{zsf} + \frac{\Delta F_{zf}}{\Delta A_x^b} A_x^b - \frac{\Delta F_{zf}}{\Delta A_y^b} A_y^b \quad (66)$$

$$F_{zrl} = F_{zsr} - \frac{\Delta F_{zf}}{\Delta A_x^b} A_x^b + \frac{\Delta F_{zr}}{\Delta A_y^b} A_y^b \quad (67)$$

$$F_{zrr} = F_{zsr} - \frac{\Delta F_{zf}}{\Delta A_x^b} A_x^b - \frac{\Delta F_{zr}}{\Delta A_y^b} A_y^b \quad (68)$$

### 3.3.5. Free Rolling $C_N$ - $C_Y$ Diagram (Infinite Radius)

The first and simplest diagram to create is a free rolling  $C_N$ - $C_Y$  diagram with zero yaw rate (infinite radius). In this case, no driving or braking forces will be applied and tire slip angles depend only on the vehicle slip angle and steer angle. Neglecting aerodynamics effects, this diagram will be insensitive to speed.

### **3.3.5.1. Slip Ratios**

A free rolling MMD will be created by setting the slip ratio of each tire to zero, resulting in zero longitudinal force at each tire in its own reference frame, neglecting rolling resistance. If a model that accurately represents rolling resistance is available, this effect can be included. When rolling resistance is neglected as it is here, the overall vehicle longitudinal acceleration in the direction of travel will be exactly zero when both slip and steer are zero. With yaw rate equal to zero (infinite radius), every other point on the diagram will have some amount of negative longitudinal acceleration due to slip angle induced drag from lateral forces.

### **3.3.5.2. Tire Vertical Forces**

In addition to slip angles and slip ratios, vertical forces acting on each tire must be known to calculate lateral tire forces. Determining the vertical forces is an implicit problem because the vertical forces acting on each tire depend on the weight transfers from lateral and longitudinal accelerations, each of which depend on the tire forces to be calculated. To determine the appropriate vertical tire forces, an initial guess is made. A simple first guess is to use the static vertical forces. This allows the calculation of lateral tire forces, and resulting vehicle accelerations. These accelerations are used to update the initial vertical force estimates. Using these updated vertical force estimates, tire forces and vehicle accelerations are recalculated. Each time this process is repeated, the difference between the acceleration used to calculate the vertical loads and the resulting accelerations decreases. Tolerances are chosen for lateral and longitudinal acceleration as well as yaw moment and the process is repeated until the difference between two steps is less than the chosen tolerance. Once the value settles within the target error, the solutions have converged. Figure 21 displays a flow chart of the process.

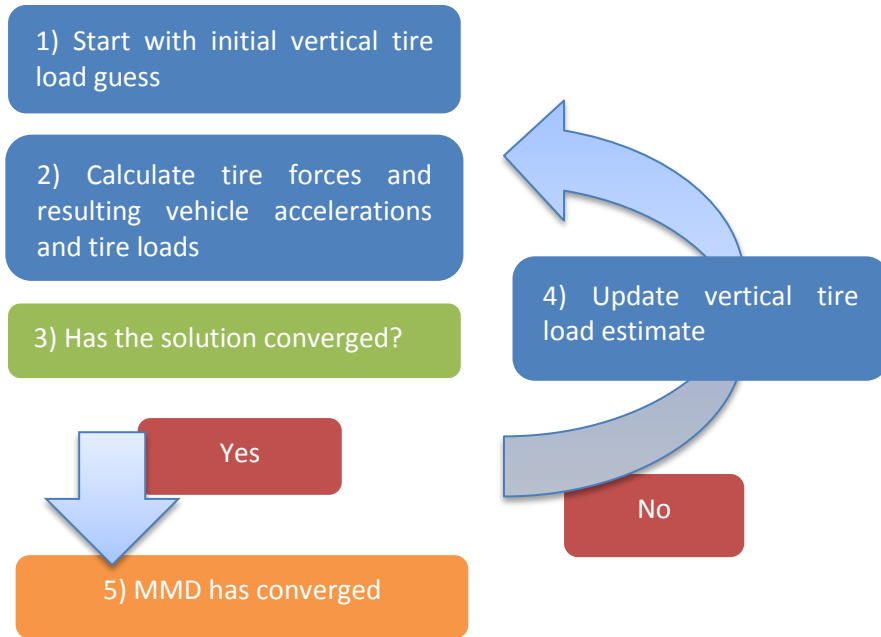
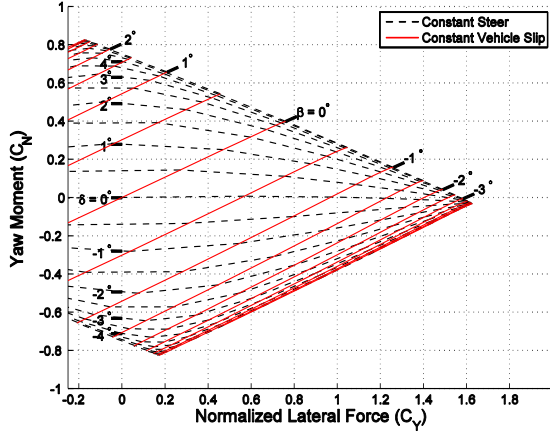
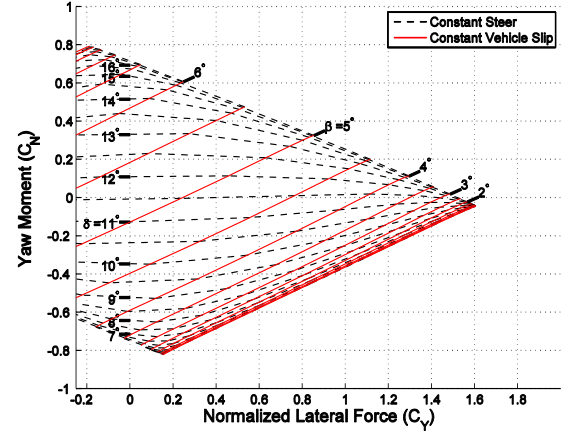


Figure 43: Flow chart for load transfer convergence

### 3.3.6. Constant Yaw Rate $C_N$ - $C_Y$ Diagram (Finite Radius)

The simplest way to incorporate yaw rate into MMDs is to create diagrams of constant yaw rate at a given speed (or radius). The free rolling  $C_N$ - $C_Y$  diagram discussed above belongs to this family of diagrams as it represents a constant yaw rate of zero. The only difference when creating these diagrams is that the slip angles are now dependent on vehicle speed and yaw rate (or radius) and the range of vehicle slip and steer angles required to cover the entire sub limit region will change. Constant yaw rate diagrams created with non-zero yaw rate and finite speed will not be symmetric for a symmetric vehicle. Figure 44 is an infinite radius  $C_N$ - $C_Y$  diagram and figure 45 represents a 10 meter radius. The two diagrams have very similar appearance, and the most significant difference is the range of vehicle slip angles and steer angles across the diagram. There are also subtle differences in the diagram shape and overall size that are most noticeable at the corners of the diagram.

Figure 44:  $C_N$ - $C_Y$  – infinite radius – detailedFigure 45:  $C_N$ - $C_Y$  – 10 meter radius – detailed

### 3.3.7. Free Rolling $C_N$ - $A_Y$ Diagram

Creating  $C_N$ - $A_Y$  diagrams is similar to creating  $C_N$ - $C_Y$  diagrams. The most significant difference is how yaw rate is handled. Unlike  $C_N$ - $C_Y$  diagrams, yaw rate (or corner radius) is not known for each point on the grid before the diagram is created, and due to its dependence on lateral acceleration, must be identified by convergence in the same way as tire vertical loads. The steady state constraint shown in (69) is used to estimate a new yaw rate before each iteration step, with an initial guess of zero.

$$\omega_{est} = \frac{A_Y^v}{V} \quad (69)$$

Unlike estimating the vertical loads, estimating the yaw rate in this way can cause the solution to oscillate and converge slowly. In some cases, the solution can oscillate without converging or even become unstable. In order to speed convergence, the solution can be “relaxed” using the relaxation parameter  $p_r$  shown in (70). The relaxation parameter is a weighting between the previous yaw rate estimate  $\omega_n$ , and the new estimate  $\omega_{est}$  which produces a more stable predicted yaw rate estimate  $\omega_{n+1}$  that is used to calculate the slip angles for the subsequent iteration. At high speeds, the yaw rate will be small and have a relatively small effect on the solutions. Due to this, diagrams at high speeds tend to be relatively stable and relaxation values between 0.7 and 0.8 generally lead to fast convergence. At speeds below tangent speed,

relaxation values of 0.5 or lower may improve results. To further improve speed of convergence, results from higher speeds can be used as an initial guess for vertical tire forces and yaw moments.

$$\omega_{n+1} = \omega_{est}(1 - p_r) + \omega_n p_r \quad (70)$$

Figures 46 and 47 show  $C_N$ - $A_Y$  diagrams created at 30, and 20 m/s (108, and 72 kph). Several linear performance characteristics can be identified from these figures. First, the slope of the constant vehicle slip curve is positive in figure 46 and negative in figure 47 indicating that the tangent speed is between 20 and 30 m/s for this vehicle. Also, the relative slopes of the constant vehicle steer lines differs significantly between the two diagrams demonstrating the decrease in yaw damping at higher speeds.

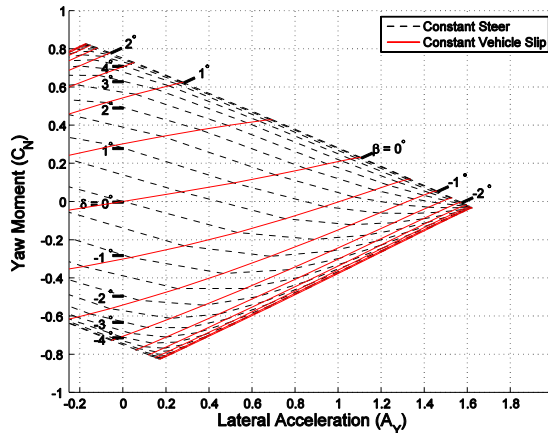


Figure 46:  $C_N$ - $A_Y$  – 30 m/s – detailed

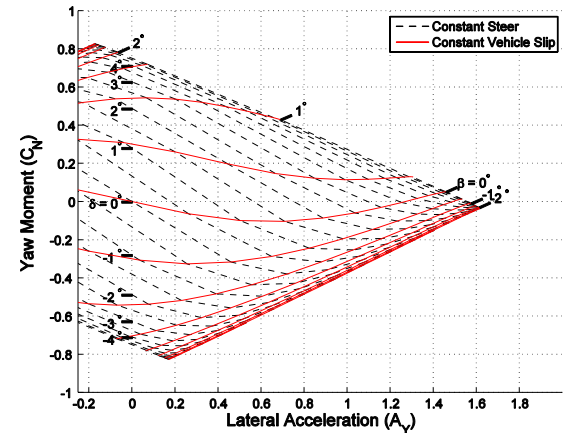


Figure 47:  $C_N$ - $A_Y$  – 20 m/s – detailed

### 3.3.8. Level Surface Moment Diagrams

Every point on a free rolling  $C_N$ - $A_Y$  diagram, other than the center, will have some amount of negative longitudinal acceleration caused by induced slip angle drag, so maneuvers on the diagram will not occur at constant speed. This is not immediately apparent from typical MMDs but can be seen if the same surface is viewed from other perspectives, with longitudinal acceleration as the third dimension (normally oriented out of the page.) For example, figure 48 is a view of a free rolling  $C_n$ - $A_y$  diagram from the “side” which shows lateral and longitudinal

acceleration and figure 49 shows a three dimensional projection of the surface. In previous plots, points past saturation had been removed from the diagrams to show the details around the edges. In these figures, points past saturation have not been removed to demonstrate the full shape. The edges of the diagram would continue further if the range were not limited to  $\pm 10$  degrees.

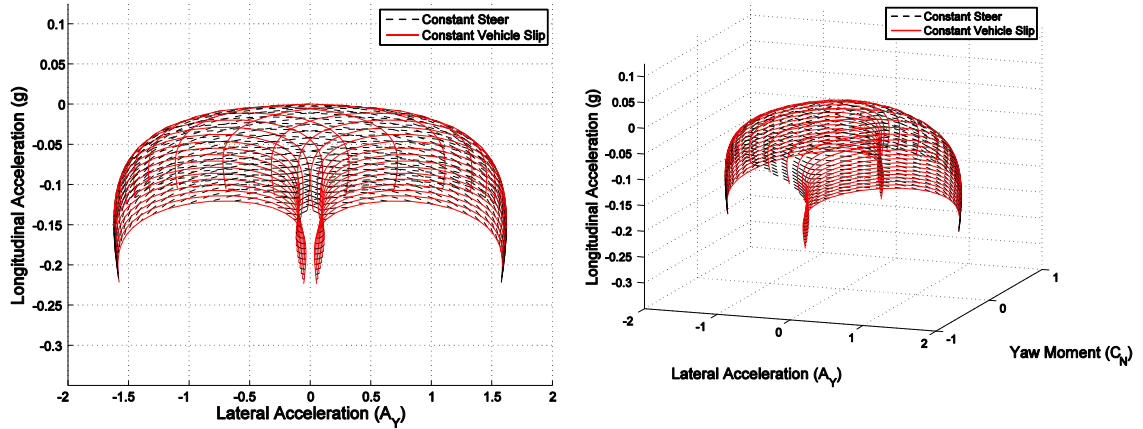


Figure 48:  $C_N-A_Y$  – 30 m/s – side view

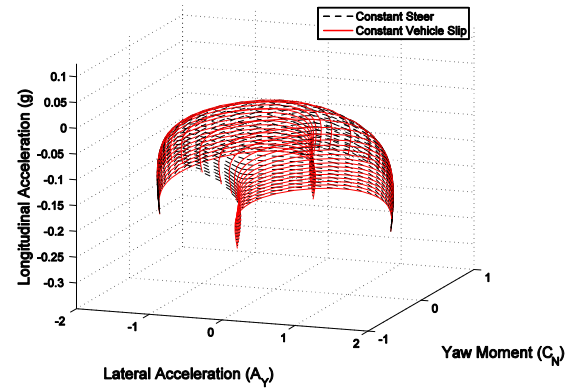


Figure 49:  $C_N-A_Y$  – 30 m/s – 3d view

In order to understand vehicle behavior over the entire driving and braking range, both  $C_N-C_Y$  and  $C_N-A_Y$  diagrams can be constructed over a range of longitudinal accelerations. To do this, diagrams are constructed with every grid point at the same longitudinal acceleration. These MMDs of constant longitudinal acceleration are referred to as level surfaces as they all share the same level of longitudinal acceleration. A  $C_N-A_Y$  level surface for zero longitudinal acceleration is the simplest to understand, because maneuvers performed at a constant velocity can be represented, but similar surfaces can be created for any longitudinal acceleration within the capabilities of the tires. Figure 50 shows level surfaces at -1.0, -0.5, 0.0, 0.5, and 1.0 g. The diagrams at more extreme longitudinal accelerations have smaller lateral and yaw moment limits due to the interaction between lateral and longitudinal tire forces. Points that could not reach the desired level due to tire saturation are not shown.

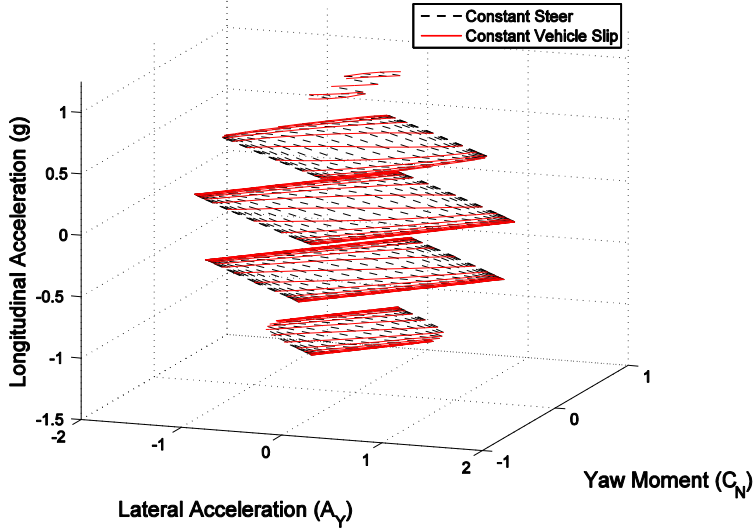


Figure 50:  $C_N$ - $A_Y$  – 30 m/s – multiple level surfaces

### 3.3.8.1. Driving and Braking Constraints

When creating level surfaces it is important to represent the mechanical or hydraulic system that is used to generate the longitudinal forces. In the driving case, an open differential is approximated by requiring the tire frame longitudinal forces for the two rear tires to equal to one another as shown in (71). In the braking case, front and rear hydraulic braking circuits are approximated by requiring that both front tires have the same longitudinal force in their respective tire frames, and that both rear tires have the same longitudinal forces in theirs. The front and rear longitudinal tire forces are linked by a front brake bias term  $B_{FBB}$ . A value of 1 represents equal longitudinal force front and rear, and a value of 2 results in twice the force being generated at the front compared to the rear. The brake force constraint is shown in (72).

$$F_{Xrl} = F_{Xrr} \quad (71)$$

$$F_{Xfl} = F_{Xfr} = B_{FBB}F_{Xrl} = B_{FBB}F_{Xrr} \quad (72)$$

These constraints are the simplest representations of driving and braking systems that can be implemented. Other constraints can be implemented to represent anti-lock brakes, torque-biasing differentials, or all-wheel drive. For example, a simple all-wheel drive implementation

would be to use the braking constraint (72) under driving conditions. This would approximate the behavior of front and rear open differentials and a constant bias between front and rear drive. Active systems that use other vehicle parameters to determine the target forces for each wheel in driving and braking cases could also be implemented. Somewhat ironically, enforcing the equal speed constraint of a locked differential would be significantly more complicated than the representation of an open differential.

### 3.3.8.2. Force Targets

As in the case of the free-rolling MMDs, creating level surfaces is an iterative process, but in addition to identifying the appropriate vertical tire forces and lateral accelerations, appropriate longitudinal forces must be identified that produced the desired longitudinal acceleration as well as satisfy the constraints of a differential or hydraulic braking system.

To create a level surface, a free rolling surface or other initializing surface is used as a starting point. The difference between the target longitudinal acceleration and the initial surface is used to calculate the change in longitudinal force required to reach the target accelerations as shown in (73). This desired change in longitudinal force is split between the two rear wheels when driving, or all four wheels when braking. The target force for a single rear wheel is determined using the current longitudinal forces and the differential or braking constraints. Equation (74) shows how the target force is calculated for the driving case and (75) shows the target for the rear tire in the braking case. The rear target force and the hydraulic braking system constraint are used to calculate the front force target. These forces are only an estimate of the forces that will be required to reach the desired longitudinal acceleration, and they are somewhat simplified as they do not consider the angle of the wheels relative to the direction of travel, as well the effect of lateral tire forces on longitudinal acceleration. While these factors could be included, they add complexity and do not significantly decrease the time required for convergence.

$$\Delta F_{Xerror}^V = M(A_{Xtarget}^V - A_{Xcurrent}^V) \quad (73)$$

$$F_{Xr}^T = \frac{F_{Xrl}^T + F_{Xrr}^T + \Delta F_{Xerror}^V}{2} \quad (74)$$

$$F_{Xr}^T = \frac{F_{Xfl}^T + F_{Xfr}^T + F_{Xrl}^T + F_{Xrr}^T + \Delta F_{Xerror}^V}{2(1 + B_{fbb})} \quad (75)$$

### 3.3.8.3. Slip Ratios

With the target longitudinal forces determined, the slip ratios required to create the target forces must be identified. The ideal solution would be an inverse tire model, with longitudinal force as an input, which could be solved explicitly. Unfortunately, there is not a direct way of doing this for Magic Formula models that include lateral/longitudinal interactions like the one used in this study. Instead, a Taylor series can be used to approximate the tire model in the region of interest. A second order series, shown in (76) is used.  $\Delta F_x$  is the desired change in longitudinal force for an individual tire and is defined in (77). The first and second order derivative terms can be calculated numerically, or by direct differentiation of the tire model with respect to slip ratio. Figure 51 shows an example tire model curve, its corresponding second order Taylor polynomial, as well as the maximum longitudinal force that is identified through multiple peak identification iterations.

$$0 = \frac{\partial^2 F}{\partial \sigma^2} \Delta \sigma^2 + \frac{\partial F}{\partial \sigma} \Delta \sigma - \Delta F_x \quad (76)$$

$$\Delta F_{xi} = F_{xi-target} - F_{xi} \quad (77)$$

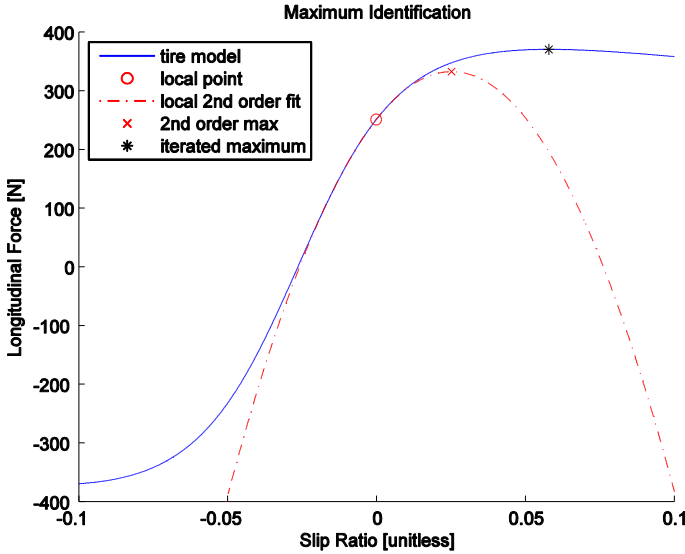


Figure 51: Quadratic Taylor approximation of tire force

The slip ratio for a desired longitudinal force is calculated using the quadratic equation shown in (78). As long as the desired longitudinal force is less than the maximum estimated by the Taylor series there will be two real solutions and the solution with the smaller magnitude will be selected. In either the driving or braking case, if a tire is unable to meet the force target, the slip ratio for peak longitudinal force is used. When one tire has reached its limit, the other tires' target forces are adjusted to respect the differential or hydraulic braking constraints based on the limiting tire. For example, in the driving case, if the desired longitudinal force is greater than the maximum force estimated by the Taylor series for either rear wheel, then the target force of both rear wheels is reduced to the smaller of the two maximum force estimates. In these cases, where at least one tire is unable to reach the required longitudinal force, the vehicle will not reach the target longitudinal acceleration and will converge to the maximum longitudinal acceleration for the particular vehicle slip and steer combination. In some cases, longitudinal forces do not peak, or peak at very high slip ratios. In these cases, it is practical to place an upper limit on slip ratio (e.g., 0.5).

$$\Delta\sigma = \frac{-\frac{\partial F_x}{\partial\sigma} \pm \sqrt{\left(\frac{\partial F_x}{\partial\sigma}\right)^2 + 4\frac{\partial^2 F_x}{\partial\sigma^2}\Delta F_x}}{2\frac{\partial^2 F_x}{\partial\sigma^2}} \quad (78)$$

Once slip ratio estimates are calculated, they are used to recalculate the tire forces, vehicle accelerations and resulting vertical loads. Based on the new accelerations, target longitudinal forces and slip ratio estimates are computed and the process is repeated until constraint equations and vehicle accelerations have converged to their specified targets.

The identification of target longitudinal forces and their associated slip ratios can be carried out simultaneously with the identification of vertical tire loads, and in the case of  $C_N$ - $A_Y$ , along with the yaw rate. Figure 52 is a flow chart for the level-surface convergence process.

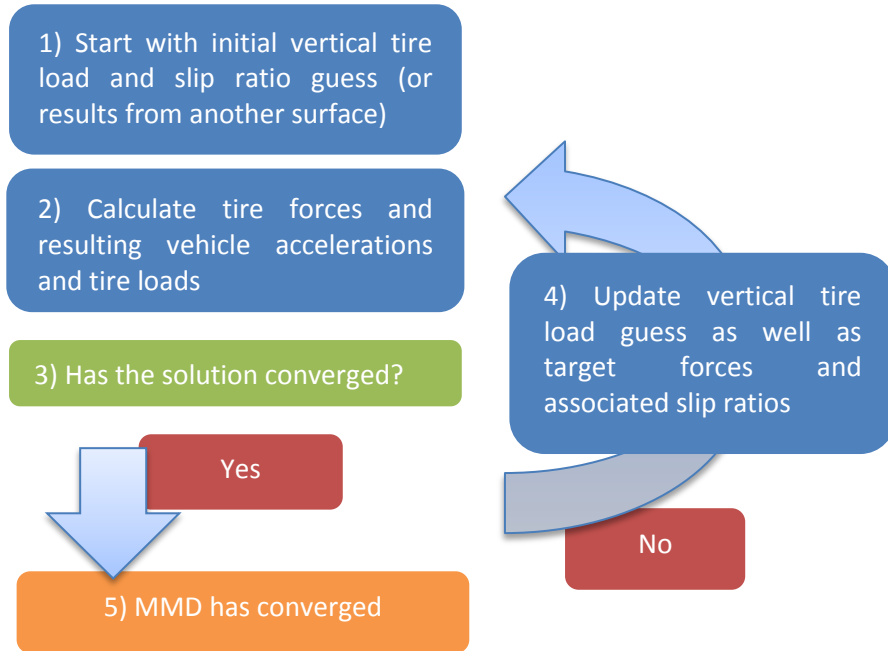
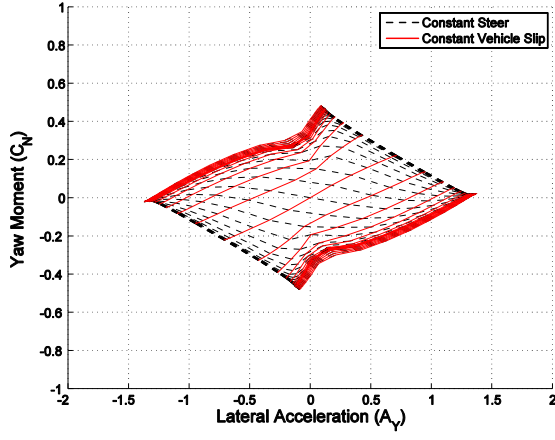
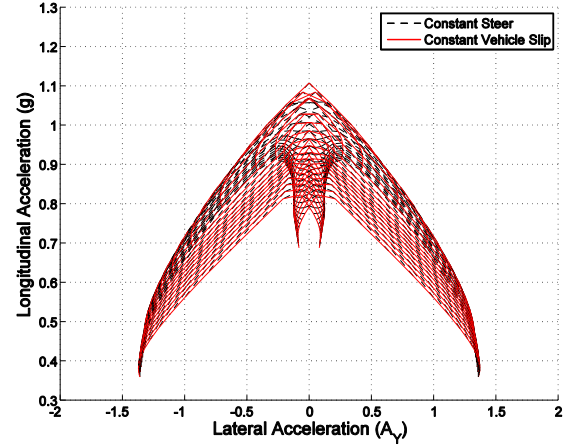
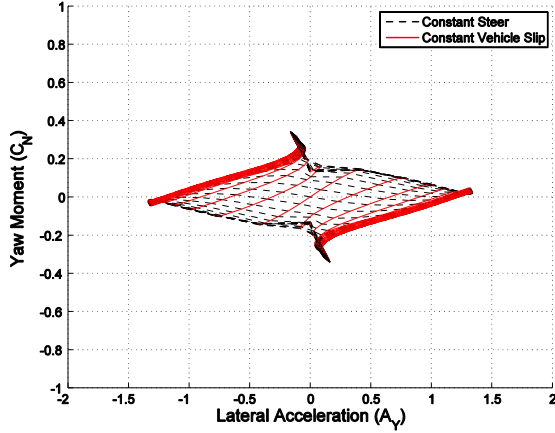
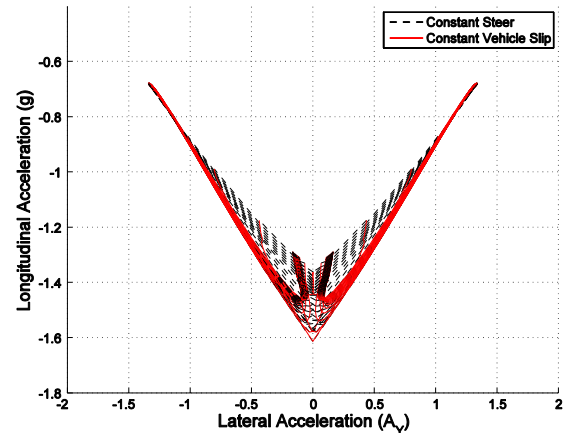


Figure 52: Flow chart for level surface convergence

If the target longitudinal acceleration is greater than the vehicle can achieve, the diagram will converge to the maximum longitudinal acceleration for every point, creating a limit longitudinal acceleration surface. Figures 53 through 56 show limit longitudinal surfaces for driving and braking.

Figure 53:  $C_N$ - $A_Y$  – 30 m/s – driving limitFigure 54:  $C_N$ - $A_Y$  – 30 m/s – driving limit – g-g viewFigure 55:  $C_N$ - $A_Y$  – 30 m/s – braking limitFigure 56:  $C_N$ - $A_Y$  – 30 m/s – braking limit – g-g view

### 3.4. Interpretation

There are key parts of MMDs that are useful indicators of vehicle performance, such as the slopes of the constant vehicle slip and vehicle steer lines. When looking at a single diagram, these are immediately observable, but once diagrams are made across a large range of velocities, yaw rates, and longitudinal accelerations it quickly becomes a cumbersome task to look at every diagram. To better use the information in MMDs, diagrams can be derived that

condense the information into a more accessible form. The following are several examples of the types of plots that can be created when combining information from a number of MMDs.

Related measures of stability and controllability are the stability index and steering sensitivity [11]. Figures 57 and 58 show the stability index plotted vs. lateral acceleration for driving and braking at several levels of longitudinal acceleration. At zero longitudinal acceleration, the stability index is negative, representing stability across the entire lateral acceleration range and stability increases at the limit of lateral acceleration. The braking case is interesting because the limit stability switches between stable at 0g to unstable at 0.5g and back to stable at 1.0g. Figures 59 and 60 show steering sensitivity plotted vs. lateral acceleration, and indicate how the vehicle will react to steering changes made by the driver. At the same points that the stability index crosses zero, the steering sensitivity goes to infinity further indicating the instability at those points.

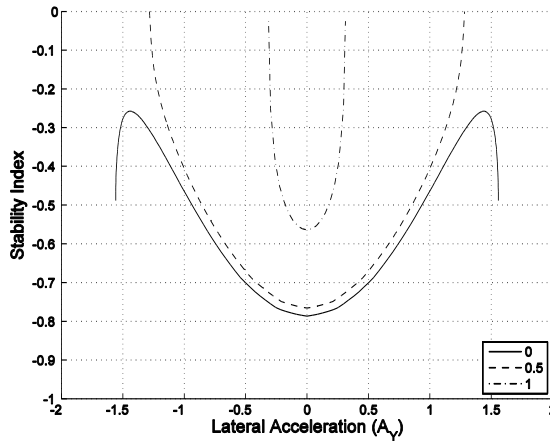


Figure 57: Stability index – 20 m/s – driving

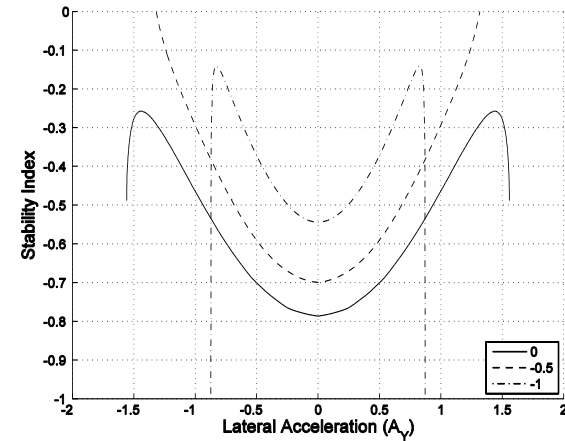


Figure 58: Stability index – 20 m/s – braking

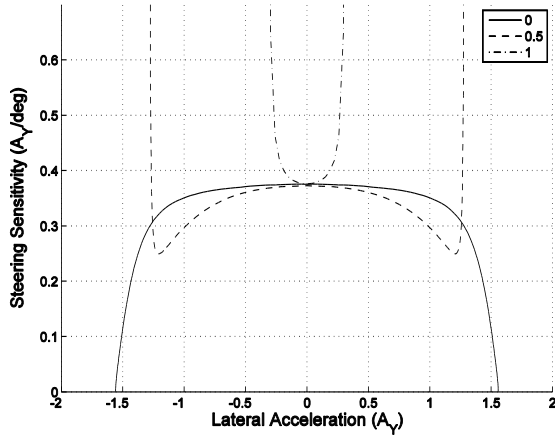


Figure 59: Steering sensitivity – 20 m/s – driving

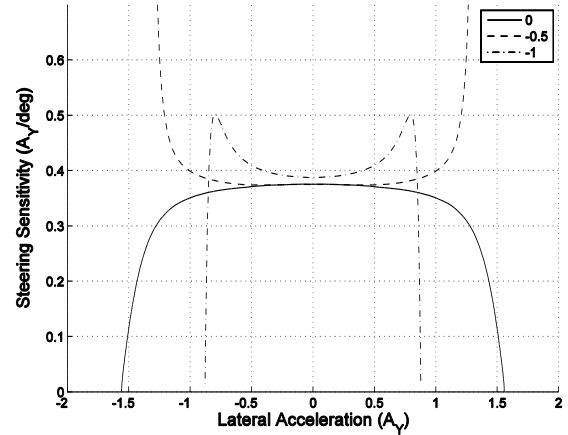


Figure 60: Steering sensitivity – 20 m/s – braking

One of the most common representations of vehicle performance is the g-g diagram, which is a plot of longitudinal acceleration vs. lateral acceleration. Figure 61 shows a g-g diagram that was created from  $C_N$ - $A_Y$  level surface diagrams that cover the entire longitudinal capabilities of the vehicle.

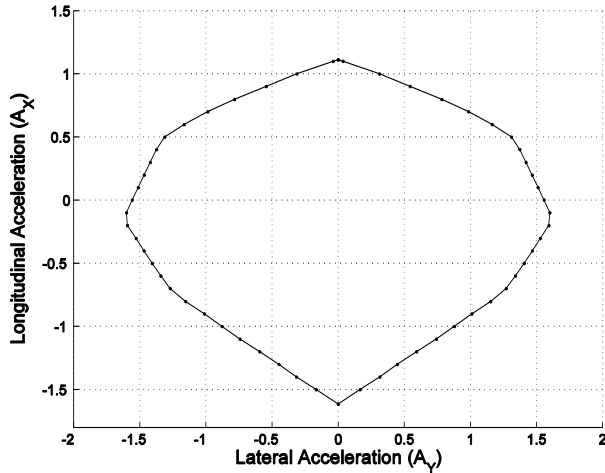


Figure 61: g-g diagram – 20 m/s

### 3.5. Future work

The work that has been presented here identifies the limits of the vehicle, without considering the role of the driver. The next step is to identify realistic limits of the combined driver and vehicle system. This will likely rely heavily on measures of stability and controllability such as the stability index and steering sensitivity. Additional stability measures from [25,27] also offer potential to identify sub limit levels of vehicle performance that represents the capabilities of a driver.

### 3.6. Conclusion

A process for creating free rolling  $C_N$ - $A_Y$  and  $C_N$ - $C_Y$  diagrams was presented and extended to the creation of MMD surfaces at constant longitudinal acceleration. When a number of these MMDs are combined, the overall working envelope of the vehicle can be represented. Using diagrams over a range of speeds and longitudinal accelerations, information about vehicle stability and controllability can be presented concisely.

#### **4. Lap Time Simulation: Quasi-Transient Lap Time Simulation via Acceleration-Moment Limit Surfaces**

Abstract:

Quasi-transient lap time simulation is introduced, which is an extension of quasi-static lap time simulation that allows yaw dynamics to be included in a simple lap simulation. The quasi-transient simulation method maintains the benefits of quasi-static simulation, including the overall simplicity of the method as well as fast computation. In place of the typical “g-g” diagram, a Limit Acceleration Surface (LAS) is used to represent the longitudinal, lateral, and yaw acceleration limits of the vehicle as it traverses a given path. The method is first developed using a simple octahedral LAS, which is defined by peak lateral, longitudinal, and yaw performance, then further demonstrated using a general LAS. Vehicle stability and controllability profiles will be created in addition to velocity, acceleration, vehicle slip and steered angle profiles. Results of a quasi-transient simulation are compared to the results of a corresponding quasi-static simulation.

## 4.1. Introduction

A large range of lap time simulation tools are available from very simple steady state simulations to complicated transient multi-body simulations. There are advantages at both ends of the spectrum, with the simplicity and the ease of interpretation of steady state and quasi-static simulations at one end, and the ability to represent extremely complicated behavior using transient simulations at the other. The goal of this investigation is to start with a simple quasi-static lap time simulation and increase its capability by including yaw dynamics without significantly increasing the complexity of the method. The addition of the yaw degree of freedom allows investigation of yaw dynamics, including stability and controllability, which is not possible with quasi-static methods.

Quasi-Static (or quasi-steady state) Simulation (QSS) methods presented in [28,29] start with a “g-g” diagram representing the combined limit acceleration of the vehicle in the longitudinal and lateral directions. Using the g-g diagram and a driven line, an optimal speed profile for the minimum lap time can be directly created. A similar method will be used to perform Quasi-Transient Simulation (QTS), but instead of performing a lap on the limit of a g-g diagram, the lap will be performed on the limit of a three dimensional Limit Acceleration Surface (LAS) representing the lateral, longitudinal, and yaw acceleration limit performance of the vehicle. In addition to generating a velocity profile and the associated accelerations along the path, sensitivities of vehicle accelerations to steered angle and vehicle slip angle will also be created and can be used to understand the stability and controllability of the vehicle.

This presentation will include a general background of lap time simulation as well as further justification for the quasi-transient method. This will be followed by the development and demonstration of quasi-transient lap time simulation. The vehicle being simulated represents a Formula Student (Formula SAE) vehicle, which is a racecar designed and built by students for collegiate design competitions around the world.

## 4.2. Background

Early examples of lap time simulation are presented in [11] and are as simple as dividing a path into curved and straight sections with speeds in the corners determined by steady state lateral

acceleration, and speed on the straights determined by pure driving and braking. These pure steady state simulations could be carried out with a pen and paper, and are believed to have been first used in the mid 1950's by Mercedes-Benz. These simple simulations were the starting point for the increasingly sophisticated lap time simulation tools used today.

In [30], a “quasi-dynamic” lap time simulation is presented that can perform simulations relatively quickly (~5 minutes) on a personal computer. This work was published in 1994 and provides the earliest reference that shows the possibility of a somewhat sophisticated model running efficiently on a personal computer. The method used simplified lateral, longitudinal, and yaw equations of motion, and iteratively optimizes the velocity profile of the vehicle on a known path. While this method included yaw dynamics in its solution, the quasi-static method developed later provided significant improvements in computational speed and generality of the vehicle model used.

A QSS method is well described in [28]. This simulation tool uses a defined driving line along with a pre-calculated speed dependent g-g diagram to determine an optimal velocity profile. The most significant feature of this simulation method is the pre-calculation of the g-g diagram and the reverse calculating braking zones. This is a significant improvement over the previous described method, as it allows direct identification of braking points instead of identifying them with an iterative method. It is fast while not significantly sacrificing accuracy. This method is similar to the one that will be used in QTS.

There are other variations of the quasi-static method. In [31], the same procedure of reverse calculating braking zones is used, but the vehicle behavior is calculated at the time of simulation. With this method, the time spent generating the g-g diagram is saved at the expense of identifying the vehicle performance limits while generating the velocity profile. In [28,32,33,34,35] methods are that identify the optimal driving line as well as the minimum lap time. Each variation affords its own advantages, but it is not clear from the literature if there is one quasi-static method that is significantly superior to the other.

A rigorous theoretical basis for the quasi-static method is provided in [36,37,38,39] by formalizing the identification of optimal velocity profiles for a point traveling on a line with

acceleration constraints. The acceleration limits imposed can be as simple as a circle or ellipse, or can be based on speed dependent g-g diagrams that are generated from arbitrarily complex vehicle models. This formalization had been lacking in many of the previous works despite their successful use. Although the developments are specific to the quasi-static method, the same concepts can be applied to the quasi-transient method.

On the other end of the complexity spectrum is a transient simulation method developed and presented in [40,41,42,43]. This method uses a 7-degree of freedom vehicle model and simplified representations of the suspension to approximate load transfer while maneuvering and applies optimal control techniques to identify the optimal lap of a Formula 1 car on a particular circuit. In several studies, this tool is used to identify the sensitivity of vehicle performance to various parameters such as vehicle mass or yaw inertia. One of the interesting results of [41] was that the effect of yaw inertia on lap time was quite small, but could be significant when looking at the stability of the vehicle. These simulations are the most advanced of any that have been identified in the research, but at significant computational cost as simulations can take over 24 hours on a personal computer. Because of the computational cost, using this type of model for understanding the sensitivity of vehicle performance to parameter variation is not practical unless significant computational resources are available.

The quasi-static simulation from [28] is compared to the transient method described in [40,41,42,43] by simulating the performance of a Formula 1 car. The center of gravity location is modified and the simulations are run again. This approach allowed the researchers to show that, despite differences in overall lap times, their simpler and faster model was able to predict effects of a setup change similar to the more complex and slower transient model with a computation time of only 60 seconds.

Additional comparisons are made of steady state, quasi-static and transient simulations in [44]. The results show that, due to the pure steady state model's simplicity, the simulated behavior is not representative of typical vehicle performance. However, both quasi-static and transient models showed behavior characteristic of what is observed on a racetrack. The transient model is then used to demonstrate the effect of yaw inertia on vehicle performance in a maneuver.

The quasi-transient simulation developed in the following sections begins with the same principles as the quasi-static method and takes a step towards the capabilities of transient methods and attempts to achieve the benefits of both. QTS will rely on a pre-calculated performance envelope, and the velocity profile will be identified for a given driving line by solving corner exit and corner entry in the forward and reverse directions in the same way as the quasi-static method. Unlike typical quasi-static methods, yaw dynamics will be included, which will allow investigation of vehicle behavior not possible with the quasi-static method.

### 4.3. Necessary Concepts

Before starting, a few concepts are covered that are important for the subsequent development. Areas covered are, finite difference equations, derivative notation, and curvilinear motion.

#### 4.3.1. Finite Difference Equations

Throughout the following sections, finite difference equations are used to approximate derivatives of various parameters, such as position, velocity, or curvature. In each circumstance, a finite difference equation will be selected to fit the needs of the application. Depending on the circumstance, derivatives may be calculated using forward or centered difference equations. First derivatives are approximated by either the first order finite difference equation shown in (79), or the second order finite difference shown in (80). Second derivatives are calculated using the second order finite difference equation in (81).

$$\frac{dx}{dy} = \frac{x_{n+1} - x_n}{\Delta y} \quad (79)$$

$$\frac{dx}{dy} = \frac{x_{n+1} - x_{n-1}}{2\Delta y} \quad (80)$$

$$\frac{d^2x}{dy^2} = \frac{x_{n+1} - 2x_n + x_{n-1}}{\Delta y^2} \quad (81)$$

### 4.3.2. Derivative Notation

Several shorthand notations will be used in the following sections, the first of which is the “dot” notation that will refer to derivatives with respect to time  $t$  as shown in (82, 83). Similarly, the “prime” notation will be used to represent derivatives with respect to distance traveled along the path  $s$  as shown in (84, 85).

$$\dot{x} = \frac{dx}{dt} \quad (82)$$

$$\ddot{x} = \frac{d^2x}{dt^2} \quad (83)$$

$$x' = \frac{dx}{ds} \quad (84)$$

$$x'' = \frac{d^2x}{ds^2} \quad (85)$$

### 4.3.3. Curvilinear Motion

The QTS method is based on curvilinear motion of a body traversing a known path in two dimensions. In the following paragraphs, the typical representation of curvilinear motion is extended to meet the needs of QTS. If a full development of curvilinear motion is desired, a general dynamics text such as [45] should be consulted.

When describing curvilinear motion, the dynamics of the vehicle are decomposed into a tangential part that is parallel with the path, and a radial part that is normal to the path. The velocity vector  $V$ , which describes the velocity of the body, is always tangent to the path with magnitude  $v$ . The acceleration vector  $A$  is made up of a tangent component  $a_t$  and a normal part  $a_n$  with values defined in (86, 87), where  $k$  is the path curvature.

$$a_n = \dot{v} \quad (86)$$

$$a_t = kv^2 \quad (87)$$

Typically, the body's rate of rotation about the vertical axis (orthogonal to both the normal and radial directions), or yaw rate  $\omega$ , is completely determined by the velocity  $v$  and path curvature  $k$  as shown in (88), and the yaw acceleration  $\dot{\omega}$  shown in (89).

$$\omega = kv \quad (88)$$

$$\dot{\omega} = \dot{k}v + ka_t \quad (89)$$

In order to include yaw dynamics that are not directly determined by the path and velocity, a vehicle slip angle term  $\beta$  is introduced which represents the angle between the heading of the vehicle and its direction of travel as is typical in an SAE coordinate system defined in [23]. With this addition, yaw velocity of the body is affected by the vehicle slip velocity as shown in (90), and similarly, the yaw acceleration is affected as shown in (91). It is worth noting that due to the definition of slip angle, its sign, and the sign of its derivatives, is opposite to that of similar motions of the overall vehicle orientation.

$$\omega = kv - \dot{\beta} \quad (90)$$

$$\dot{\omega} = \dot{k}v + ka_t - \ddot{\beta} \quad (91)$$

It is useful to represent the derivatives of curvature and slip angle with respect to path distance instead of time, in which case (90, 91) become (92, 93).

$$\omega = (k - \beta')v \quad (92)$$

$$\dot{\omega} = (k' - \beta'')v^2 + ka_t \quad (93)$$

#### 4.4. General Implementation

The QTS method is iterative and begins with an initial simulation that neglects the effect of vehicle slip angles. The heading of the vehicle is aligned with the path, and the limits of vehicle performance are not affected by yaw velocity. The result is an initial velocity profile that is used to create estimates of vehicle yaw rate and slip angle along the path. The lap is simulated again using the estimated yaw velocity and vehicle slip angle to refine the velocity profile. This process is repeated until the solution converges.

#### 4.4.1. Path Representation

The path is represented by a profile of signed curvature with respect to distance traveled. In order for the simulation to represent realistic behavior, the curvature profile must be both continuous and smooth. The physical reason for this requirement is that path curvature, along with speed and vehicle slip rate, is used to calculate yaw rate, and discontinuities in the curvature profile create discontinuities in the yaw rate. Discontinuities in yaw rate would require an infinite yaw moment, which is not possible. Similarly, non-smooth (or “kinked”) curvature profiles will result in non-smooth yaw rate and require step changes in yaw moment. This behavior is physically unrealistic and will lead to numerical problems when the lap is simulated. If a smooth profile is not available, filtering a discontinuous or non-smooth curvature profile may produce acceptable results.

The curvature profile used in the following sections comes from GPS data collected by the Global Formula Racing team on their 2011 Formula Student car. The track driven is the “asymmetric oval” and is shown in figure 62. The asymmetric oval course is easy to set up and is regularly used by the team for standardized vehicle testing. It is made up of one large and one small radius corner, connected by a straight section on one side, and a three-cone slalom on the other. The course can be driven in either direction, but in the following demonstrations, only the clockwise direction is considered. More information concerning the asymmetric oval and test procedures can be found in [24].

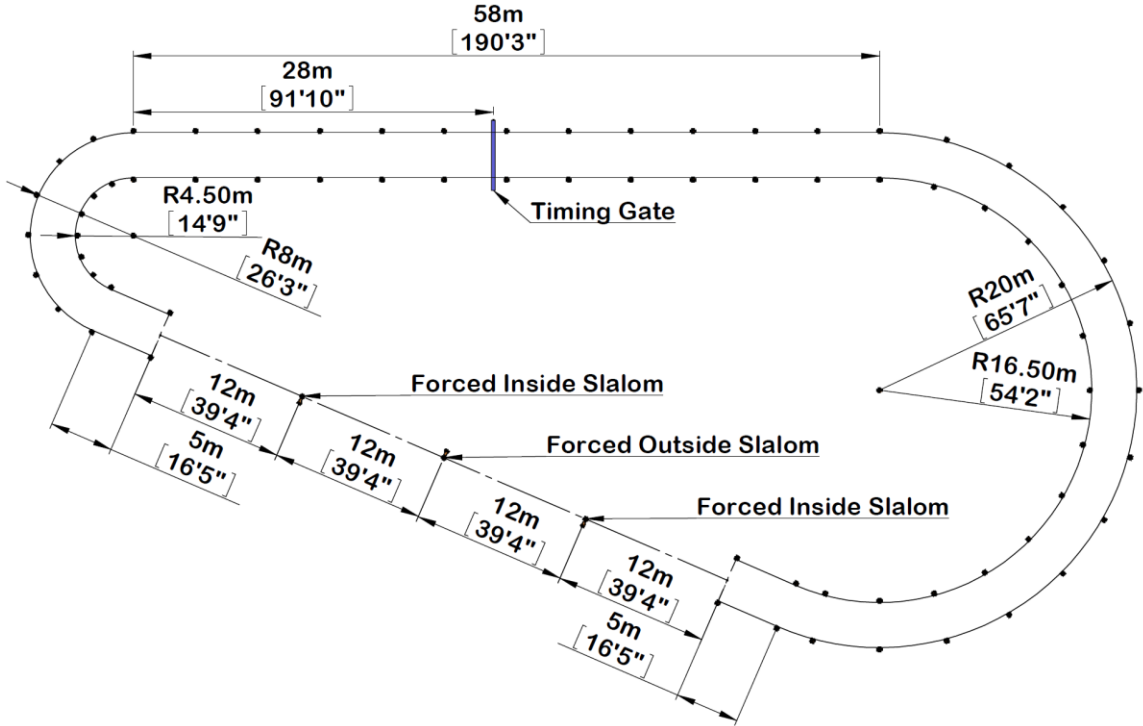


Figure 62: Asymmetric oval test track

In order to reduce the effect of lap-to-lap variation, GPS data from five consecutive flying laps is combined to create a standard lap. This standard lap is filtered to remove measurement noise and high frequency path oscillations. A second order low-pass Butterworth filter with a cutoff frequency  $0.25 \text{ m}^{-1}$  ( $0.076 \text{ ft}^{-1}$ ) is applied in the forward and reverse directions (using the MATLAB command `filtfilt`). Applying the second order filter in the forward and reverse directions, results in a fourth order filter with relatively small phase distortion of the filtered path. Curvature is calculated from X-Y coordinates using (94). Derivative terms are represented as second order finite difference approximations shown in (80, 81). Figures 63 and 64 show the resulting track map and curvature profile using 500 path segments ( $\sim 0.4\text{m}$  per segment). The track is a closed circuit where the first point and last point are the same physical location and share the same conditions. Throughout the following development, the simulations will represent a flying lap where the initial conditions at the start/finish line are the same as final conditions at the end of the lap.

$$k_n = \frac{x'y'' - y'x''}{(x'^2 + y'^2)^{3/2}} \quad (94)$$

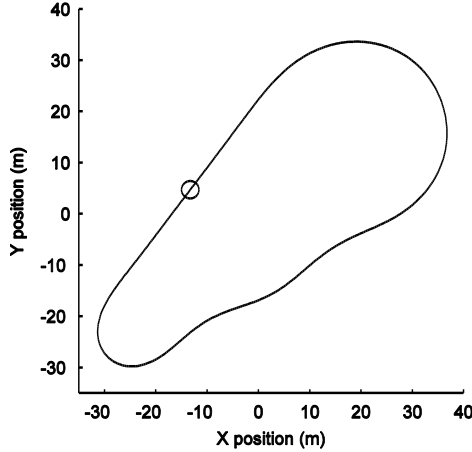


Figure 63: Track map from GPS

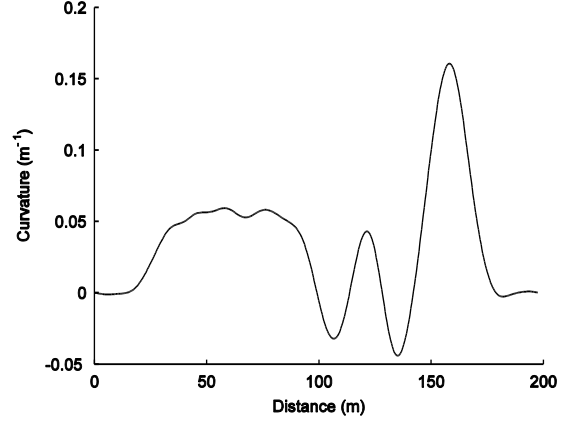


Figure 64: Curvature profile from GPS

#### 4.4.2. Vehicle Model

The performance envelope of the vehicle will be described as a Limit Acceleration Surface (LAS) that represents the combined lateral, longitudinal, and yaw acceleration of the vehicle. Two LASs will be used in this paper. The first surface resembles a diamond and is made of eight triangular faces (octahedron). This is the simplest shape that can reasonably represent the performance envelope, and is useful for initial development of the simulation methods. Figure 65 shows a three-dimensional projection of the simple limit surface and figures 66 through 68 show three normal views. Figure 66 shows the characteristic shape of a Milliken Moment Diagram. For peak positive lateral acceleration, the yaw moment is negative which indicates that the vehicle is stable, or will push/plow, at the limit. Figure 67 can be roughly interpreted as a g-g diagram, as it represents the combined lateral and longitudinal acceleration limits, although the yaw moment will be nonzero along most of the limit. The octahedral LAS is symmetric with respect to right and left hand cornering, and asymmetric with respect to driving and braking.

The limit surface is divided into upper and lower limit surfaces. Faces are included in the upper surface if the longitudinal component of their outward normal is positive and included in the

lower surface otherwise. The upper surface can be thought of primarily as representing positive longitudinal acceleration (driving), and the lower as negative longitudinal acceleration (braking), but as can be seen in figures 67 and 68, the boundary between the upper and lower surfaces is non-zero and part of the upper surface represents negative longitudinal acceleration. The boundary curve between the upper and lower surfaces is an important feature of the LAS and will be referred to as the limit surface boundary curve (LSBC). In addition to limit accelerations, vehicle slip angles and steer angles are known for each vertex and will be used to determine vehicle slip angle and steer angle over the lap.

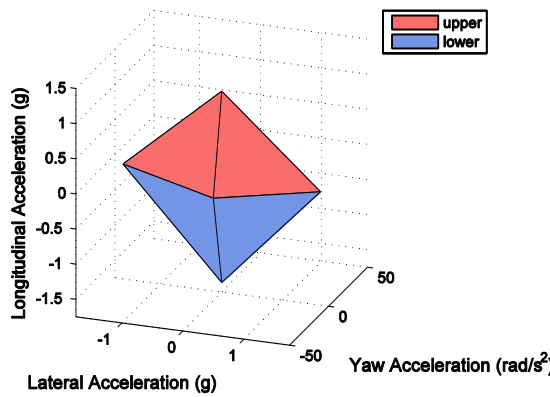


Figure 65: Octahedral LAS (3d)

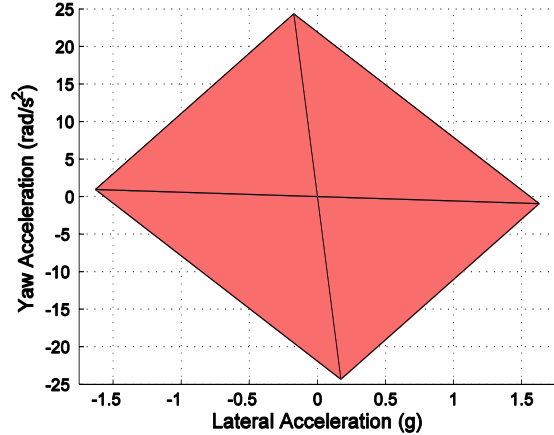


Figure 66: General LAS ( $a_n - \dot{\omega}$ )

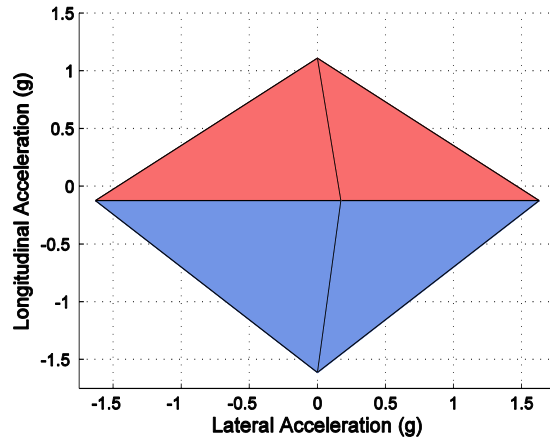


Figure 67: Octahederal LAS ( $a_n - a_t$ )

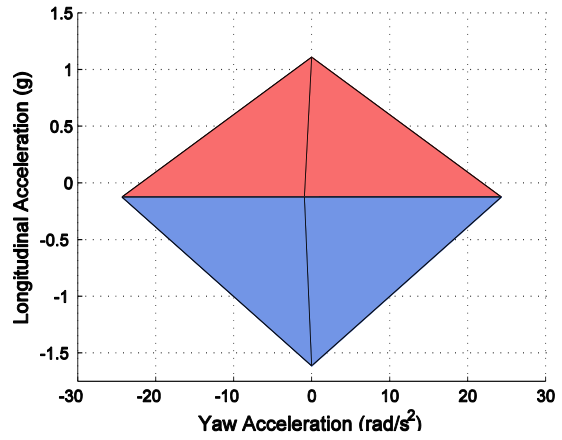


Figure 68: Octahederal LAS ( $\ddot{\omega} - a_t$ )

The surface shown in figures 65 through 68 can be thought of a three-dimensional extension of a Milliken Moment Diagram that includes longitudinal acceleration. The diagram presented is analogous to a  $C_N$ - $C_Y$  diagram created with zero yaw velocity, which can also be interpreted as representing behavior on an infinite radius (zero curvature). In order to represent vehicle behavior over a wide range of speeds and yaw velocities, corresponding LASs are generated over a range of effective curvatures  $k_{eff}$ , where effective curvature is defined as shown in (95). Effective curvature is equal to path curvature only when (96) is satisfied, which is a steady state cornering constraint. Surfaces are created with effective curvatures of  $0.075\text{ m}^{-1}$  and  $0.15\text{ m}^{-1}$ , which correspond to steady state lateral accelerations of 0.75 and 1.5 g at  $10\text{ m/s}$ . This range represents what is seen in acquired data, as well as the simulations to be performed. The overall change in shape of the LAS over this range of effective curvature is small, but the changes in vehicle slip angle and steer angle are significant. Quadratic polynomials of surface vertices are used to interpolate continuously between calculated LASs. Symmetry is used to represent negative curvatures by interpolating using the absolute value of  $k_{eff}$ , and reversing the sign of lateral acceleration, yaw acceleration, slip angle and steer angle, when  $k_{eff}$  is negative.

$$k_{eff} = \frac{\omega}{v} \quad (95)$$

$$\omega = \frac{a_n}{v} \quad (96)$$

A second LAS surface made up of significantly more elements is shown in figures 69 through 72, and will be used to demonstrate QTS with a surface that is more general. Once again, the surface is split between upper and lower segments based on the orientation of the individual face normal vectors. In this example, the boundary between the upper and lower surfaces is not simply defined at a single longitudinal acceleration or a single plane.

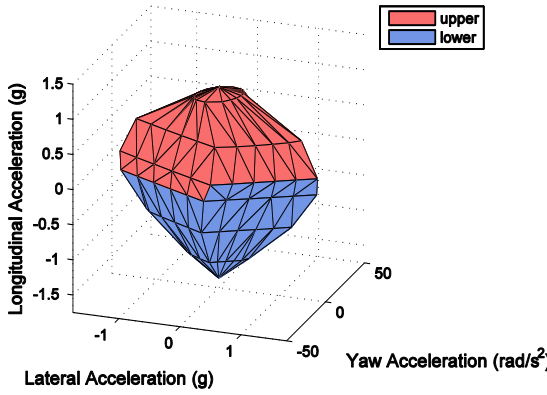
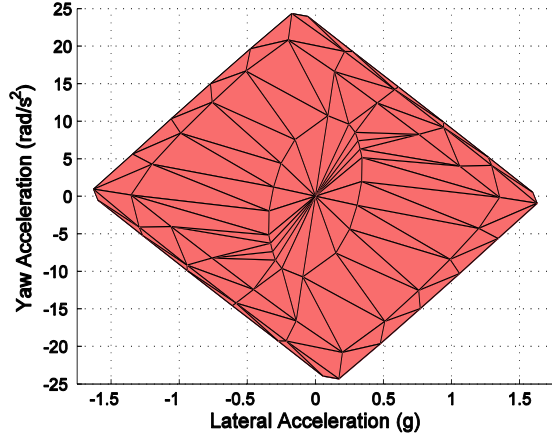
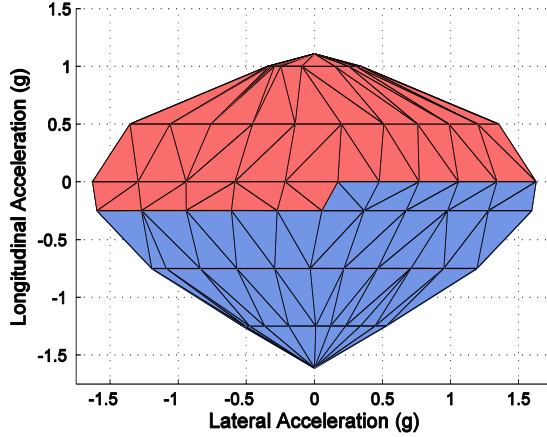
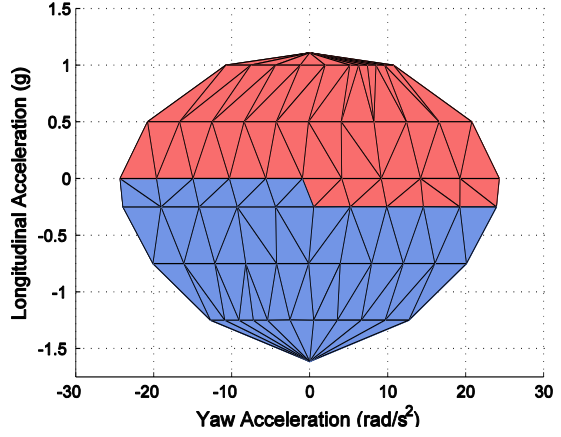


Figure 69: General LAS (3d)

Figure 70: General LAS ( $a_n - \bar{\omega}$ )Figure 71: General LAS ( $a_n - a_t$ )Figure 72: General LAS ( $\bar{\omega} - a_t$ )

It is important to note that the topology of the surfaces must remain constant across the range of effective curvatures used. That is, the edges that form the LSBC must always form the LSBC and it follows that faces cannot change from upper to lower surfaces or vice versa.

#### 4.4.3. Boundary Speed Profile

With the vehicle limits and path defined, generation of the limit speed profile (LSP) begins by identifying a boundary speed profile (BSP) that is based on the lateral, longitudinal, and yaw accelerations along the LSBC. The BSP represents the fastest speed possible at each point on the path without considering how it could reach that speed, or whether the vehicle could continue further on the desired path. This is the same concept as determining the maximum

steady state speed a vehicle could travel at each point on a curvature profile considering only maximum lateral acceleration. In this simple steady state case, where longitudinal and yaw dynamics are ignored, the velocity at each point is determined by the instantaneous path curvature and the maximum lateral acceleration as shown in (97).

$$v = \sqrt{\frac{a_n}{k}} \quad (97)$$

To extend this concept to include yaw dynamics, the maximum combined lateral and yaw acceleration must be considered, which is represented by the LSBC. The appropriate boundary speed will result in a combined acceleration that lies on the LSBC.

Before the BSP can be identified, each of the line segments forming the LSBC is parameterized based one of its endpoints and a vector joining the first endpoint to the next. For example, the octahedral limit surface has four boundary edge segments. Each of the segments is parameterized with a point  $A_0$  and edge direction  $A_1$  such that any point on a given segment can be described using (98-100) where  $\chi$  varies between 0 and 1.

$$A_0 = [a_{t0} \quad a_{n0} \quad \dot{\omega}_0] \quad (98)$$

$$A_1 = [a_{t1} \quad a_{n1} \quad \dot{\omega}_1] \quad (99)$$

$$A = [a_t \quad a_n \quad \dot{\omega}] = A_1\chi + A_0 \quad (100)$$

For any point along the curvature profile, the boundary speed will satisfy (101-103) and  $\chi$  must be between 0 and 1 (and be real). Derivatives of curvature and slip angle are calculated using the centered difference equations (80, 81).

$$a_t = a_{t1}\chi + a_{t0} \quad (101)$$

$$a_n = a_{n1}\chi + a_{n0} = kv^2 \quad (102)$$

$$\dot{\omega} = \dot{\omega}_1\chi + \dot{\omega}_0 = (k' - \beta'')v^2 + ka_t \quad (103)$$

Solving (101-103) for  $v$  results in (104). As would be expected, when  $a_{n1}$  is zero and  $a_n$  has a constant limit, (104) reduces to the steady state result from (97).

$$v = \sqrt{\frac{a_{n0} - a_{n1}(a_{t0}k - \dot{\omega}_0)/(a_{t1}k - \dot{\omega}_1)}{k + a_{n1}(k' - \beta'')/(a_{t1}k - \dot{\omega}_1)}} \quad (104)$$

It is not initially known on which edge segment of the LSBC the boundary speed will lie for each location along the path. To determine which segment the boundary surface lies on, each segment is checked in succession until a solution is found that lies on the LSBC. Solving for the boundary speed at every location along the path yields the BSP. Figure 73 shows the BSP for the octahedral surface on the asymmetric oval.

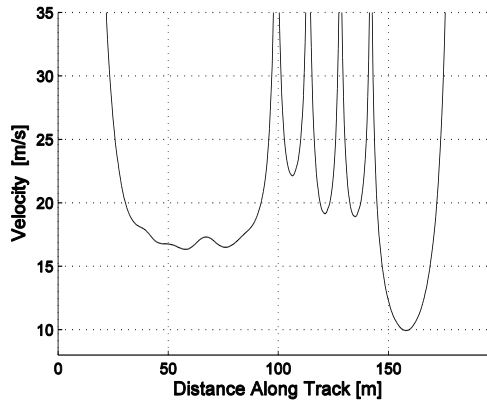


Figure 73: Boundary speed profile

#### 4.4.4. Critical Points

The boundary speed profile represents the maximum instantaneous performance on the curvature profile, but it does not consider the longitudinal acceleration required to move from one path segment to the next. Most points on the BSP are not feasible, and only critical points along the path are realizable within the performance limits of the vehicle. In order to identify these critical points, the longitudinal acceleration that would be required to traverse the BSP is compared with the longitudinal acceleration at the corresponding point on the LSBC. The boundary edge longitudinal acceleration is found using the boundary speed  $v$  and (105), which is found by solving (102) for  $\chi$  and substituting into (101). Figures 74 and 75 show the longitudinal acceleration required to transverse a portion of the BSP compared to the

longitudinal acceleration on the LSBC for the octahedral LAS and the general LAS. Critical points occur where the two acceleration curves cross.

$$a_t = a_{t1} \left( \frac{k v^2 - a_{n0}}{a_{n1}} \right) + a_{t0} \quad (105)$$

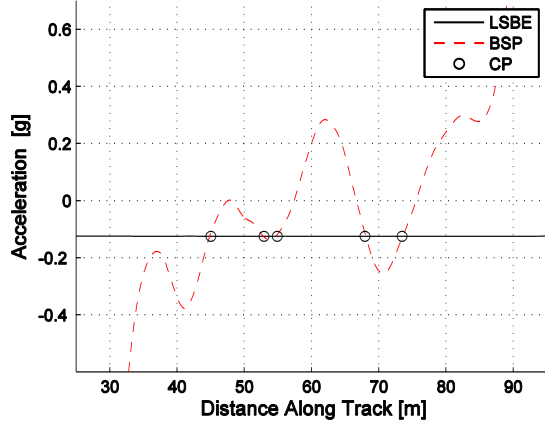


Figure 74: Critical points – Octahedral LAS

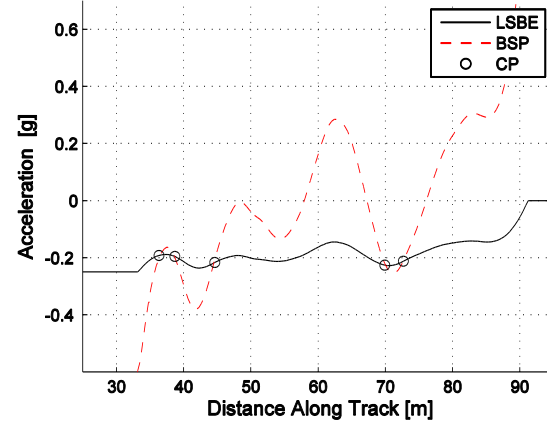


Figure 75: Critical points – General LAS

In figure 74, representing the octahedral LAS, the longitudinal acceleration on the boundary surface edge is a constant  $-0.125g$ , so all critical points occur where the boundary speed profile acceleration is equal to  $-0.125g$ . In figure 75, representing the general LAS, the longitudinal acceleration on the boundary surface edge varies, and critical points can occur over a range of acceleration values between  $-0.25$  and  $0g$ . A physical way of understanding the implications of this is that at the critical points, the BSP and the LSP will be coincident and tangent. If the LSP was not coincident with the BSP then the speed at the critical point would not be a limit speed (it would be either too fast or too slow), and if the curves are coincident, but not tangent, the LSP would cross the BSP resulting in an unrealizable speed.

Using the steady state example once again (neglecting yaw dynamics), if the maximum lateral acceleration corresponds with zero longitudinal acceleration then the critical points will occur at minimums of the boundary speed profile, which occur at a local curvature maximums (radius minimums). This is the intuitive case where the apex of the corner is the critical point and represents the mid-corner change from braking to driving. In the general case, critical points

limit corner speed, but as has been shown, they do not have to occur at the local minimum radius of a corner or correspond with minimum cornering speeds.

Because the path is discretized, the exact location of the critical point will lie between two points on the path. Choosing the nearest point can be an acceptable estimate, but it will generally lead to a slightly infeasible speed. It could be acceptable to ignore the small infeasibility, as it will decrease with decreased path grid spacing. But, as the speed at the critical point significantly affects the rest of the speed profile, it is worth improving the estimate of the critical point location and its associated velocity and longitudinal acceleration. This is done by using the difference in accelerations of the BSP and LSBC at the nearest discretization, along with the slopes of the two acceleration curves at the same point, with derivatives calculated using the centered difference formula from (80). Equation (106) shows how the normalized critical distance  $c_n$  is calculated, which is the distance from the nearest discretized point to the second order accurate critical point. The associated longitudinal acceleration and speed at this critical point is found using (107, 108). This improves the estimate of the critical point's locations, but is still only an approximation of the critical point location and could lead to infeasible speeds.

$$c_n = \frac{a_{tBSP} - a_{tLSBE}}{a'_{tBSP} - a'_{tLSBE}} \quad (106)$$

$$a_{tcrit} = a_{tBSP} + c_n a'_{tBSP} \quad (107)$$

$$v_{crit} = v_{BSP} + a_{tBSP} c_n + \frac{1}{2} a'_{tBSP} c_n^2 \quad (108)$$

This critical speed is not on the discretized set of points that has been defined for our solution, so it is used to find the limit speeds of the points on either side of it. These points will then be used as the starting points for simulation of the limit profile. Using (109), the normalized critical distance to the critical point is modified depending on the direction to the nearest point. Limit speeds in the forward and reverse directions are identified using (110, 111).

$$c_d = \begin{cases} -c_n, & c_n < 0 \\ 1 - c_n, & c_n \geq 0 \end{cases} \quad (109)$$

$$v_{Flim} = \sqrt{v_{crit}^2 + 2a_{tcrit}c_d\Delta s} \quad (110)$$

$$v_{Rlim} = \sqrt{v_{crit}^2 - 2a_{tcrit}(1 - c_d)\Delta s} \quad (111)$$

#### 4.4.5. Limit Speed Profile

Once critical points are identified, portions of the limit speed profile are created by propagating the limit speed in both the forward and reverse directions until either the boundary speed profile or a limit speed profile from another critical point is intersected. This process should be started with the lowest speed critical point, as critical points that are above the limit speed profile of other critical points are not feasible and do not need to be considered. After the portion of the limit speed profile is created for a critical point, another portion of the limit speed profile should be generated starting at the next lowest speed of the remaining feasible critical points. This process is repeated until no feasible critical points remain and the LSP is complete for the entire path.

The limit speed is propagated from one point to the next by identifying the speed at the neighboring point that results in a combined lateral, longitudinal and yaw acceleration that lies on the LAS. Equations (112-114) define the acceleration vector  $A$ , a point on the limit surface  $P$ , and the normal vector to the surface  $N$ . The distance  $D$  of the acceleration vector from a plane defined by  $P$  and  $N$  is calculated using (115). In order for the vehicle to perform on the limit, this distance must equal zero.

$$A = [a_t \quad a_n \quad \dot{\omega}] \quad (112)$$

$$P = [p_t \quad p_n \quad p_z] \quad (113)$$

$$N = [n_t \quad n_n \quad n_z] \quad (114)$$

$$D = (P - A) \cdot N = 0 \quad (115)$$

Longitudinal and yaw accelerations from (86, 92) are discretized and shown in (116, 118). Each uses the first order finite difference equation defined in (79), while lateral acceleration is defined in (117) and uses the average of the endpoint values in order to maintain symmetry of

the calculations. Using (119), longitudinal and yaw accelerations are written in terms of  $\Delta s$  in place of  $\Delta t$ . Accelerations are calculated based on the velocity  $v$ , path curvature  $k$ , and vehicle slip angle  $\beta$ , at points  $a$  and  $b$  along the path separated by a distance  $\Delta s$ . When simulating in the forward direction, point  $b$  follows point  $a$  along the path and  $\Delta s$  is positive, but the same equations can be used in the reverse direction by changing the order of the points along the path as well as the sign of  $\Delta s$ . In either case, point  $a$  can be thought of as the starting point (the known speed) and  $b$  as the result (the speed to be determined).

$$a_t = \frac{v_b - v_a}{\Delta t} = \frac{v_b^2 - v_a^2}{2\Delta s} \quad (116)$$

$$a_n = \left( \frac{k_a + k_b}{2} \right) \left( \frac{v_a + v_b}{2} \right)^2 \quad (117)$$

$$\dot{\omega} = \frac{\omega_b - \omega_a}{\Delta t} = [(k_b - \beta'_b)v_b - (k_a - \beta'_a)v_a] \frac{v_a + v_b}{2\Delta s} \quad (118)$$

$$\Delta t = \frac{2\Delta s}{v_a + v_b} \quad (119)$$

Using (116-119) and simplifying (115), results in (120), which is quadratic in terms of  $v_b$ , with constants  $C_0$ ,  $C_1$ , and  $C_2$  defined in (121-123). If the initial path segment velocity  $v_a$  is a feasible speed for driving the path segment (lies tangent to or below the BSP), there will be two unique solutions to the quadratic equation. One will be positive and the other negative. The positive solution is the one of interest, as the negative solution represents the vehicle first overshooting the distance  $\Delta s$ , then returning to the end point with a velocity in the opposite direction.

$$D = C_0 + v_b C_1 + v_b^2 C_2 = 0 \quad (120)$$

$$C_0 = n_t \left( p_t + \frac{v_a^2}{2\Delta s} \right) + n_n \left( p_n - \frac{v_a^2(k_a + k_b)}{8} \right) + n_z \left( p_z + \frac{v_a^2(k_a - \beta'_a)}{2\Delta s} \right) \quad (121)$$

$$C_1 = v_a \left( -n_n \frac{k_a + k_b}{4} + n_z \frac{(k_a - \beta'_a) - (k_b - \beta'_b)}{2\Delta s} \right) \quad (122)$$

$$C_2 = -n_t \frac{1}{2\Delta s} - n_n \frac{k_a + k_b}{8} - n_z \frac{k_b - \beta'_b}{2\Delta s} \quad (123)$$

The vectors  $P$  and  $N$  depend on what triangular segment of the LAS is used, and it is important that the correct segment is chosen for each step. When starting from a critical point, the initial face segment is selected by identifying the face that contains the segment of the LSBC that determined the boundary speed. When creating the LSP, the segment must be on the upper surface when propagating in the forward direction, and on the lower surface when propagating in the reverse direction. After each step, the accelerations should be checked to ensure that they lie within the edges of the LAS segment that was used to determine them. If the accelerations are outside the segment edges, then the other surface segments should be checked until the segment is found that contains a solution. As long as the step size is small enough, and the surface segments are large enough, it is likely that the solution will pass from a segment to one of its neighbors, so they should be checked first, followed by their neighbors. Figure 76 shows a three dimensional transparent projection of the octahedral LAS with the resulting accelerations plotted on its surface. Figures 77 through 79 show the three normal views of the same surface. Figure 80 shows the resulting velocity profile.

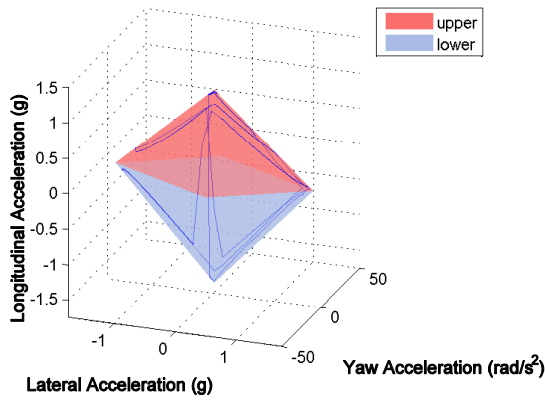


Figure 76: Octahedral LAS (3d) w/profile

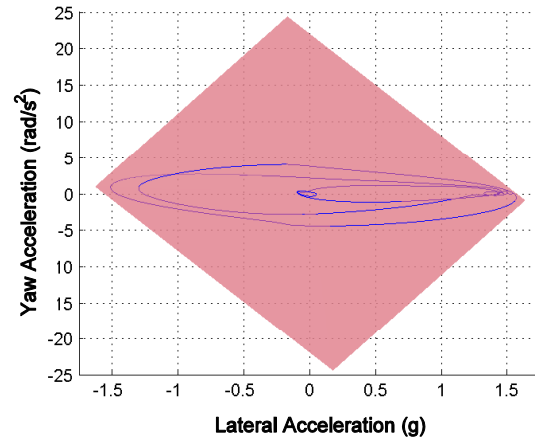


Figure 77: Octahedral LAS ( $a_n - \ddot{\omega}$ ) w/profile

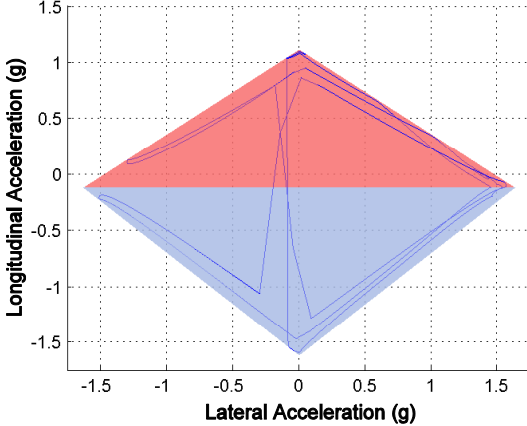
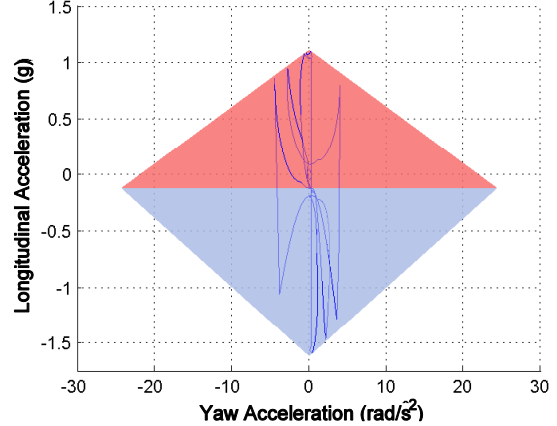
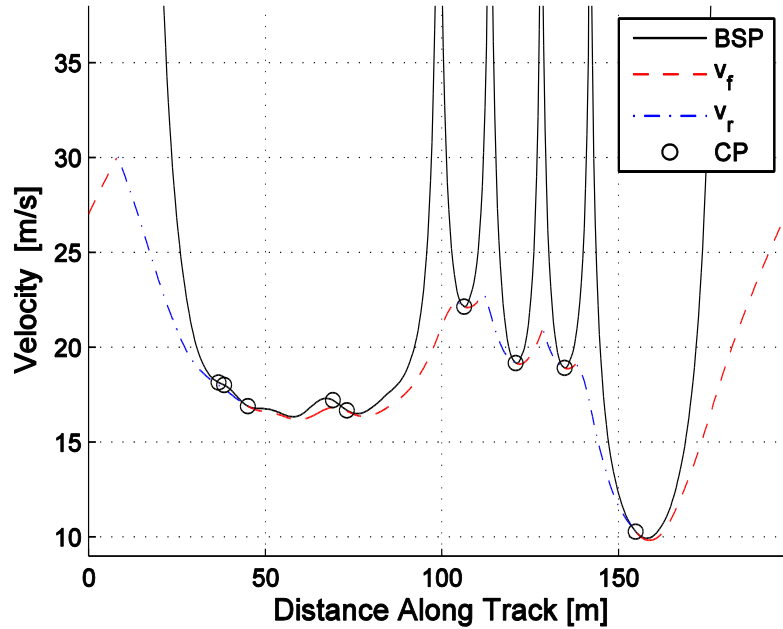
Figure 78: Octahedral LAS ( $a_n - a_t$ ) w/profileFigure 79: Octahederal LAS ( $\ddot{\omega} - a_t$ ) w/profile

Figure 80: LSP and BSP – Octahederal LAS

#### 4.4.6. Yaw Velocity and Slip Angle

The LSBC parameters  $A_0$  and  $A_1$  as well as vectors  $P$  and  $N$  for each limit surface segment are dependent on effective curvature. But, when both the BSP and the LSP are first calculated, the yaw velocity and vehicle speed profiles of the vehicle are not known and effective curvature cannot be calculated. Similarly, the vehicle slip angle profile is not known and cannot be used

when generating either the BSP or LSP. To identify the effective curvature and slip angle of the vehicle, the entire process of creating the BSP and LSP is performed with the effective curvature and vehicle slip assumed to be zero. As the LSP is propagated, the vehicle slip angle profile is created by identifying the slip angle at each point on the LAS. After the LSP is created, the effective curvature profile can be calculated using the speed, curvature, and vehicle slip profiles. In general, the LAS shape is not a strong function of effective curvature, and the effect of vehicle slip angle is secondary to that of the path curvature so the accelerations identified and the resulting speed profile are both good first approximations. Slip angle is a much stronger function of effective curvature and its first approximation will be inaccurate.

To improve the results, the process of creating the LSP can be repeated using the vehicle slip angle and effective curvature from the first iteration. This process can be repeated using the updated effective curvature and vehicle slip profiles until sufficient convergence is achieved. Figures 81 through 84 show comparisons of speed, accelerations, yaw rate and vehicle slip angle for the first, second and tenth iterations using the octahedral LAS. Each iteration takes less than 0.25 seconds when using the octahedral LAS and less than 0.5 seconds when using the general LAS.

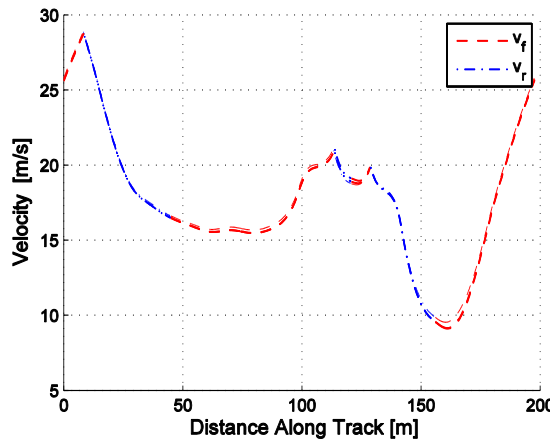


Figure 81: Velocity profile – Iteration comparison

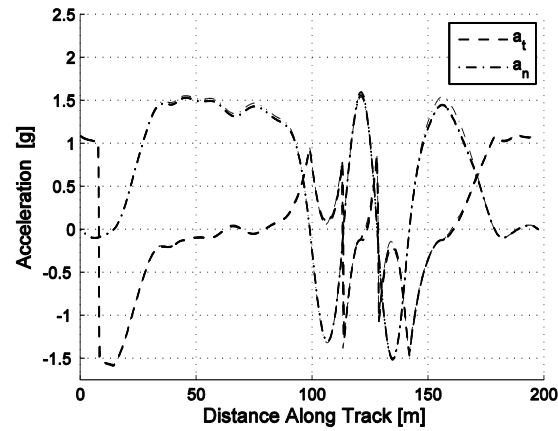


Figure 82: Acceleration profiles – Iteration comparison

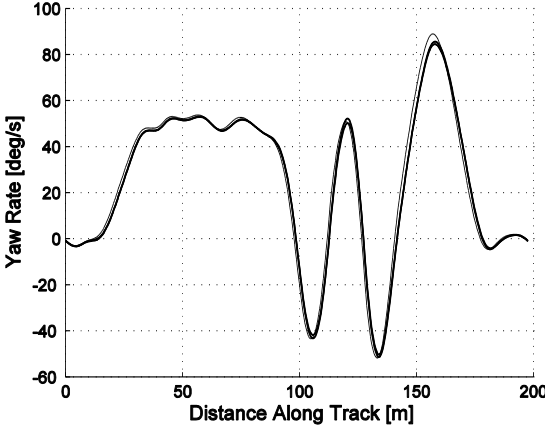


Figure 83: Yaw rate profile – Iteration comparison

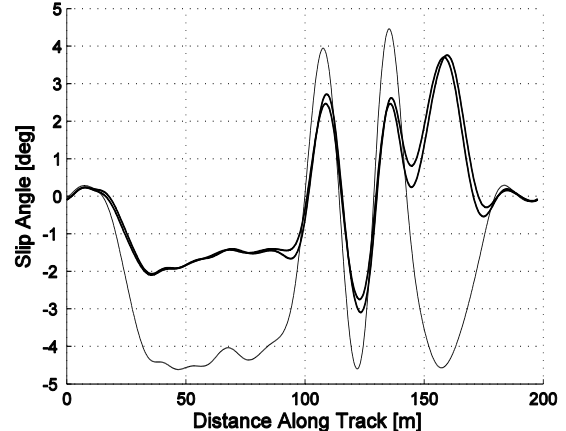


Figure 84: Vehicle slip profile – Iteration comparison

The velocity, acceleration, and yaw rate profiles in the figures above are almost indistinguishable, and the small differences are shown more clearly in figures 85 through 88, which show a magnified segment of the same data. The largest change is in the vehicle slip angle, while some of the traces are still indistinguishable even when magnified. Figure 89 shows how the overall lap time changes as the solution converges. The change from the first to second iteration is approximately 1% of the total lap time with subsequent iterations resulting in changes of less than 0.1%, and quickly decreasing after several iterations. For the remainder of this work, five iterations will be used.

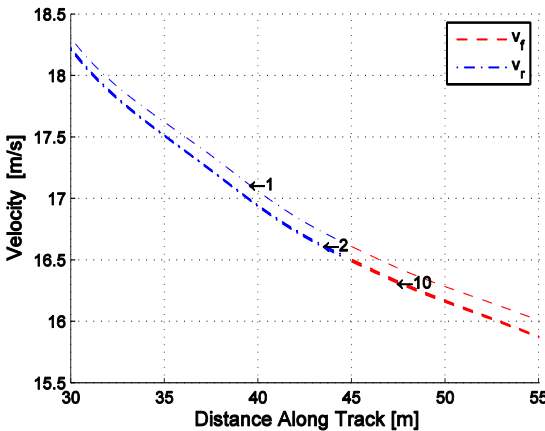


Figure 85: Velocity profile – Iteration comparison segment

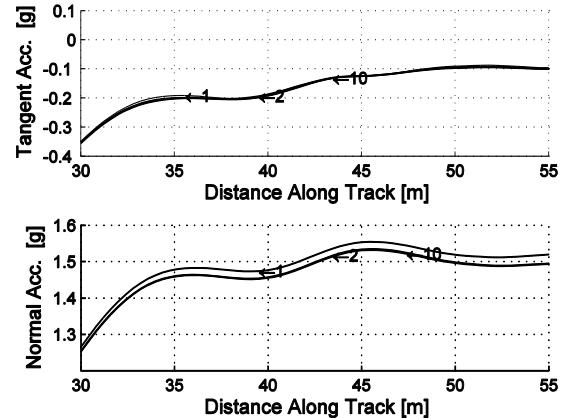


Figure 86: Acceleration profiles – Iteration comparison segment

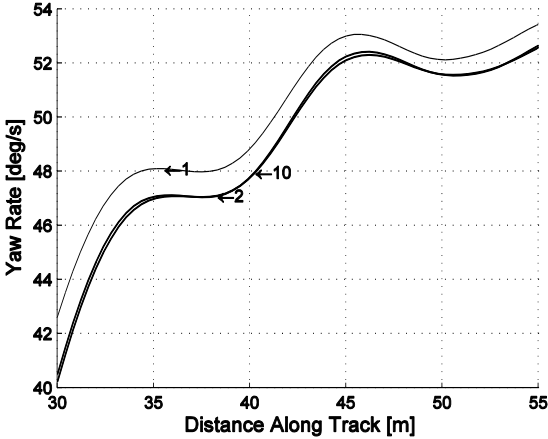


Figure 87: Yaw rate profile – Iteration comparison segment

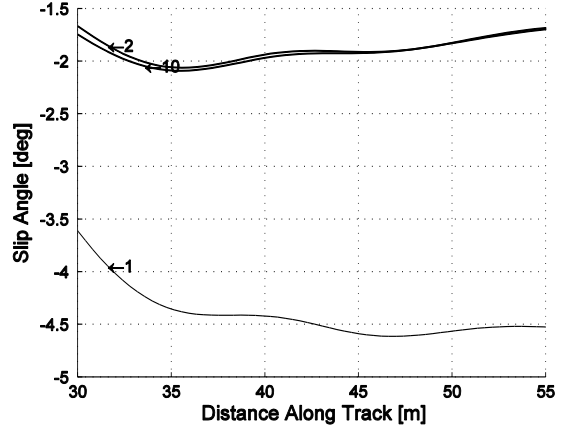


Figure 88: Vehicle slip profile – Iteration comparison segment

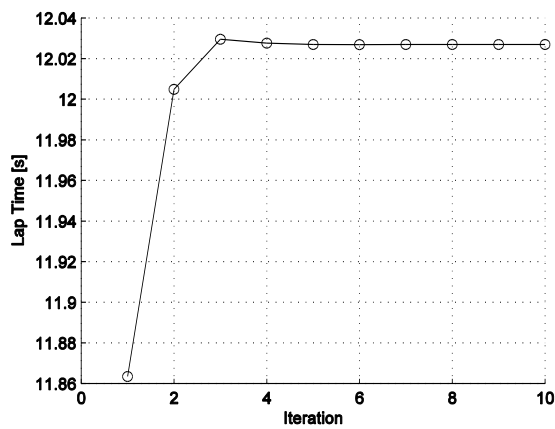


Figure 89: Lap time convergence

#### 4.4.7. Drive-Brake Continuity

Vehicle performance at critical points occurs at the edge of the LAS that separates the upper and lower surfaces, and the acceleration of the vehicle, as well as the vehicle slip angle is continuous at the transition. The same is not necessarily true for the transitions from the upper to lower surface that occurs at the braking points. At these points, the vehicle's acceleration is discontinuous as it transitions from a point on the upper surface to a point on the lower surface. Although transitions from driving to braking are often very fast, the instantaneous change from driving to braking produced by the simulation is not realistic as there will always be some

amount of transition time as the driver applies the brakes, releases the throttle, and the weight of the vehicle shifts forward. Accurately representing the dynamics of this transition is beyond the scope of this simulation, but must be dealt with because the instantaneous transition from driving to braking causes discontinuities in the vehicle slip angle. When the solution is iterated, and the discontinuities are reached, unrealistically large yaw moments are required due to the discontinuous slip angle profile. Figure 90 shows the vehicle slip angle profile created after the first two iterations using the general LAS. After the first iteration, there are discontinuities in the vehicle slip profile which cause large spikes in the vehicle slip profile in the second iteration. As iterations continue, the vehicle slip profile gets progressively more erratic and is not representative of normal vehicle behavior. A reasonable solution to this problem is to apply a filter to the vehicle slip angle profile. By applying a 2<sup>nd</sup> order Butterworth filter with a cutoff frequency of 5 m<sup>-1</sup> in both the forward and reverse directions, a suitably smooth vehicle slip profile is created that acceptably represents the original version. Figure 91 shows the vehicle slip profile after five iterations. The discontinuities are still present in the unfiltered profile, but the filtered profile, which is used in the simulation, is smooth.

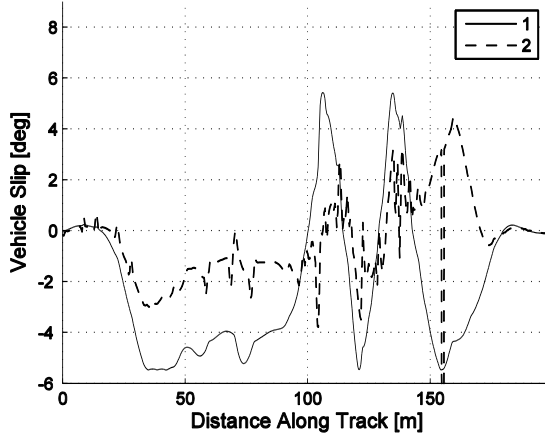


Figure 90: Vehicle slip discontinuities

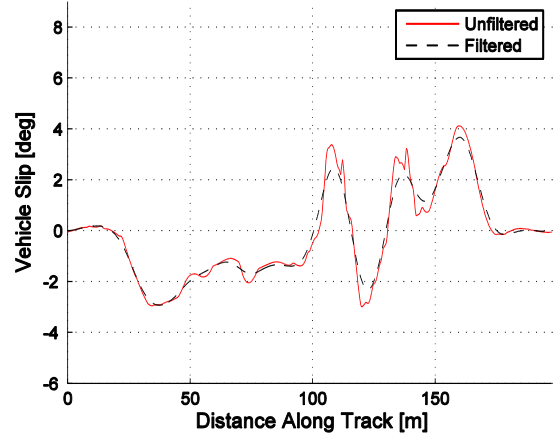


Figure 91: Vehicle slip filtering

#### 4.4.8. Steering Angle

The steered angle of the vehicle is used in the initial calculation of the LAS, but once the LAS is created, steered angle is not directly used and does not need to be calculated or referenced

during the simulation. Although it is not necessary, the steer profile can be created by identifying the corresponding steered angle at each point on the LAS in the same way that vehicle slip angle was found. Figure 92 shows the resulting unfiltered steered angle profile for the general LAS. In general, profiles for any vehicle parameter can be created to aid in analyzing and interpreting the simulation results.

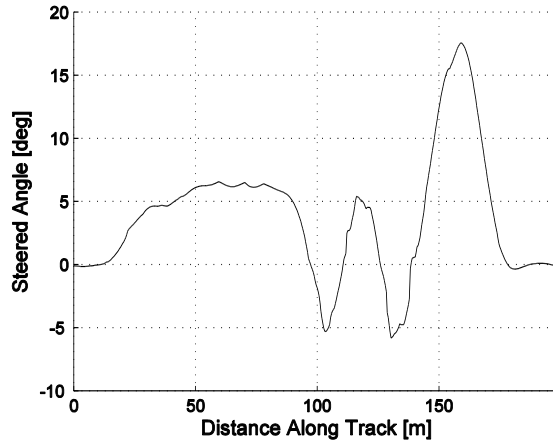


Figure 92: Steered angle profile

#### 4.4.9. Controllability and Stability

One by-product of creating the LAS is that the derivatives of lateral and yaw acceleration with respect to steered angle and vehicle slip are all known on the LAS, and their profiles can be generated in the same way the vehicle slip and steered angle profiles are created. These derivatives can aid in the understanding of vehicle stability and controllability along the path. For example, the derivative of yaw moment with respect to steered angle indicates the level of control the driver will have of the vehicle's yaw velocity. When this derivative is near zero, the driver's steering inputs will not affect the yaw rate and would likely be interpreted by the driver as limit understeer, or push/plow. Similarly, the derivative of yaw acceleration with respect to vehicle slip angle is an indicator of the vehicle's stability. For example, if the derivative is positive, a disturbance in vehicle slip angle will create a yaw acceleration that will tend to restore the original vehicle slip angle, which is a stabilizing response (note: positive yaw moments tend to create negative slip angles). When the derivative of yaw acceleration with

respect to vehicle slip is negative, it will likely be interpreted by the driver as limit oversteer, or loose/spin. Figures 93 through 96 show the derivatives of lateral and yaw acceleration with respect to both steered angle and vehicle slip. Similar plots can also be created for the effect of longitudinal slip on lateral and yaw acceleration, as well as derivatives of longitudinal acceleration with respect to steered angle, vehicle slip, and longitudinal slip, all of which can provide insight into the stability and controllability of the vehicle.

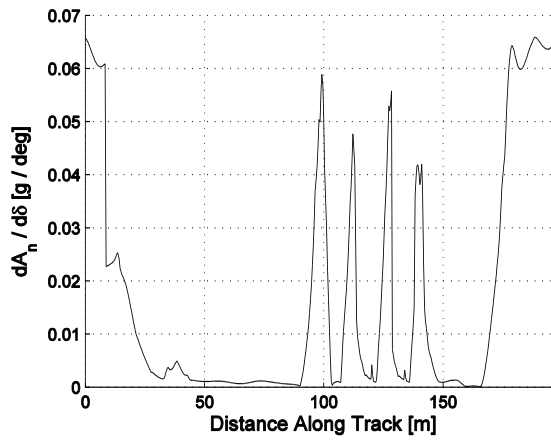


Figure 93: Derivative of lateral acceleration w.r.t. steered angle

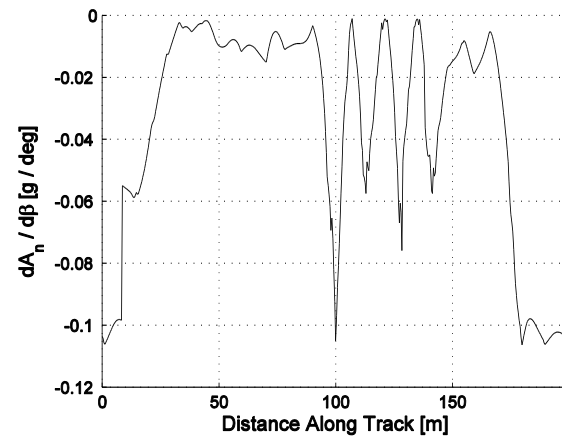


Figure 94: Derivative of lateral acceleration w.r.t. Vehicle slip angle

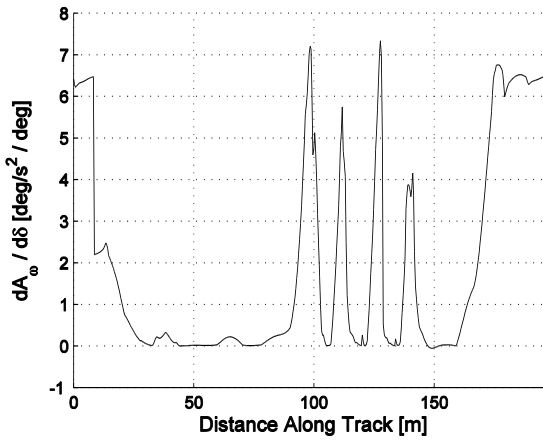


Figure 95: Derivative of yaw acceleration w.r.t. steered angle

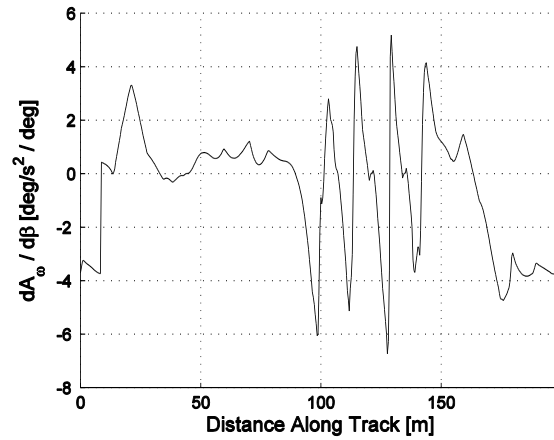


Figure 96: Derivative of yaw acceleration w.r.t. vehicle slip angle

#### 4.4.10. Power Limitation

A simple engine representation can be included by limiting the power of the vehicle while its speed is increasing. This is accomplished by limiting the speed at each forward step to the speed that could be achieved given a defined power limit ( $p_{max}$ ) using (124). Figure 97 shows a comparison of a lap simulated without power limitation and with a 30 kW limitation. The difference is most significant on the long straight, and the lap time is increased from 11.24 to 11.52 seconds.

$$v_b = \sqrt{v_a^2 + 2 \frac{p_{max}}{mv_a} \Delta s} \quad (124)$$

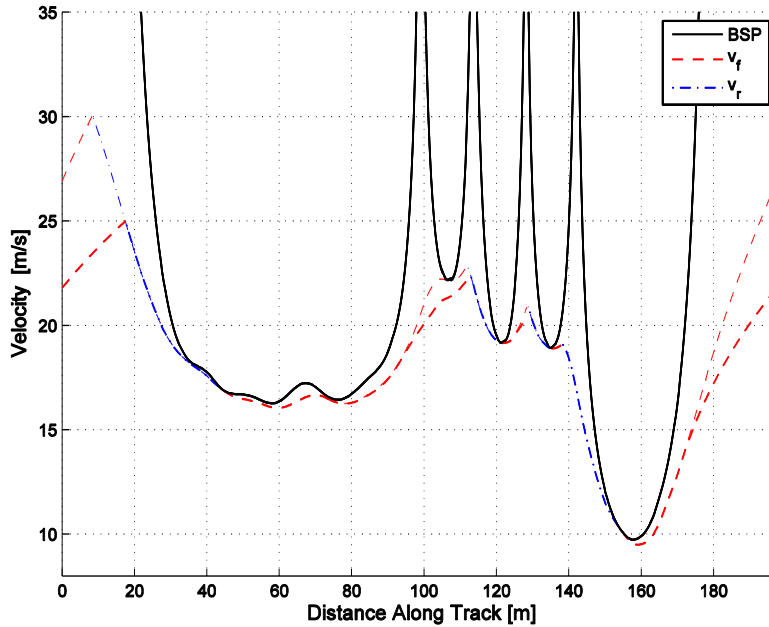


Figure 97: Power limitation

### 4.5. Results

With QTS defined, it will be evaluated and demonstrated in several ways. QTS will be compared to QSS, and used to perform a brief design study of the effect of vehicle mass, CG location and yaw inertia on vehicle performance.

#### 4.5.1. Quasi-Static vs. Quasi-Transient

Quasi-static methods do not consider the yaw moment required to traverse the defined vehicle path, and in doing so essentially remove the yaw performance limit of the vehicle. This behavior can be represented using the quasi-transient method by increasing the yaw capacity of the vehicle by many orders of magnitude (or similarly decreasing the yaw inertia), which removes the yaw limit of the vehicle. The two methods produce nearly identical lap times, with the quasi-transient method estimating 11.240 seconds for a lap while the quasi-static method (yaw capacity increased 1000 times) estimated 11.236 seconds. Although the lap times are almost identical, the vehicle slip and steer angle profiles differ significantly as shown in figures 98 and 99, as well as the yaw stability and controllability in figures 100 and 101. The differences in the results are greatest where the behavior of the vehicle is the most transient, such as corner entry and corner exit, as well as in the slaloms. This discrepancy was expected, as the quasi-static simulation simplifies these sections to steady state conditions.

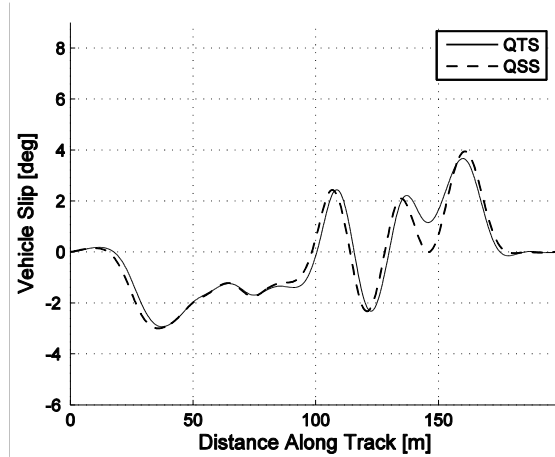


Figure 98: QSS-QTS vehicle slip comparison

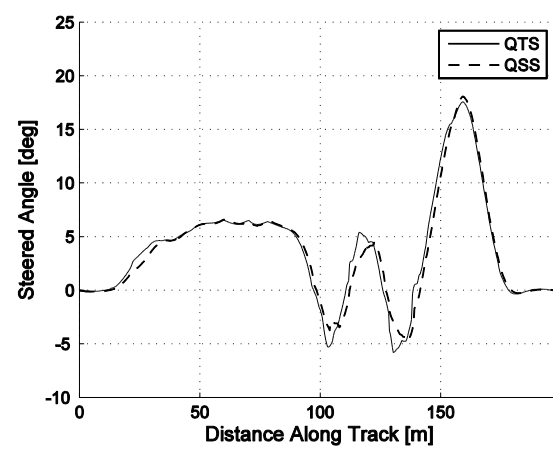


Figure 99: QSS-QTS steered angle comparison

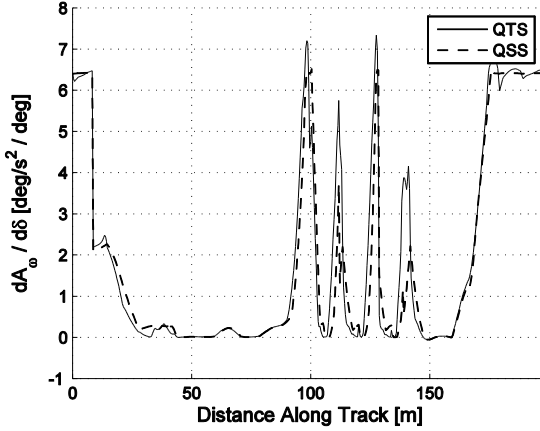


Figure 100: QSS-QTS yaw control comparison

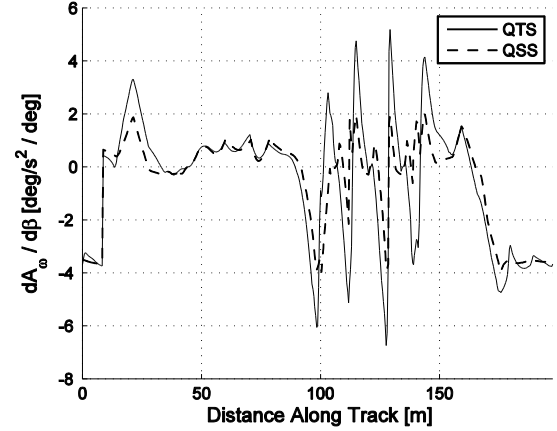


Figure 101: QSS-QTS yaw stability comparison

#### 4.5.2. Design Study

Using the general limit surface, simulations were run with mass, yaw inertia, CG location and power all varied by +/-5%. The baseline lap time was 11.52 seconds and table 1 shows the results in terms of percentage change in lap time. CG X-Position represents the percent distance forward of the rear axle (or percent weight on the front axle) and the percent change is added or subtracted from the nominal value (45% +/- 5%). The other parameters are simply increased or decreased by 5% of the nominal value.

Table 1: Design study results

Parameter	Nominal Value	-5%	+5%
Vehicle Mass	300 kg	-0.43%	0.44%
Yaw Inertia	200 kg m <sup>2</sup>	-0.017%	0.023%
CG Height	300 mm	-0.14%	0.17%
CG X-Positions	45% Front	0.43%	0.12%
Power	30 kW	0.23%	-0.21%

From this simple design study, it is apparent that lap time is less sensitive to yaw inertia than the other parameters. The study also indicates that a rearward center of gravity is a good choice,

but also suggest that the optimal GC X-position is somewhat forward of the 45% nominal value. The relative changes suggest that removing 5 kg of vehicle mass is worth approximately 15 mm of CG height reduction or a power increase of almost 1 kW.

#### 4.6. Future Work

Due to the vehicle slip angle discontinuities created at the transitions from driving to braking, a filter was used to smooth the vehicle slip profile. An alternative solution is to smooth the velocity profile only at the braking transitions such that the transition from the upper surface to the lower is not instantaneous. The vehicle slip profile in this region, as well as steer and derivative profiles, could be updated using performance information from within the LAS.

The limit surfaces used for this investigation were all limits of the vehicle's performance without considering the driver. Near the apex of each corner, the yaw acceleration response to steer input drops to zero or near zero which means that the driver would have little to no ability to correct the trajectory of the vehicle by steering. At the same time, the yaw response to vehicle slip angle often is near zero or negative, meaning the vehicle would also be unstable. A real driver would not drive on this limit and would keep some amount of control in reserve in order to deal with disturbances. It is likely that a real driver would also avoid high levels of instability, particularly when the instability corresponds with low control. A significant improvement to the quasi-transient method would be a process for developing LASs that consider the driver by limiting the performance of the vehicle based on stability and controllability limits. The work in [25] provides an initial direction for identifying these limits. The resulting velocity profiles should be a better representation of the combined driver-vehicle-track system.

#### 4.7. Conclusion

The quasi-transient lap time simulation method was defined and shown to produce lap times nearly identical to that of the quasi-static method. The effects of yaw inertia were shown to have a small effect on lap time for a given path compared to other vehicle parameters. Despite the similarity in lap time, profiles of vehicle slip and steered angle as well as several measures of stability and control were shown to differ significantly from the results of the pure steady state case. The most significant advantage of the quasi-static method is its ability to represent the

stability and controllability of the vehicle. The next steps in developing this method are to identify targets for stability and control limits and use these limits to create limit surfaces for simulation.

## 5. Dissertation Conclusion

The two primary goals of this investigation were to create tools that could accurately model vehicle behavior while providing useful insight at the same time. Extensions to Nondimensional Tire Theory contributed to these goals by allowing arbitrary inputs to be included in the model structure based on statistical significance. This structure provides direct access to key tire characteristics and how they are affected by inputs, which provides insight into how the tire will behave in use, and provides a means for modeling effects that might have previously been neglected. Accuracy of the model, measured as mean absolute error, was shown to be comparable to other published results, while including the effects of inflation pressure and rim width.

The Nondimensional Tire Model was used, along with a simple three degree of freedom model, to generate Milliken Moment Diagrams over a wide range of longitudinal accelerations and yaw rate conditions. These diagrams, and parameters derived from them, are shown to provide valuable information about the stability and controllability of the vehicle in the linear performance range, as well as on the limit of traction. Diagrams created across a vehicle's entire range of longitudinal acceleration represent a maneuvering envelope within which the vehicle performs, the outer surface of which is a limit acceleration surface that represents the limit performance of the vehicle.

Quasi-transient lap time simulation is defined, which performs computationally inexpensive lap time simulations on a predetermined path using limit acceleration surfaces. The quasi-transient method extends the quasi-static method to include yaw dynamics. Although the effect of yaw inertia on lap time was found to be quite small, there were significant differences in the behavior of the vehicle over the lap such as steered angle, vehicle slip. The ability to represent vehicle acceleration and moment derivatives over a lap allows direct evaluation of stability and controllability, which had not been previously demonstrated.

## 6. Bibliography

- [1] E.M. Kasprzak and D. Gentz, "The Formula SAE Tire Test Consortium-Tire Testing and Data Handling," Society of Automotive Engineers, SAE Paper No. 2006-01-3606, 2006.
- [2] E. Bakker, L. Nyborg, and H.B. Pacejka, "Tyre Modelling for Use in Vehicle Dynamics Studies," Society of Automotive Engineers, SAE Paper No. 870421, 1987.
- [3] H.B. Pacejka, *Tire and Vehicle Dynamics*, 2nd ed. Oxford, UK: Society of Automotive Engineers, 2006.
- [4] A.J.C. Schmeitz, I.J.M. Besselink, J. de Hoogh, and H. Nijmeijer, "Extending the Magic Formula and Swift Tyre Models for Inflation Pressure Changes," s.n., 2005.
- [5] I.J.M. Besselink, A.J.C. Schmeitz, and H.B. Pacejka, "An improved Magic Formula/Swift tyre model that can handle inflation pressure changes," *Vehicle System Dynamics*, vol. 48, Supplement, pp. 337-352, 2010.
- [6] H.S. Radt and W.F. Milliken, "Motions of Skidding Automobiles," Society of Automotive Engineering , SAE Paper No. 600133, 1960.
- [7] H.S. Radt and W.F. Milliken, "Nondimensionalizing Tyre Data for Vehicle Simulation," *Road Vehicle Handling, Institute of Mechanical Engineers*, vol. C133, pp. 229-240, 1983.
- [8] E. Fiala, "Seitenkräfte am Rollenden Luftreifen (Lateral Forces on Rolling Pneumatic Tires)," *VDI Zeitschrift*, vol. 96, 1954.
- [9] H.S. Radt and D.A. Glemming, "Normalization of Tire Force and Moment Data," *Tire Science and Technology*, vol. 21, pp. 91-119, 1993.
- [10] H.S. Radt, "Processing of Tire Force/Moment Data," Society of Automotive Engineers, SAE Paper No. 951048, 1995.

- [11] W.F. Milliken and D.L. Milliken, *Race Car Vehicle Dynamics.*: Society of Automtive Engineers, 1995.
- [12] H.S. Radt, "An Efficient Method for Treating Race Tire Force-Moment Data," Society of Automotive Engineers, SAE Paper No. 942536, 1994.
- [13] E.M. Kasprzak and K.E. Lewis, "Inflation Pressure Effects in the Nondimensional Tire Model," Society of Automotive Engineers, SAE Paper No. 2006-01-3607, 2006.
- [14] E.M. Kasprzak and K.E. Lewis, "Tire Asymmetries and Pressure Variations in the Radt/Milliken Nondimensional Tire Model," Society of Automotive Engineers, SAE Paper No. 2006-01-1968, 2006.
- [15] E.M. Kasprzak, "Extension of the Nondimensional Tire Theory to General Operating Conditions," State University of New York at Buffalo, Buffalo, New York USA, Dissertation, UMI Number: 3244243, 2007.
- [16] P. Bayle, J.F. Forissier, and S. Lafon, "A New Tyre Model for Vehicle Dynamics Simulations," *Automotive Technology International*, pp. 193-198, 1993.
- [17] H.B. Pacejka and I.J.M. Besselink, "Magic Formula Tyre Model with Transient Properties," *Vehicle System Dynamics*, vol. 27, pp. 234-249, 1997.
- [18] L. Segal, "Theoretical Prediction and Experimental Substantiation of the Response of the Automobile to Steering Control," *The Institute of Mechanical Engineers*, pp. 310-330, 1956.
- [19] W.F. Milliken, F. Dell'Amico, and R.S. Rice, "The Static Directional Stability and Control of the Automobile," Society of Automotive Engineers, SAE Paper No. 760712, 1976.
- [20] R.S. Rice and W.F. Milliken, "Static Stability and Control of the Automobile Utilizing the Moment Method," Society of Automotive Engineers, SAE Paper No. 800847, 1980.

- [21] R.S. Rice and W.F. Milliken, "Moment Method," *The Institute of Mechanical Engineers*, vol. C113, pp. 31-60, 1983.
- [22] W.F. Milliken, P.G. Wright, and D.L. Milliken, "Moment Method - A Comprehensive Tool for Race Car Development," Society of Automotive Engineers, SAE Paper No. 942538, 1994.
- [23] "Vehicle Dynamics Terminology," Society of Automotive Engineers, Warendal, PA, SAE Standard J760e 1976.
- [24] W.S. Murray, "Vehicle Dynamic Validation and Analysis from Suspension Forces," Oregon State University, M.S. Thesis 2012.
- [25] R.C. Hoffman, J.L. Stein, L.S. Louca, and K. Huh, "Using the Milliken Moment Method and Dynamic Simulation to Evaluate Vehicle Stability and Controllability," *International Journal of Vehicle Design*, vol. 48, no. 1, pp. 132-148, 2008.
- [26] D. Kang, J.L. Stein, R.C. Hoffman, L.S. Louca, and K. Huh, "Implementing the Milliken Moment Method using Controlled Dynamic Simulation," Society of Automotive Engineers, SAE Paper No. 2005-01-0417, 2005.
- [27] C.G. Bobier and J.C. Gerdes, "Staying Within the Nullcline Boundary for Vehicle Envelope Control Using a Sliding Surface," *Vehicle System Dynamics*, 2012.
- [28] D. Brayshaw and M. Harrison, "A Quasi Steady State Approach to Race Car Lap Simulation in Order to Understand the Effects of Racing Line and Centre of Gravity Location," *Proceedings of the Institution of Mechanical Engineers, Part D: Journal of Automobile Engineering*, vol. 219, pp. 725-739, 2005.
- [29] A. Candelpergher, M. Gadola, and D. Vetturi, "Developments of a Method for Lap Time Simulation," Society of Automotive Engineers, SAE Paper No. 2000-01-3562, 2000.

- [30] J.C. La Joie, "Race Car Performance Optimization," Society of Automotive Engineers, SAE Paper No. 942492, 1994.
- [31] D.W. Thomas, D.J. Segal, D.L. Milliken, and J. Michalowicz, "Analysis and Correlation using Lap Time Simulation-Dodge Stratus for the North American Touring car Championship," Society of Automotive Engineers, SAE Paper No. 962528, 1996.
- [32] M. Mühlmeier and N. Müller, "Optimization of the Driving Line on a Race Track," Society of Automotive Engineers, SAE Paper No. 2002-01-3339, 2002.
- [33] B. Siegler and D. Crolla, "Lap Time Simulation for Racing Car Design," Society of Automotive Engineers, SAE Paper No. 2002-01-0567, 2002.
- [34] A. Rucco, G. Notarstefano, and J. Hauser, "Computing minimum lap-time trajectories for a single-track car with load transfer," in *Decision and Control (CDC), 2012 IEEE 51st Annual Conference on*, 2012, pp. 6321-6326.
- [35] D. Cambiaghi, M. Gadola, L. Manzo, and D Vetturi, "A tool for lap time simulation," Society of Automotive Engineers, Paper No. 962529, 1996.
- [36] E. Velenis and P. Tsotras, "Optimal Velocity Profile Generation For Given Acceleration Limits: Receding Horizon Implementation," in *American Control Conference*, Portland, OR, USA, 2005, pp. 2147 - 2152.
- [37] E. Velenis and P. Tsotras, "Optimal Velocity Profile Generation For Given Acceleration Limits: Theoretical Analysis," in *American Control Conference*, Portland, OR, USA, 2005, pp. 1478 - 1483.
- [38] E. Velenis and P. Tsotras, "Optimal Velocity Profile Generation For Given Acceleration Limits; The Half-Car Model Case," in *IEEE International Symposium on Industrial Electronics*, vol. 1, Dubrovnik, Croatia, 2005, pp. 361-366.

- [39] E. Velenis and P. Tsiotras, "Minimum-Time Travel for a Vehicle with Acceleration Limits: Theoretical Analysis and Receding-Horizon Implementation," *Journal of Optimization Theory and Applications*, vol. 138, pp. 275-296, 2008.
- [40] D. Casanova, "On Minimum Time Vehicle Manoeuvring: The Theoretical Optimal Lap," Cranfield University, Cranfield University, PhD Thesis 2000.
- [41] D. Casanova, R.S. Sharp, and P. Symonds, "Minimum Time Manoeuvring: The Significance of Yaw Inertia," *Vehicle System Dynamics: International Journal of Vehicle Mechanics and Mobility*, vol. 34, pp. 77-115, 2000.
- [42] D. Casanova, R.S. Sharp, and P. Symonds, "On Minimum Time Optimisation of Formula One Cars: The Influence of Vehicle Mass," in *Advanced Vehicle Control*, Ann Arbor, Michigan, 2000, pp. 585-592.
- [43] D. Casanova, R.S. Sharp, and P. Symonds, "Sensitivity To Mass Variations Of The Fastest Possible Lap Of A Formula One Car.," *Vehicle System Dynamics*, vol. 35, pp. 119-134, 2001.
- [44] B. Siegle, A. Deakin, and D. Crolla, "Lap Time Simulation: Comparison of Steady State, Quasi-Static and Transient Race Car Cornering Strategies," Society of Automotive Engineers, SAE Paper No. 2000-01-3563, 2000.
- [45] R.C. Hibbeler, *Engineering Mechanics. Statics & Dynamics*, 9th ed., Eric Svendsen, Ed. Upper Saddle River, New Jersey: Prentice Hall, 2000.